

DEVELOPMENT OF ALL DIGITAL INTERFEROMETRIC CLOSED-LOOP  
FIBER OPTIC GYROSCOPE WITH YTTERBIUM DOPED  
SUPERFLUORESCENT FIBER SOURCE

A THESIS SUBMITTED TO  
THE GRADUATE SCHOOL OF NATURAL AND APPLIED SCIENCES  
OF  
MIDDLE EAST TECHNICAL UNIVERSITY

BY

HAKAN KESKIN

IN PARTIAL FULFILLMENT OF THE REQUIREMENTS  
FOR  
THE DEGREE OF DOCTOR OF PHILOSOPHY  
IN  
PHYSICS

JANUARY 2023



Approval of the thesis:

**DEVELOPMENT OF ALL DIGITAL INTERFEROMETRIC CLOSED-  
LOOP FIBER OPTIC GYROSCOPE WITH YTTERBIUM DOPED  
SUPERFLUORESCENT FIBER SOURCE**

submitted by **HAKAN KESKİN** in partial fulfillment of the requirements for the degree of **Doctor of Philosophy in Physics, Middle East Technical University** by,

Prof. Dr. Halil Kalıpçılar  
Dean, Graduate School of **Natural and Applied Sciences** \_\_\_\_\_

Prof. Dr. Seçkin Kürkcüoğlu  
Head of the Department, **Physics Dept. METU** \_\_\_\_\_

Prof. Dr. Hakan Altan  
Supervisor, **Physics Dept., METU** \_\_\_\_\_

**Examining Committee Members:**

Prof. Dr. Asaf Behzat Şahin  
Electrical and Electronics Eng., AYBU \_\_\_\_\_

Prof. Dr. Hakan Altan  
Physics Dept., METU \_\_\_\_\_

Prof. Dr. Alpan Bek  
Physics Dept., METU \_\_\_\_\_

Assist. Prof. Dr. Ihor Pavlov  
Physics Dept., METU \_\_\_\_\_

Assist. Prof. Dr. Bülend Ortaç  
UNAM, Bilkent University \_\_\_\_\_

Date: 23.01.2023

**I hereby declare that all information in this document has been obtained and presented in accordance with academic rules and ethical conduct. I also declare that, as required by these rules and conduct, I have fully cited and referenced all material and results that are not original to this work.**

Name Last name : Hakan Keskin

Signature :

## **ABSTRACT**

### **DEVELOPMENT OF ALL DIGITAL INTERFEROMETRIC CLOSED-LOOP FIBER OPTIC GYROSCOPE WITH YTTERBIUM DOPED SUPERFLUORESCENT FIBER SOURCE**

Keskin, Hakan  
Doctor of Philosophy, Physics  
Supervisor : Prof. Dr. Hakan Altan

January 2023, 145 pages

In this thesis, the development of a Fiber Optic Gyroscope (FOG) driven by Ytterbium (Yb) doped Amplified Spontaneous Emission (ASE) Source that has broad spectral bandwidth allowing for sensitive measurements is investigated. The first emphasis is given to the development of a Yb-doped ASE. This ASE operates at around 1 $\mu$ m wavelength with broad spectral bandwidth. Different ASE configurations such as single-pass forward (SPF), single-pass backward (SPB), double-pass forward (DPF), and double-pass backward (DPB) are compared in terms of spectral bandwidth, power, central wavelength stability and power stability. Additionally, mean wavelength stability is measured between the temperature of -40/+60°C to assess potential applications. Afterward, a 1 $\mu$ m all-fiber closed-loop optical gyroscope is demonstrated. Stable operation is achieved by using a fiber coil using PM fiber and the most stable ASE in terms of power and spectrum. Finally, theoretical and experimental results are compared including angular random walk (ARW) sources of a FOG.

Keywords: Superfluorescent, ytterbium, fiber, gyroscope, ASE



## ÖZ

### YTTERBIUM KATKILI SÜPERFLORESAN FİBER KAYNAKLI TAM DİJİTAL İNTERFEROMETRİK KAPALI DÖNGÜ FİBER OPTİK DÖNÜÖLÇER GELİŞTİRİLMESİ

Keskin, Hakan  
Doktora, Fizik  
Tez Yöneticisi: Prof. Dr. Hakan Altan

Ocak 2023, 145 sayfa

Bu tezde, iterbiyum (Yb) katkılı süperfloresan fiber kaynağı (SFK) ve bu ışık kaynağı ile tümleşik fiber optik dönüölçer (FOD) incelenmiştir. İlk olarak, Yb katkılı süper floresan fiber kaynağı ele alınmıştır. Bu ışık kaynağı geniş bir spektral bant aralığına sahip olur  $1\mu\text{m}$  dalga boyuna sahiptir. Çeşitli ışık kaynağı tasarımları spektrum bant genişliği, güç, merkez dalga boyu ve güç kararlılığı parametreleri üzerinden karşılaştırılmıştır. Ek olarak, farklı sıcaklıklarda merkez dalga boyu kararlılığı test edilmiştir. Ardından  $1\mu\text{m}$  dalga boyunda çalışan kapalı döngü fiber optik dönü ölçer incelenmiştir. Özel bir tip fiber ve en kararlı ışık kaynağı kullanılarak, kararlı yapıya sahip bir sistem kurulmuştur. Daha sonra, FOD gürültü kaynakları üzerinden teorik ve deneysel sonuçlar karşılaştırılmıştır.

Anahtar Kelimeler: Süperfloresan, iterbiyum, fiber, dönüölçer, ASE

Tezimi eđime adıyorum.

*I dedicate my thesis to my wife.*

## ACKNOWLEDGMENTS

First of all, this thesis is a product of team work. There are lots of people to be mentioned.

To begin with, I want to thank my beloved wife, Sinem Taşyürek Keskin for her invaluable faith in me. She provided great psychological support to me whenever I lost my eager and motivation. She is my inspiration.

Many thanks to FiberLAST Inc and Lumos Laser for letting me use their components and knowledge. I want to thank Alpan Bek, Asaf Behzat Şahin, Ihor Pavlov and Seydi Yavaş for their precious technical assistance.

My colleagues, Hüseyin Avni Vural, Bağış Altınöz, Ece Alaçakır Demir, Ümit Bektik helped me with their knowledge and talent. They gave great support and precious advice during my study. And also, I thank Alper Ünver for his contributions and advice.

I wish to express my deepest gratitude to my supervisor Hakan Altan for his guidance, advice, and insight throughout the research and methodology. I owe him a lot for my success in my career.

This work is supported by Roketsan.

## TABLE OF CONTENTS

|   |      |
|---|------|
| ABSTRACT .....                                    | v    |
| ÖZ.....   | vii  |
| ACKNOWLEDGMENTS .....                             | ix   |
| TABLE OF CONTENTS .....                           | x    |
| LIST OF TABLES .....                              | xiii |
| LIST OF FIGURES .....                             | xiv  |
| LIST OF ABBREVIATIONS .....                       | xix  |
| LIST OF SYMBOLS.....                              | xxi  |
| CHAPTERS  |      |
| 1 INTRODUCTION.....                               | 1    |
| 1.1 Principles of Optical Gyroscopes .....        | 3    |
| 1.1.1 Review of Wave Optics.....                  | 3    |
| 1.1.2 Interference of Waves.....                  | 6    |
| 1.1.3 Sagnac Effect.....                          | 7    |
| 1.2 Gyroscope Types .....                         | 10   |
| 1.2.1 Ring Laser Gyroscope .....                  | 11   |
| 1.2.2 Fiber Optic Gyroscope .....                 | 13   |
| 1.3 Digital Scheme.....                           | 17   |
| 1.3.1 Open Loop Operation .....                   | 17   |
| 1.3.2 Closed Loop Operation.....                  | 20   |
| 1.4 State of the Art in Rare-Earth Doped FOG..... | 23   |
| 2 IFOG ARCHITECTURE .....                         | 27   |

|       |  |    |
|-------|--|----|
| 2.1   | Fiber Types.....                           | 27 |
| 2.1.1 | Single Mode Fiber.....                     | 27 |
| 2.1.2 | Polarization Maintaining Fiber .....       | 27 |
| 2.1.3 | Active Fibers .....                        | 32 |
| 2.2   | Fiber Coil.....                            | 34 |
| 2.3   | Passive Components.....                    | 39 |
| 2.4   | Types of Light Sources .....               | 50 |
| 2.4.1 | Diode.....                                 | 51 |
| 2.4.2 | Laser Diode .....                          | 55 |
| 2.4.3 | Light Emitting Diode .....                 | 56 |
| 2.4.4 | Superluminescent Laser Diode .....         | 58 |
| 2.4.5 | Amplified Spontaneous Emission Source..... | 60 |
| 2.5   | Optoelectronic .....                       | 64 |
| 2.5.1 | Phase Modulator .....                      | 64 |
| 2.5.2 | Photodetectors.....                        | 66 |
| 2.6   | ASE Source for 1030nm IFOG .....           | 73 |
| 2.6.1 | Ytterbium Gain Medium.....                 | 73 |
| 2.6.2 | Gain Dynamics.....                         | 76 |
| 2.7   | ASE Source Optimization .....              | 80 |
| 2.7.1 | ASE Configurations .....                   | 81 |
| 2.7.2 | Test Results .....                         | 82 |
| 2.7.3 | Simulation Results .....                   | 91 |
| 3     | IFOG NOISE ANALYSIS.....                   | 95 |
| 3.1   | Noise Types of IFOG .....                  | 95 |

|       |  |     |
|-------|--|-----|
| 3.1.1 | Allan Variance Analysis .....          | 96  |
| 3.1.2 | Bias Instability .....                 | 97  |
| 3.1.3 | Angular Random Walk .....              | 98  |
| 3.2   | Noise Analysis .....                   | 99  |
| 3.2.1 | Two-level Modulation .....             | 99  |
| 3.2.2 | Four-level Modulation .....            | 101 |
| 3.3   | Sources of ARW .....                   | 103 |
| 3.3.1 | Shot Noise .....                       | 103 |
| 3.3.2 | Relative Intensity Noise .....         | 105 |
| 3.3.3 | Electronic Noises .....                | 106 |
| 3.3.4 | Total ARW of FOG .....                 | 111 |
| 3.4   | Phase Noise and SNR Optimization ..... | 113 |
| 4     | EXPERIMENTAL RESULTS .....             | 117 |
| 4.1   | Fiber Coil Assembly Tests .....        | 117 |
| 4.2   | ASE Assembly Tests .....               | 121 |
| 4.3   | IFOG Prototype and Tests .....         | 127 |
| 5     | CONCLUSION .....                       | 133 |
|       | REFERENCES .....                       | 135 |
|       | CURRICULUM VITAE .....                 | 145 |

## LIST OF TABLES

### TABLES

|  |     |
|--|-----|
| Table 2.1. Various operational wavelength ranges .....               | 43  |
| Table 2.2. Comparison of materials used in photodetectors [56] ..... | 72  |
| Table 4.1. Nufern/PM980-XP-80 specifications.....                    | 117 |
| Table 4.2. Fiber coil specifications .....                           | 118 |
| Table 4.3. PER meter results.....                                    | 118 |
| Table 4.4. MIOC characteristics .....                                | 119 |
| Table 4.5. MIOC power coupling .....                                 | 120 |
| Table 4.6. Laser diode specifications.....                           | 121 |
| Table 4.7. PPF specifications .....                                  | 122 |
| Table 4.8. WDM specifications .....                                  | 123 |
| Table 4.9. Yb-doped fiber specifications .....                       | 123 |
| Table 4.10. Isolator data.....                                       | 124 |
| Table 4.11. 50/50 coupler specifications .....                       | 128 |
| Table 4.12. PINFET specifications .....                              | 129 |

## LIST OF FIGURES

### FIGURES

|  |    |
|--|----|
| Figure 1.1. Graph of power loss in fiber versus wavelength [7] .....                 | 6  |
| Figure 1.2. Sagnac effect in a CW rotating in a closed ring-shaped waveguide .....   | 8  |
| Figure 1.3. RLG schematic [5] .....  | 12 |
| Figure 1.4. RFOG architecture [5] .....  | 14 |
| Figure 1.5. BFOG architecture [12] .....   | 15 |
| Figure 1.6. Basic schematic of FOG [14] .....  | 16 |
| Figure 1.7. Square wave modulation scheme [1] .....                                  | 18 |
| Figure 1.8. Cosine modulation [5] .....  | 19 |
| Figure 1.9. Cosine modulation with rotation [5] .....                                | 19 |
| Figure 1.10. Closed-loop architecture [5] .....                                      | 20 |
| Figure 1.11. Two-level modulation output response [5] .....                          | 21 |
| Figure 1.12. Four-level modulation output response [5] .....                         | 22 |
| Figure 1.13. Four-level modulation output response with rotation [5] .....           | 22 |
| Figure 2.1. Fiber cable [7] .....  | 27 |
| Figure 2.2. PMD effect a) without and a) with mode coupling [31] .....               | 28 |
| Figure 2.3. PM fiber types a) panda b) bow tie c) elliptical [31] .....              | 29 |
| Figure 2.4. Fast and slow axes with the effect of stress bars in PM fiber [5] .....  | 30 |
| Figure 2.5. PMD, decoherence length and beat length [5] .....                        | 30 |
| Figure 2.6. Symmetrical depolarization lengths [5] .....                             | 32 |
| Figure 2.7. Energy level diagram of Er-doped fiber [32] .....                        | 33 |
| Figure 2.8. Energy level diagram of Yb-doped fiber [33] .....                        | 34 |
| Figure 2.9. Representation of windings in order to create winding pattern [34] ..... | 35 |
| Figure 2.10. Various fiber coils [35] .....  | 36 |
| Figure 2.11. Quadrupole and octupole winding patterns [5], [39] .....                | 36 |
| Figure 2.12. Winding errors [40] .....   | 37 |
| Figure 2.13. Fiber subjected to bending stress [9] .....                             | 38 |
| Figure 2.14. Bending loss depending on coil diameter and numerical aperture .....    | 39 |

|  |    |
|--|----|
| Figure 2.15. Coupling of two fiber using side polishing [5].....   | 40 |
| Figure 2.16. Coupler ports .....   | 41 |
| Figure 2.17. Coupler [42].....   | 41 |
| Figure 2.18. 1x3 coupler [43] .....  | 42 |
| Figure 2.19. Coupler port types .....  | 42 |
| Figure 2.20. Alignment of stress bars of PM fibers .....   | 43 |
| Figure 2.21. FWDM [44] .....   | 44 |
| Figure 2.22. 4 port circulator representations [7].....  | 44 |
| Figure 2.23. Circulator with 3 ports [44] .....  | 45 |
| Figure 2.24. FBG refractive index difference [45] .....  | 45 |
| Figure 2.25. Reflection of selected wavelength [47] .....  | 47 |
| Figure 2.26. Difference of uniform FBG and periodic refractive index .....   | 47 |
| Figure 2.27. Chirped FBG and periodic refractive index difference .....  | 48 |
| Figure 2.28. Blazed FBG and resulting polarization modes [46] .....  | 48 |
| Figure 2.29. Superstructure FBG .....  | 49 |
| Figure 2.30. Isolator operation principle [48] .....   | 50 |
| Figure 2.31. Isolator [48] .....   | 50 |
| Figure 2.32. Diode symbol.....   | 51 |
| Figure 2.33. (a) Forward biasing of the diode (b) Reverse biasing of the diode (Black regions represent electron-free regions.)..... | 52 |
| Figure 2.34. Current flowing across a diode versus the voltage applied .....   | 53 |
| Figure 2.35. Diodes examples [49] .....  | 54 |
| Figure 2.36. Laser diode, SLD and LED spectrum for InGasAsP/InP devices [7] .....  | 54 |
| Figure 2.37. Laser diode [50].....   | 55 |
| Figure 2.38. LED electronic symbol.....  | 56 |
| Figure 2.39. Basic LED circuit .....   | 56 |
| Figure 2.40. Light generation in PN-type semiconductor technology .....  | 57 |
| Figure 2.41. LEDs of different types and cladding [51] .....   | 57 |
| Figure 2.42. SLD examples [52].....  | 60 |
| Figure 2.43. Graph of power loss in fiber versus wavelength [5].....   | 61 |

|  |    |
|--|----|
| Figure 2.44. The scattering of the light in the fiber [5] .....  | 62 |
| Figure 2.45. ASE source components .....   | 62 |
| Figure 2.46. Pump laser [53] .....   | 63 |
| Figure 2.47. Pump laser spectrum .....   | 63 |
| Figure 2.48. ASE output spectrum for 1550nm ASE source[32].....  | 64 |
| Figure 2.49. Piezoelectric phase modulator [5].....  | 65 |
| Figure 2.50. MIOC [5].....   | 65 |
| Figure 2.51. Photodiode electronic symbol .....  | 67 |
| Figure 2.52. P-N type photodiode working principle [55] .....  | 67 |
| Figure 2.53. Photodiode characteristic [7] .....   | 68 |
| Figure 2.54. Comparison of detector material types [7].....  | 70 |
| Figure 2.55. PINFET example [57] .....   | 72 |
| Figure 2.56. Basic FET circuit .....   | 72 |
| Figure 2.57. a) Three-level b) four-level c) quasi-three-level systems .....   | 73 |
| Figure 2.58. Absorption and emission cross-sections of Yb-doped fibers [60] .....  | 75 |
| Figure 2.59. SPB and SPF representations .....   | 79 |
| Figure 2.60. DPB and DPF representations.....  | 80 |
| Figure 2.61. SP ASE architectures a) SPF b) SPB .....  | 81 |
| Figure 2.62. DP ASE architecture a) DPF b) DPB.....  | 81 |
| Figure 2.63. Temperature test setup .....  | 82 |
| Figure 2.64. SPF configuration output spectrum for different pump currents a) 0.6m<br>b) 0.8m and c) 1.0m.....                                       | 83 |
| Figure 2.65. SPF a) output power and b) mean wavelength for different Yb-doped<br>fiber lengths. c) Mean wavelength for different temperatures ..... | 84 |
| Figure 2.66. SPB configuration output spectrum for different pump currents a) 0.6m<br>b) 0.8m and c) 1.0m.....                                       | 85 |
| Figure 2.67. SPB a) output power and b) mean wavelength for different Yb-doped<br>fiber lengths. c) Mean wavelength for different temperatures ..... | 86 |
| Figure 2.68. DPF configuration output spectrum for different pump currents a) 0.6m<br>b) 0.8m and c) 1.0m.....                                       | 87 |

|  |     |
|--|-----|
| Figure 2.69. DPF a) output power and b) mean wavelength for different Yb-doped fiber lengths. c) Mean wavelength for different temperatures..... | 88  |
| Figure 2.70. DPB configuration output spectrum for different pump currents a) 0.6m b) 0.8m and c) 1.0m .....                                     | 89  |
| Figure 2.71. DPB a) output power and b) mean wavelength for different Yb-doped fiber lengths. c) Mean wavelength for different temperatures..... | 90  |
| Figure 2.72. SPF spectrum simulation and test result.....  | 91  |
| Figure 2.73. SPB spectrum simulation and test result .....   | 92  |
| Figure 2.74. DPF spectrum simulation and test result .....   | 92  |
| Figure 2.75. DPB spectrum simulation and test result.....  | 93  |
| Figure 3.1. Noises in FOG [5] .....  | 95  |
| Figure 3.2. Allan variance graph and related noises [66] .....   | 96  |
| Figure 3.3. Bias instability parameter variance plot [66].....   | 98  |
| Figure 3.4. Angle random walk parameter variance plot [66].....  | 99  |
| Figure 3.5. Noise sources in FOG.....  | 103 |
| Figure 3.6. Equivalent circuit of a transimpedance amplifier.....  | 106 |
| Figure 3.7. ARW analysis of (a) 1030nm; (b) 1550nm FOG .....   | 112 |
| Figure 3.8. SNR analysis of 1030nm FOG (a) 100 $\mu$ W (b) 105 $\mu$ W optical power   | 114 |
| Figure 3.9. Single pass backward configuration .....   | 115 |
| Figure 4.1. PER meter test setup.....  | 118 |
| Figure 4.2. Fiber optic coil.....  | 119 |
| Figure 4.3. Fiber optic coil assembly .....  | 121 |
| Figure 4.4. Laser diode characteristics.....   | 122 |
| Figure 4.5. ASE source .....   | 125 |
| Figure 4.6. ASE source assembly .....  | 125 |
| Figure 4.7. ASE source assembly and laser diode driver .....   | 126 |
| Figure 4.8. Yb-doped ASE source spectrum output .....  | 126 |
| Figure 4.9. Optical power output of Yb-doped ASE source.....   | 127 |
| Figure 4.10. Functional scheme of Yb ASE IFOG .....  | 128 |
| Figure 4.11. Driver electrical board.....  | 129 |

|  |     |
|--|-----|
| Figure 4.12. IFOG prototype .....  | 130 |
| Figure 4.13. Signal output with no rotation.....                                     | 130 |
| Figure 4.14. Signal output while rotating .....                                      | 131 |
| Figure 4.15. Allan variance analysis for 10, 110 and 120 $\mu$ W optical power ..... | 132 |

## LIST OF ABBREVIATIONS

### ABBREVIATIONS

|      |   |
|------|---|
| ASE  | : Amplified spontaneous emission          |
| ADC  | : Analog-to-digital converter             |
| ARW  | : Angular random walk                     |
| APD  | : Avalanche photodiode                    |
| BF   | : Back faced                              |
| BFOG | : Brillouin fiber optic gyroscope         |
| CFBG | : Chirped fiber Bragg grating             |
| CW   | : Clockwise                               |
| CCW  | : Counter-clockwise                       |
| DSP  | : Digital signal processing               |
| DAC  | : Digital-to-analog converter             |
| DPB  | : Double pass backward                    |
| DPF  | : Double pass forward                     |
| Er   | : Erbium                                  |
| EDFA | : Erbium-doped fiber amplifier systems    |
| EDFS | : Erbium-doped Fiber Source               |
| FBG  | : Fiber Bragg grating                     |
| FWDM | : Filter Wavelength Division Multiplexer  |
| FWHM | : The full width at half maximum          |
| IFOG | : Interferometric fiber optic gyroscope   |
| LD   | : Laser diode                             |
| LED  | : Light emitting diodes                   |
| MDF  | : Mode field diameter                     |
| MIOC | : Multifunctional Integrated Optical Chip |
| NA   | : Numerical aperture                      |
| OSA  | : Optical spectrum analyzer               |

PER : Polarization extinction ratio  
PM : Polarization maintaining  
PMD : Polarization mode dispersion  
PSD : Power spectral density  
CPU : Processing unit  
PIN : p-type, intrinsic and n-type  
PINFET : p-type-intrinsic-n-type field effect transistor  
PPF : Pump protection filter  
RIN : Relative intensity noise  
RFOG : Resonant fiber optic gyroscope  
RLG : Ring laser gyroscope  
SF : Scale factor  
SNR : Signal-to-noise ratio  
SM : Single-mode  
SPB : Single pass backward  
SPF : Single pass forward  
SLED : Super bright light emitting diodes  
SLD : Superluminescent laser diode  
SRD : Super-radiant Diode  
UV : Ultraviolet  
WDM : Wavelength Division Multiplexer  
Yb : Ytterbium

## LIST OF SYMBOLS

### SYMBOLS

|                   |                                   |
|-------------------|-----------------------------------|
| $\vec{E}$         | : Electric field strength         |
| $\vec{H}$         | : Magnetic field strength         |
| $\vec{D}$         | : Dielectric displacement         |
| $\vec{B}$         | : Magnetic induction              |
| $\vec{J}$         | : Current density                 |
| $\rho$            | : Charge density                  |
| $\vec{P}$         | : Polarization                    |
| $\vec{M}$         | : Magnetization                   |
| $\rho$            | : Conductivity                    |
| $\epsilon_0$      | : Permittivity of vacuum          |
| $\mu_0$           | : Permeability of the vacuum      |
| $c$               | : Speed of light                  |
| $\epsilon$        | : Relative dielectric constant    |
| $\omega$          | : Angular frequency               |
| $n$               | : Refractive index                |
| $\alpha$          | : Absorption coefficient          |
| $\phi_i$          | : Respective phase of fields      |
| $\lambda$         | : Wavelength of light in a vacuum |
| $\Delta\phi$      | : Phase difference of the waves   |
| $\Omega$          | : Rotation rate                   |
| $f$               | : Optical frequency               |
| $\Delta\phi_R$    | : Phase change due to rotation    |
| $\Delta\phi_m$    | : Phase modulation                |
| $\Delta\phi_{fb}$ | : Feedback phase shift            |
| $P_{\perp}(L)$    | : Vertical polarization mode      |

|                        |  |
|------------------------|--|
| $P_{\parallel in}$     | : Parallel axis input polarization mode    |
| $h$                    | : h-parameter                              |
| $\Lambda$              | : Beat length                              |
| $\Delta n_b$           | : Birefringence                            |
| $L_{dc}$               | : Decoherent length                        |
| $\Delta\lambda_{FWHM}$ | : Full-width half maximum                  |
| $L_d$                  | : Depolarization length                    |
| $\mu$                  | : Micro                                    |
| $\lambda_c$            | : Cut-off wavelength                       |
| $\Lambda_{Bragg}$      | : Bragg period                             |
| $I_d$                  | : Diode current                            |
| $V_d$                  | : Diode voltage                            |
| $I_s$                  | : Reverse bias saturation current          |
| $\eta$                 | : Quantum efficiency                       |
| $e$                    | : Electron charge                          |
| $h$                    | : Planck constant                          |
| $\nu$                  | : Photon frequency                         |
| $q$                    | : Quantum defect                           |
| $\nu_l$                | : Lasing frequency                         |
| $\nu_p$                | : Pump frequency                           |
| $R_{12}$               | : Rates of pump excitation                 |
| $R_{21}$               | : Rates of pump relaxation                 |
| $W_{12}$               | : Rates of signal absorption               |
| $W_{21}$               | : Rates of signal emission                 |
| $A_{21}$               | : Rate of spontaneous emission             |
| $n_1$                  | : Number of the ground state               |
| $n_2$                  | : Number of the excited state              |
| $\sigma_{ap}$          | : Effective pump absorption cross-sections |
| $\sigma_{ep}$          | : Effective emission cross-sections        |

|                  |  |
|------------------|--|
| $\sigma_{as}$    | : Effective signal absorption cross-sections         |
| $\sigma_{es}$    | : Effective signal emission cross-sections           |
| $\tau$           | : Lifetime of the ions                               |
| $P_p$            | : Pump power   |
| $P_s$            | : Signal power                                       |
| $\Gamma_p$       | : Overlap factor of the pump                         |
| $\Gamma_s$       | : Overlap factor of the signal                       |
| $\bar{\lambda}$  | : Mean wavelength                                    |
| $\varepsilon$    | : Photon energy                                      |
| $i_d$            | : Dark current                                       |
| $R_d$            | : Photodiode dynamic resistance                      |
| $R_s$            | : Photodiode series resistance                       |
| $k_b$            | : Boltzmann constant                                 |
| $i_{n,TIA}$      | : Op-amp input noise current                         |
| $R_f$            | : Feedback resistance                                |
| $v_{n,TIA}$      | : Op-amp input noise voltage spectral density        |
| $v_{ADC}$        | : Voltage noise density of the D/A converter         |
| $v_{VA}$         | : The voltage noise density of the voltage amplifier |
| $V_\pi$          | : Voltage that creates pi phase shift                |
| $\sigma_{R,S}$   | : Rate noise due to shot noise                       |
| $\sigma_{R,RIN}$ | : Rate noise due to RIN                              |
| $\sigma_{R,E}$   | : Rate noise due to electronic noise                 |
| $t_s$            | : Sampling time                                      |
| $t_{int}$        | : Integration time                                   |



## **CHAPTER 1**

### **INTRODUCTION**

Imagine an observer is located inside a black box. The black box is moving and rotating freely. At the same time, the observer cannot interact with its surroundings because the black box blocks all types of interactions such as visual contact, light, magnetic, etc. However, it is required to measure the exact position and rotation of the observer. Global Navigation Satellite System (GNSS) or other positioning systems such as barometer, magnetometer, magnetic compass, etc. is not allowed. At this point, the observer has no choice but to use inertial sensors. Inertial sensors such as accelerometers and gyroscopes allow us to measure linear acceleration and angular velocity using the physical laws of motion.

As a crucial class of sensors, inertial sensor applications are continuously growing as they were first used in aerospace and military applications. Gyroscopes which are also named gyro measure the rotational rate of a body around a linear axis that is fixed with respect to an inertial space. Gyroscopes are named inertial sensors after this operational principle.

Mainly, three types of gyros have been designed and developed based and angular momentum conservation, the Sagnac effect and the Coriolis effect in the last five decades.

Mechanical gyros were the first types of gyroscopes. They have a mass namely a rotor spinning very rapidly and steadily around an axis. The rotor keeps its direction of rotation due to the conservation of the angular moment principle. The dynamically Tuned Gyroscope (DTG) and the Control Moment Gyroscope (CMG) were

developed using such principle and also used in space missions [1]. Mechanical gyroscopes have delicate and moving parts that lower the reliability of systems.

Although mechanical gyroscopes have great historical importance in terms of performance, their size and initial production and maintenance cost raised a need for smaller and low-cost versions of gyroscopes. The first response to this need was in optics. The invention of lasers enabled to development of optical gyroscopes such as Ring Laser Gyroscopes (RLG) [2]. RLG was designed based on the Sagnac effect which is the phase shift due to rotation between two counter-propagating waves in a rotating ring interferometer. Classical RLGs have a mechanical dithering system which is a moving part in the sensor. Consequently, the complication and price of the RLG sensor increase.

While the mass production of RLG enabled the gyroscopes to be used in various applications, the size of RLG-based systems still was an issue. Hemispherical Resonator Gyro (HRG) which is a vibrating gyro was invented in the 1980s [3]. Vibrating gyroscopes are based on the Coriolis effect. This effect creates a coupling between two resonant modes of a mechanical resonator. HRG consisting of a fused silica hemispherical shell sensing element has a great rotational sensing performance. However, it is still an expensive sensor. This results in the development of another vibrating gyro names as Micro-Electro-Mechanical System (MEMS) gyroscopes. Silicon and quartz MEMS gyros are highly miniaturized and used in many applications since their invention [4]. Low-cost is a very attractive characteristic of MEMS gyroscopes despite low-grade performance.

Requirement of a compact, low-sized, low-cost, reliable and highly sensitive rotation sensing element. Another photonic gyroscope type met all of these requirements. Fiber Optic Gyroscope (FOG) has a solid-state sensing element namely fiber optics. This increases the reliability of the sensors. Fiber optic-based telecommunication systems enabled to have compact and low-cost components. Additionally, the sensitivity of a FOG is directly proportional to its fiber coil length and effective

diameter which enables to design and manufacture of navigation-grade to strategic-grade sensitive sensors [5].

## 1.1 Principles of Optical Gyroscopes

### 1.1.1 Review of Wave Optics

Optical calculations in optics are mainly done with two techniques; raytracing and wave optics. Ray optics gives a general view of an optical system. On the other hand, optical phenomena such as diffraction and interference are omitted in ray optics. When the dimensions of the system are comparable with the wavelength of light waves as in single-mode fiber cables, raytracing is not sufficient enough to describe the system. Hence, wave optics is required to define the physics of fiber optic gyroscope.

Optical waves in a medium can be defined as an electromagnetic wave and Maxwell equations of electromagnetism are used to derive differential wave equation which defines the propagation of light through the medium [6].

$$\nabla \cdot \vec{D} = \rho \quad (1.1)$$

$$\nabla \cdot \vec{B} = 0 \quad (1.2)$$

$$\nabla \times \vec{E} = -\frac{\partial \vec{B}}{\partial t} \quad (1.3)$$

$$\nabla \times \vec{H} = \vec{J} + \frac{\partial \vec{D}}{\partial t} \quad (1.4)$$

Here,  $\vec{E}$  is electric field strength [V/m],  $\vec{H}$  is magnetic field strength [A/m],  $\vec{D}$  is dielectric displacement [As/m<sup>2</sup>],  $\vec{B}$  is magnetic induction [Vs/m<sup>2</sup>=T],  $\vec{J}$  is current density [A/m<sup>2</sup>],  $\rho$  is charge density [As/m<sup>3</sup>].

Generally, propagation in a vacuum is studied first, however, the process inside the material should be studied considering fiber materials. Parameters such as

polarization ( $\vec{P}$ ), magnetization ( $\vec{M}$ ) and conductivity ( $\rho$ ) define material characteristics effected by electromagnetism. Polarization and magnetization are related to the shift of atomic orbitals when they are subjected to electromagnetic waves. The flow of only electrons can be defined by conductivity whereas there are no magnetic charges. Relation to dielectric displacement, magnetic induction and current density are as follows [6].

$$\vec{D} = \epsilon_0 \vec{E} + \vec{P} \quad (1.5)$$

$$\vec{B} = \mu_0 (\vec{H} + \vec{M}) \quad (1.6)$$

$$\vec{J} = \sigma \vec{E} \quad (1.7)$$

Here,  $\epsilon_0$  is the permittivity of vacuum and  $\mu_0$  is the permeability of the vacuum.

Mainly, there are three approximations for air or a medium such as silica glass such as there are no free charges, there are no currents and there is no magnetization.

$$\rho = \vec{J} = \vec{M} = 0 \quad (1.8)$$

These approximations yield equations influenced by only polarization effects.

$$\nabla \cdot \vec{D} = 0 \quad (1.9)$$

$$\nabla \cdot \vec{B} = 0 \quad (1.10)$$

$$\nabla \times \vec{E} = -\frac{\partial \vec{B}}{\partial t} \quad (1.11)$$

$$\nabla \times \vec{B} = \mu_0 \frac{\partial \vec{D}}{\partial t} \quad (1.12)$$

The cross product of Equation (1.11) is calculated in order to derive the wave equation.

$$\nabla \times \nabla \times \vec{E} = \nabla \times \left( -\frac{\partial \vec{B}}{\partial t} \right) \quad (1.13)$$

Using the property of a cross product;

$$\nabla (\nabla \cdot \vec{E}) - \nabla^2 \vec{E} = -\frac{\partial}{\partial t} (\nabla \times \vec{B}) \quad (1.14)$$

Put Equations (1.12) and (1.5) into (1.14);

$$\nabla (\nabla \cdot \vec{E}) - \nabla^2 \vec{E} = -\mu_0 \epsilon_0 \frac{\partial^2}{\partial t^2} \vec{E} - \mu_0 \frac{\partial^2}{\partial t^2} \vec{P} \quad (1.15)$$

The final wave equation is derived as:

$$\nabla^2 \vec{E} - \nabla (\nabla \cdot \vec{E}) = \frac{1}{c^2} \frac{\partial^2 \vec{E}}{\partial t^2} + \mu_0 \frac{\partial^2 \vec{P}}{\partial t^2} \quad (1.16)$$

Wave equation for a magnetic field can be derived similarly.

Silica glass has a homogeneous structure and the material is polarized parallel to the field strength. Therefore;

$$\nabla \cdot \vec{D} = \nabla \cdot \vec{E} = 0 \quad (1.17)$$

$$\nabla^2 \vec{E} = \frac{1}{c^2} \frac{\partial^2 \vec{E}}{\partial t^2} + \mu_0 \frac{\partial^2 \vec{P}}{\partial t^2} \quad (1.18)$$

Here, polarization is a material characteristic. Assuming that response polarization to field effect is instantaneous, polarization can be written as;

$$\vec{P} = \epsilon_0 (\chi^{(1)} \vec{E} + \chi^{(2)} \vec{E}^2 + \chi^{(3)} \vec{E}^3 + \dots) \quad (1.19)$$

In general,  $\chi^i$  the term is a tensor however for homogenous materials such as silica it is a scalar term. Assuming only having linear relation between polarization and field strength and using Equation (1.5);

$$\vec{P} = \epsilon_0 \chi^{(1)} \vec{E} \quad (1.20)$$

$$\vec{D} = \epsilon_0 \vec{E} (1 + \chi^{(1)}) \quad (1.21)$$

Relative dielectric constant ( $\epsilon$ ) is related to terms inside parenthesis.

$$\epsilon = (1 + \chi^{(1)}) = \left( n + i \frac{c}{2\omega} \alpha \right)^2 \quad (1.22)$$

Here,  $n$  is the refractive index and  $\alpha$  is the absorption coefficient. Assuming in a very low loss medium such as silica ( $\text{SiO}_2$ ),  $\alpha$  is so small for wavelengths around 1550nm as given in Figure 1.1 that the relative dielectric constant is real.

$$\epsilon = n^2 \quad (1.23)$$

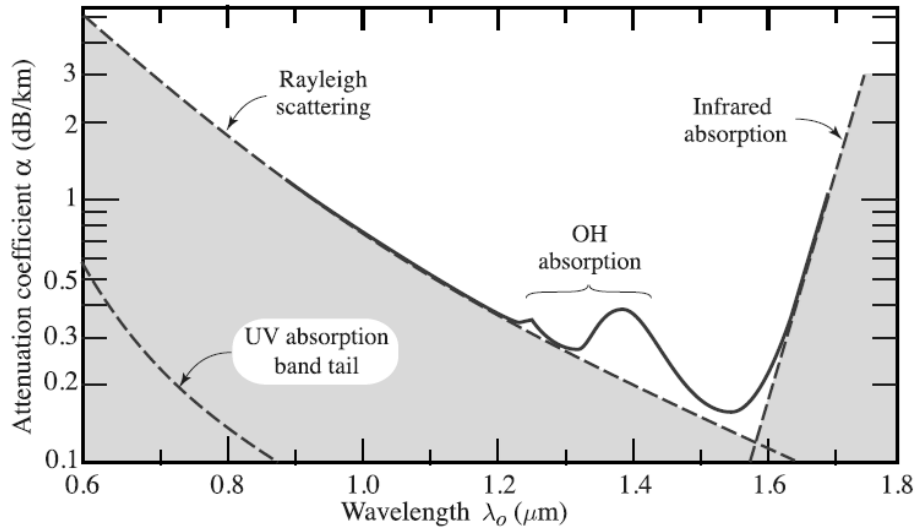


Figure 1.1. Graph of power loss in fiber versus wavelength [7]

Using Equations (1.18), (1.20), (1.22) and (1.23), we get simple wave equation.

$$\nabla^2 \vec{E} = \frac{n^2}{c^2} \frac{\partial^2 \vec{E}}{\partial t^2} \quad (1.24)$$

Similarly, for the magnetic field, we get;

$$\nabla^2 \vec{H} = \frac{n^2}{c^2} \frac{\partial^2 \vec{H}}{\partial t^2} \quad (1.25)$$

### 1.1.2 Interference of Waves

Optical waves have a very high rate of frequency. It is not possible to direct measure the phase of electromagnetic waves. Therefore, indirect measurement methods of optical power or intensity using interference are required. A fiber optic gyroscope is

a rotation-sensing interferometer in which light input is split into two waves. Counterpropagating waves are recombined at the output. Resulting superposition of waves ( $E(\vec{r}, t)$ ) is the vectorial sum of split waves ( $E_1(\vec{r}, t), E_2(\vec{r}, t)$ ) propagated along different paths [7].

$$E(\vec{r}, t) = E_1(\vec{r}, t) + E_2(\vec{r}, t) \quad (1.26)$$

$$E_i(\vec{r}, t) = E_{i0} e^{i(\omega t + \phi_i)} \quad (1.27)$$

Here,  $E_{i0}$  is the maximum amplitude of fields.  $\phi_i$  is a respective phase of fields and depends on a total propagated optical path.

$$\frac{\phi_i}{2\pi} = \frac{L_{op}}{\lambda} \quad (1.28)$$

Here,  $\lambda$  is the wavelength of light in a vacuum. The intensity of a wave is the square of the field however the sum of the superposition of two waves is calculated as proportional to the temporal averaging of the scalar square of the field.

$$\langle \vec{E} \vec{E}^* \rangle = \langle \vec{E}_1 \vec{E}_1^* \rangle + \langle \vec{E}_2 \vec{E}_2^* \rangle + \langle \vec{E}_1 \vec{E}_2^* \rangle + \langle \vec{E}_2 \vec{E}_1^* \rangle \quad (1.29)$$

Result of Equation (1.29);

$$I = I_1 + I_2 + 2\sqrt{I_1 I_2} \cos(\Delta\phi) \quad (1.30)$$

Here,  $I_i$  is the intensity of input waves,  $\Delta\phi$  is the phase difference of the waves which is related to the optical path difference. It is important to mention that the state of polarization of both incoming waves is the same. Otherwise, the orthogonal state of polarization would yield no interference because the scalar product of  $\vec{E}_1 \cdot \vec{E}_2^*$  and  $\vec{E}_2 \cdot \vec{E}_1^*$  are equal to zero. This would result in the direct addition of intensities.

### 1.1.3 Sagnac Effect

Sagnac Effect is observed as a phase shift that occurs when two rays traveling in opposite directions travel different paths at different times under a certain rotation in

a closed and fixed-length waveguide as shown in Figure 1.2. The Red dashed line, green dashed line and blue solid line are clockwise (CW), counter clock-wise (CCW) and waveguide, respectively.

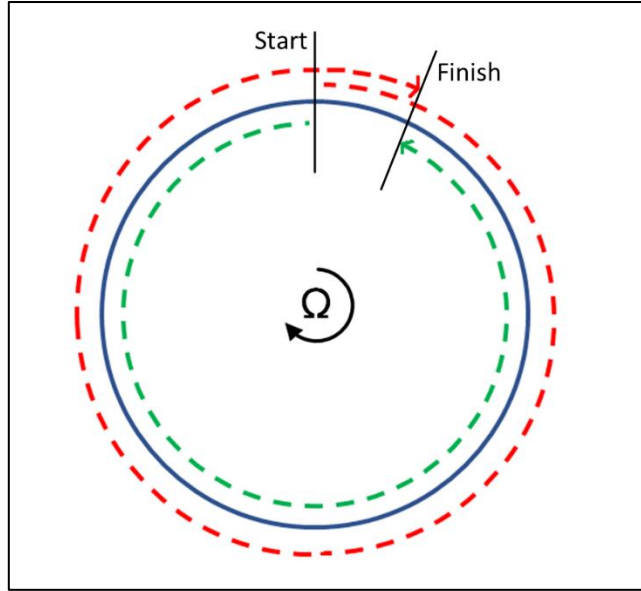


Figure 1.2. Sagnac effect in a CW rotating in a closed ring-shaped waveguide

When the waveguide is at rest with respect to an inertial frame, the distance traveled by CW and CCW waves is equal to each other. In the case of a rotation of  $\Omega$ , they arrive at the finishing point at different times. Time of rotation beams inside the closed waveguide with a radius  $R$  is  $t_R$ ,

$$t_R = \frac{2\pi R}{c} \quad (1.31)$$

During this time, starting point moves to the finishing point and travels

$$\Delta l = \Omega R t_R \quad (1.32)$$

Co-propagating CW beam is subjected to a slightly longer path. Similarly, the counter-propagating CCW beam experiences a shorter path. Therefore, the total path difference between the two beams becomes:

$$\Delta L = L_{CW} - L_{CCW} = 2\Delta l = 2\Omega R t_R = \frac{4\pi\Omega R^2}{c} \quad (1.33)$$

Corresponding time delay and phase shift for N number of turns of optical path are given as:

$$\Delta t = \frac{\Delta L}{c} = \frac{4\pi\Omega R^2}{c^2} N \quad (1.34)$$

$$\Delta\phi = 2\pi f \Delta t N = \frac{2\pi c}{\lambda} \Delta t N = \frac{8\pi^2 R^2}{\lambda c} N \Omega \quad (1.35)$$

Here,  $f$  is the optical frequency, and the total optical path is equal to  $2\pi RN$ . The resulting phase shift between counter-propagating waves can be calculated after some simplifications using [5];

$$\Delta\phi = \frac{2\pi LD}{\lambda c} \Omega \quad (1.36)$$

$\Delta\phi$ : Phase difference due to rotation

$\Omega$ : Rotation rate

$L$ : Total fiber length

$D$ : Fiber coil diameter

$\lambda$ : Wavelength

$c$ : Speed of light

Using Equation (1.36), it can be deduced that a longer optical path creates a bigger phase difference between counter-propagating beams for a unit angular rotation rate increasing the sensitivity of the gyroscope. Similarly, the final phase shift is proportional to the optical frequency of the beam; i.e., inversely proportional to the wavelength of the light source. Hence, shorter wavelengths yield higher sensitivity which is one of the main topics of this study.

Scale factor (SF) determines the relation between input and output which are rotation rate and phase shift due to rotation, respectively.

$$SF = \frac{\Delta\phi}{\Omega} = \frac{2\pi LD}{\lambda c} \quad (1.37)$$

For a sensitive gyroscope, it is expected to measure Earth rotation ( $15^\circ/\text{hr}=7.3 \times 10^{-5}$  rad/s) in a static state. For example, when  $L=1000\text{m}$ ,  $D=10\text{cm}$ ,  $\lambda=1550\text{nm}$  values are used as the fiber optic gyroscope (FOG) parameters, the SF value is calculated

as 1.4s using Equation (1.37). In this case, the phase difference that a FOG photodetector measuring earth rotation must detect is derived from Equation (1.36) and is found as  $\Delta\phi = SF \cdot \Omega = 9.8 \times 10^{-5}$  rad. The average power change that the obtained Sagnac phase difference value in the photo detector is calculated using Equation (1.38).

$$\langle P \rangle = \frac{P_0}{2} [1 + \cos \Delta\phi] \quad (1.38)$$

$\langle P \rangle$ : Average power of the interfering waves.

$P_0$ : Detector power when there is no phase difference.

Since the value obtained in this calculation based on the Earth's rotation is quite small, it is difficult to measure the changes in this value under rotation. However, with the developing optics and optoelectronic technology, it is possible to measure very sensitive values. Depending on the applications, the architectural design, components and parameters of the FOG optical path can be optimized.

As a priority to optimization, in order to prevent linear and non-linear errors that may occur along the FOG optical path at the most basic level, it is important to comply with the rule of reciprocity (mutual symmetries). This means that the numbers of all transmissions (transmittance) and reflections (reflectance) are equal in the optical path starting from the light source to the detector.

## 1.2 Gyroscope Types

All optical gyroscopes depend on the Sagnac effect however their measurement techniques differ from each other. Ring laser gyroscope (RLG) consists of a monoblock glass-ceramic resonator and active gas medium. Inside the cavity, emitted counter-propagating beams have interfered with the output mirror. The beat frequency of a signal is correlated to the rotation rate. There are mainly three fiber optic gyroscope types consisting of interferometric (IFOG), resonant (RFOG) and

Brillouin (BFOG). All of them depend on fiber optic technology. Although IFOG uses a multi-turn of fiber optic coil to create phase shift due to rotation, RFOG and BFOG include a resonator that shifts the frequency of counterpropagating beams instead of phase. RFOG and BFOG differ in the light source that they use. RFOG is simply a passive resonator that uses an external light source while BFOG is a fiber optic version of RLG.

The mechanical dithering is used to mitigate the RLGs lock-in effect which is insensitivity to low-level rotation due to scattering inside the cavity. This dithering degrades theoretical noise performance by at least one order of magnitude [8]. RFOG and BFOG have coherence-related noises. IFOG technology has a noise level very close to its theoretical limit. It is possible to design and produce IFOG with a better noise level than the others.

IFOG operates over a few fringes with about zero phase difference which eliminates the requirement of the light source with narrow spectral bandwidth. On the contrary, RLG, RFOG and BFOG create a light with a narrow spectrum that causes coherence noises. This is the main advantage of IFOG compared to other technologies.

### **1.2.1 Ring Laser Gyroscope**

For one round trip in a single optical path, the phase difference due to rotation is so small that it is not measurable. A ring laser cavity was used as a multi-pass medium that escalates the Sagnac effect in the early 1960s [5]. In the 1980s, RLG was well-developed technology [8]. RLG has been a very useful and reliable tool for inertial navigation systems. Even today, it is one of the most commonly used rotation-sensing elements.

The emitted wavelength is an integral multiple of the laser cavity as in the Fabry-Perot cavity. In Figure 1.3, a ring cavity can be used to create an optical resonance condition.

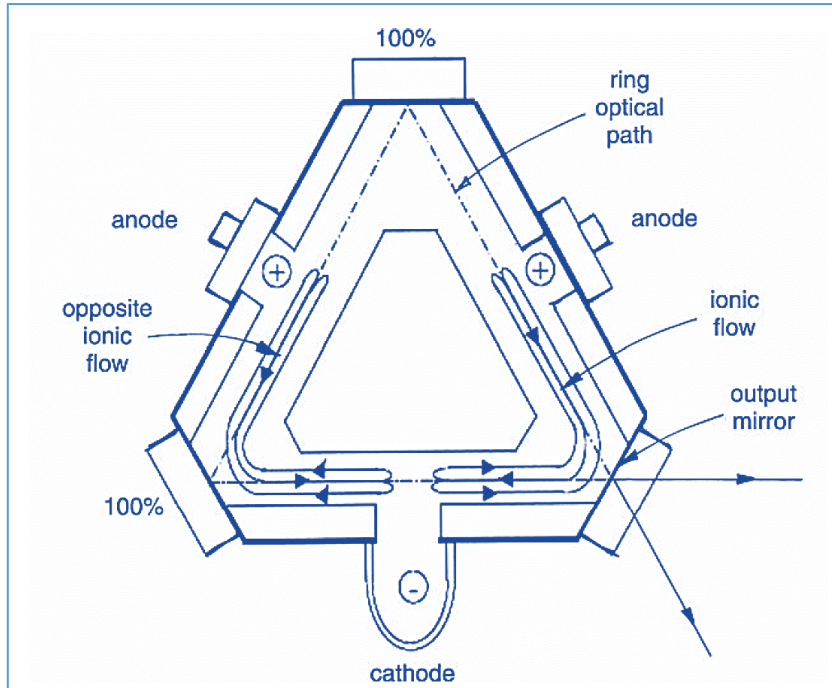


Figure 1.3. RLG schematic [5]

The laser cavity consists of at least two mirrors with high reflectivity and one output mirror that has a low transmission used as output. Inside the cavity, a gas mixture is used as a gain medium. Electrically excited atoms emit light in both directions. When there is no rotation, the optical path of both lights is the same. Therefore, counter-propagating lights have the same wavelength (or frequency). When the cavity is subjected to a rotation, light traveling in the same direction experience a longer optical path while counter-propagating light travels a shorter path. The resulting frequency difference due to the Sagnac effect is given as [8]:

$$\Delta f_R = \frac{4A}{\lambda L} \Omega_R \quad (1.39)$$

Here,  $A$  is the total area enclosed by the ring resonator,  $L$  is the perimeter of the cavity, and  $\lambda$  is the wavelength when there is no rotation. The lateral component of Earth's rotation at a latitude of approximately  $45^\circ$  is  $10^\circ/hr$  ( $=4.9 \times 10^{-5} \text{ rad/s}$ ). For an RLG with an equilateral triangular cavity of 13.2 cm for each side and a HeNe laser operating at a wavelength of 633nm, the frequency shift is 5.9Hz.

RLG has a resonant cavity with a high finesse that creates a laser emission with a very narrow bandwidth. Equation (1.39) uses a single frequency for calculation. The performance limit of an RLG is determined by its capability to distinguish the frequency of the counter-propagating beams. The bandwidth of the beams determines the performance limit so called the fundamental limit of RLG. Therefore, it is crucial to have a narrow bandwidth laser source as in HeNe lasers [8].

The Sagnac frequency difference is measured via interfering two counter-propagating beams. Interference creates a beat frequency at the output mirror and the signal is detected using a photodetector. The relation between the frequency difference and the resulting phase shift is given as:

$$\Delta\phi = 2\pi\Delta f_R t \quad (1.40)$$

and the interference intensity  $I$  is modulated at the beat frequency  $\Delta f_R$ :

$$I = I_0[1 + \cos(2\pi\Delta f_R t)] \quad (1.41)$$

Here,  $I_0$  is the maximum amplitude of the interference signal.

## 1.2.2 Fiber Optic Gyroscope

### 1.2.2.1 RFOG

In RFOG, a passive cavity with an external light source is used as an alternative design to active sensor RLD. The aim is to overcome the lock-in (limits sensitivity) and ion flow (creates bias signal) inside RLG. An external source is directed to the fiber cavity that acts as a Fabry-Perot interferometer and the angular rate creates a frequency shift between counterpropagating two beams inside the cavity. An architecture example for RFOG is given in Figure 1.4.

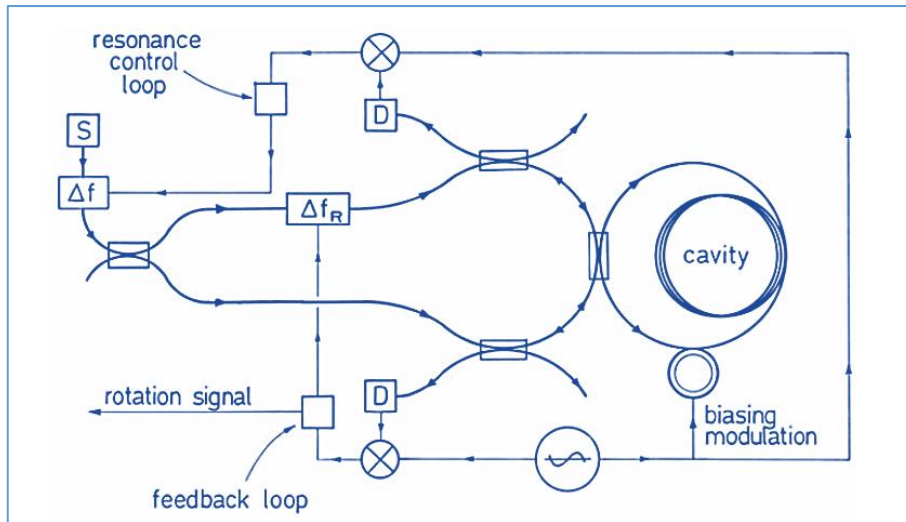


Figure 1.4. RFOG architecture [5]

RFOG design has the advantage of using a shorter length of the optical fiber when compared to IFOG. Complex calibration methods have been developed to suppress temperature effect. Although, shorter wavelengths are more effected by Faraday effect, using soft ferromagnetic alloy with very high permeability shields against magnetic field [9]. However, shorter fiber will significantly reduce the environmental effect such as temperature changes, and external magnetic field and fiber losses will be less affected which requires lower optical power [10]. Additionally, smaller volumes and mass will be available due to the compact design [11].

RFOG technology is still under development process and there is no commercially available product yet. However, it attracts the attention of many research groups due to its mentioned advantages [5].

### 1.2.2.2 BFOG

BFOG has a simple architectural design and high dynamic range which makes them attractive for many applications. The optical power of the light source is needed to be very high in order to enhance stimulated Brillouin scattering inside the resonator.

Rotation of the system results in frequency shift for counterpropagating beams. Beams are combined and create a beat frequency [12], [13]. Figure 1.5 shows a BFOG schematic.

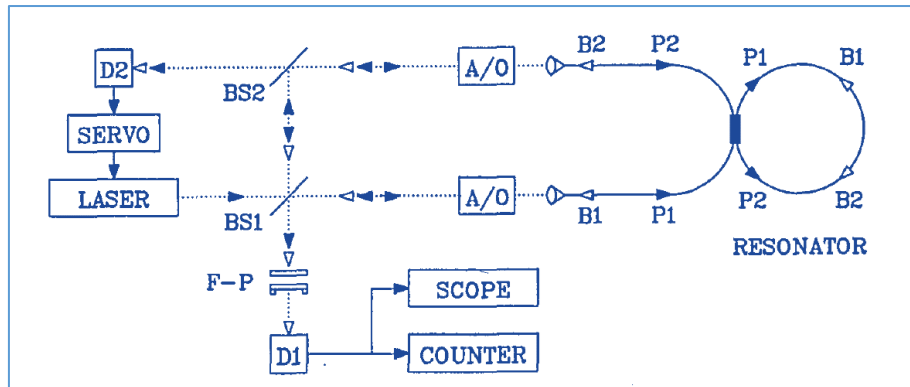


Figure 1.5. BFOG architecture [13]

BFOG suffers from a lock-in phenomenon similar to RLG. A variety of techniques are required to overcome the problem such as mechanical dither, inter-cavity phase modulation, and intensity modulation of the light source [14]

### 1.2.2.3 IFOG

A basic FOG consists of a light source, a coupler, a fiber coil and a photodiode. The output of the light source is split into clockwise (CW) and counter-clockwise (CCW) directions via a coupler. During the rotation of the system, CCW and CCW waves experience a phase shift. Phase shift creates a change in inference output at the coupler. Power chance is received at the photodiode. This passive interferometer system is illustrated in Figure 1.6.

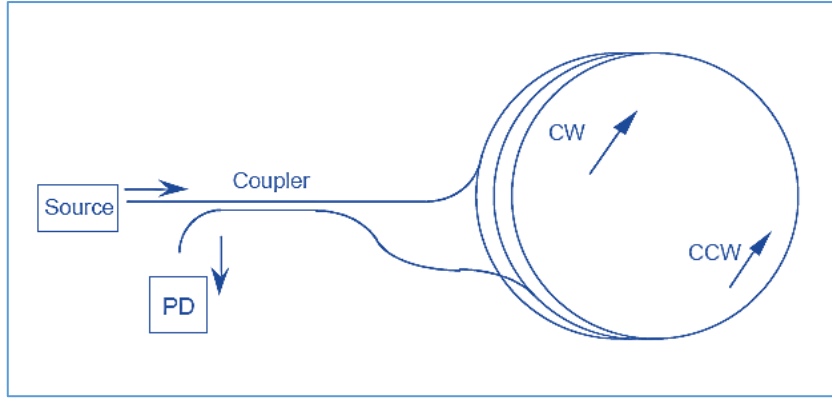


Figure 1.6. Basic schematic of FOG [15]

The rotation-induced phase shift is called as Sagnac Effect and it is the basic principle of all types of optical gyroscopes. Phase shift and rotation rate relation is given as[5]:

$$\Delta\Phi_R = \frac{2\pi LD}{\lambda c} \Omega_R \quad (1.42)$$

$\Delta\Phi_R$  is rotation-induced phase shift,  $L$  is total fiber length,  $D$  is fiber coil diameter,  $\lambda$  is the wavelength of a light source,  $c$  is the speed of light,  $\Omega_R$  is rotation rate.

The phase shift due to rotation is measured by comparing two main counter-propagating beams. In the real world, spurious reflections especially at the splice point of fibers. These reflections create a disturbance in the interaction of the main beams. High-sensitivity IFOG includes a special type of fiber called polarization maintaining (PM) fiber in order to suppress this mitigation. Details of operational principles are given in Section 2.1.2. High birefringence which is a refractive index difference between the orthogonal axes of PM fiber interrupts the temporal coherence between main counter-propagating beams and spurious beams. As a result, this acts as a temporal filter.

Additionally, the importance of light source and noises are explained in detail in the next sections

### 1.3 Digital Scheme

As explained in previous sections, the optical signal output at the photodetector is the outcome of the interference of the two-counter propagating optical waves. Optical power is time dependent parameter and is converted to digital quantity via digital conversion.

According to Equation (1.38), the IFOG has low sensitivity at low angular rate values (i.e.,  $\Delta\phi$  is small). Output signal has maximum sensitivity with respect to the angular rate at  $\Delta\phi$  equals to  $\pm\pi/2$ . Therefore, it is possible to add a phase modulation ( $\Delta\phi_m$ ) additional to phase change due to rotation ( $\Delta\phi_R$ ) [5].

$$P = \frac{P_0}{2} [1 + \cos (\Delta\phi_R + \Delta\phi_m)] \quad (1.43)$$

In this case, the gyroscope will be operating at a significantly higher point sensitivity. In the general case, an optical phase modulator is added after the coupler in Figure 1.6 and the modulation is applied to both CW and CCW signals simultaneously.

Phase modulation is applied using various methods and signal profiles. Two main operational methods are used such as open-loop and closed-loop operations.

#### 1.3.1 Open Loop Operation

Mainly, two signal forms can be applied in order to create phase modulation such as square wave and cosine or sinus modulation. A phase modulator applies square wave phase modulation that creates about  $\pm\pi/2$  phase difference between counter-propagating waves as shown in Figure 1.7.

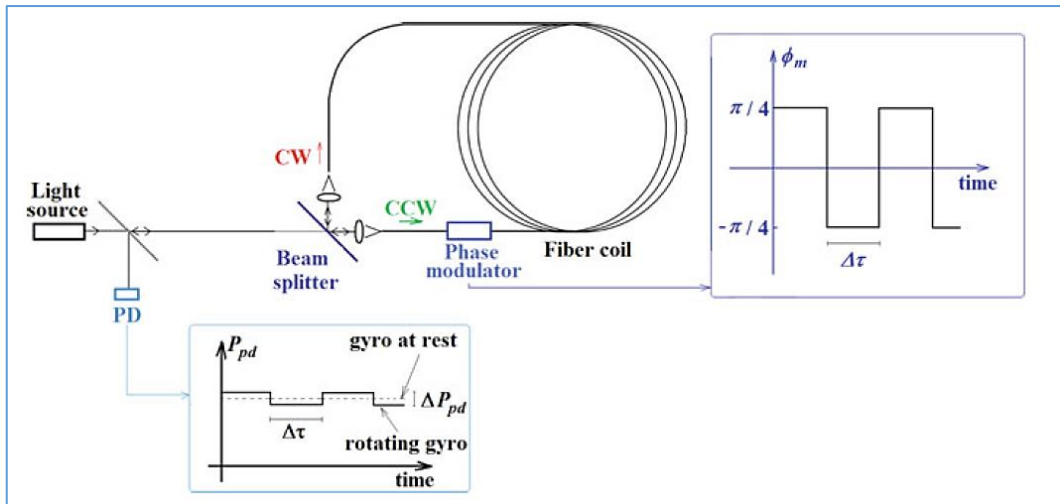


Figure 1.7. Square wave modulation scheme [1]

In the case of rotation, a phase difference is a further shifter and a voltage difference is obtained at each modulation level. The difference between these levels is proportional to the rotation rate. If the gyroscope is at rest, the output signal will be ideally zero.

For the sinus or cosine modulation technique, a phase modulator with a flat frequency response is not required which lowers the system price. An alternating modulation can be applied as given in Equation (1.44) [5].

$$\Delta\phi_m(t) = \phi_m \cos(2\pi f_m t) \quad (1.44)$$

Here,  $\phi_m$  is modulation depth and  $f_m$  is modulation frequency. The modulation and corresponding output signal are shown in Figure 1.8.

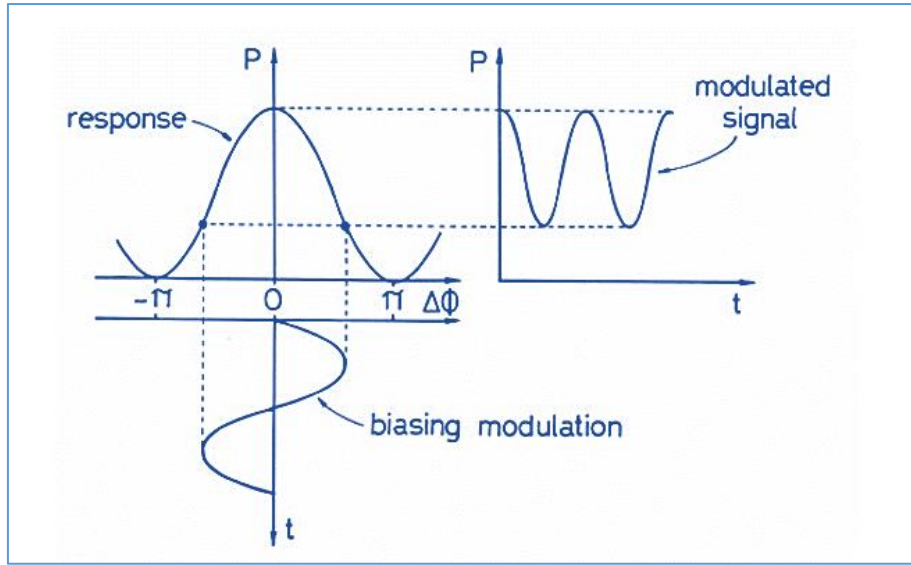


Figure 1.8. Cosine modulation [5]

After several mathematical steps including cosine and Bessel function expansion, odd harmonics that includes biased response can be derived as:

$$P = P_0 J_1(\phi_m) \sin(\Delta\phi_R) \quad (1.45)$$

The output response signal is given mainly by the first odd harmonic of the Bessel function as in Figure 1.9.

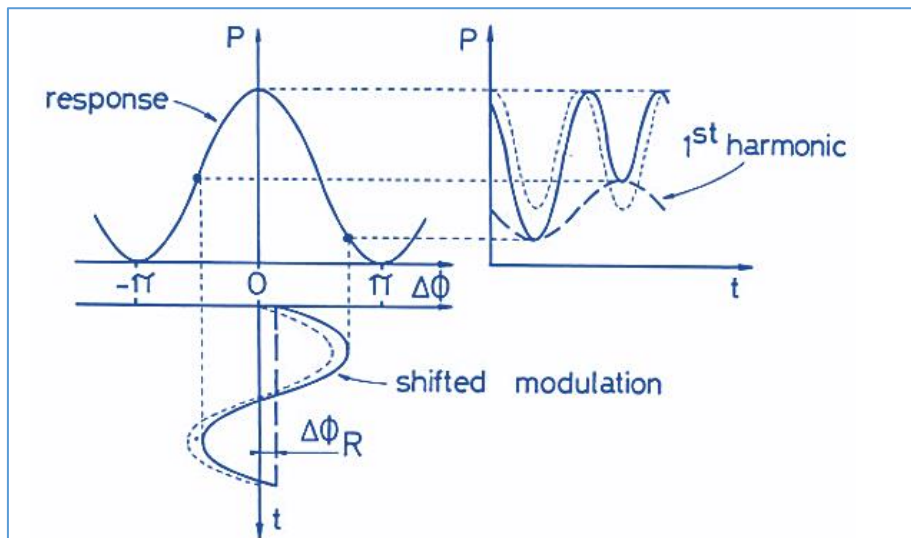


Figure 1.9. Cosine modulation with rotation [5]

### 1.3.2 Closed Loop Operation

IFOG contains an additional feedback loop in the closed-loop configuration as shown in Figure 1.10.

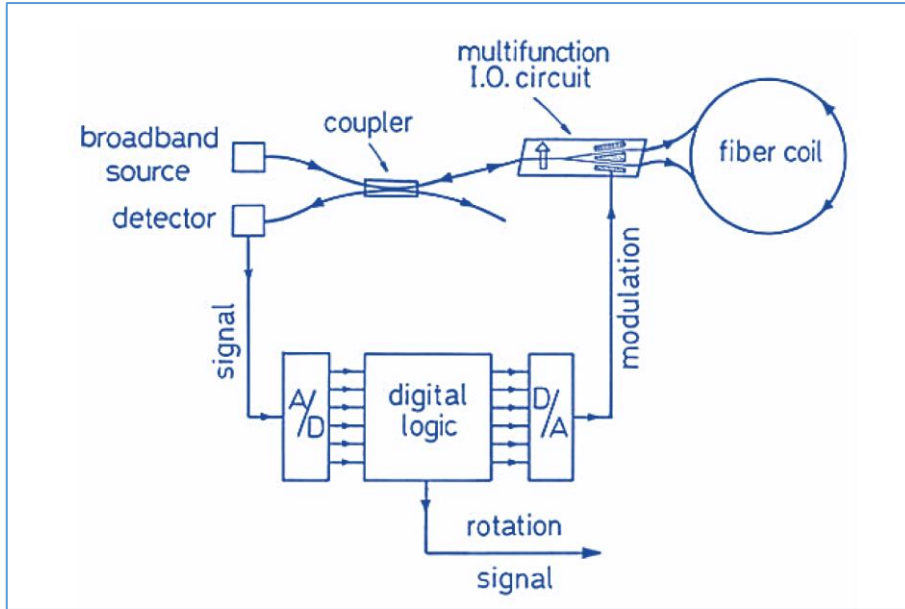


Figure 1.10. Closed-loop architecture [5]

This feedback loop aims to generate a feedback phase shift ( $\Delta\phi_{fb}$ ) that nullifies phase shift due to the rotation. So, a phase shift between the two interfering signals in closed-loop operation which is time dependent is calculated as:

$$\Delta\phi = \Delta\phi_R + \Delta\phi_m - \Delta\phi_{fb} \quad (1.46)$$

The closed loop starts with reading the output voltage of the photodiode with an analog-to-digital converter (ADC). A digital processor calculated the feedback phase shift and the data is converted to an analog signal via a digital-to-analog converter (DAC). Then the analog signal is added to the modulation signal and applied to the phase modulator. Finally, the calculated rotation rate is delivered via a digital processor.

The closed loop method may be executed with a square-wave modulation consisting of two-level and four-level modulation. Several modulation levels depend on modulation points on the interferometer response curve. The half-period of both modulation techniques is equal to the total flight time inside the fiber coil ( $\Delta\tau_g$ ). The relation between flight time and eigenfrequency of the fiber coil is given as:

$$f_p = \frac{1}{2\Delta\tau_g} \quad (1.47)$$

Two level-modulation output with and without rotation is given in Figure 1.11.

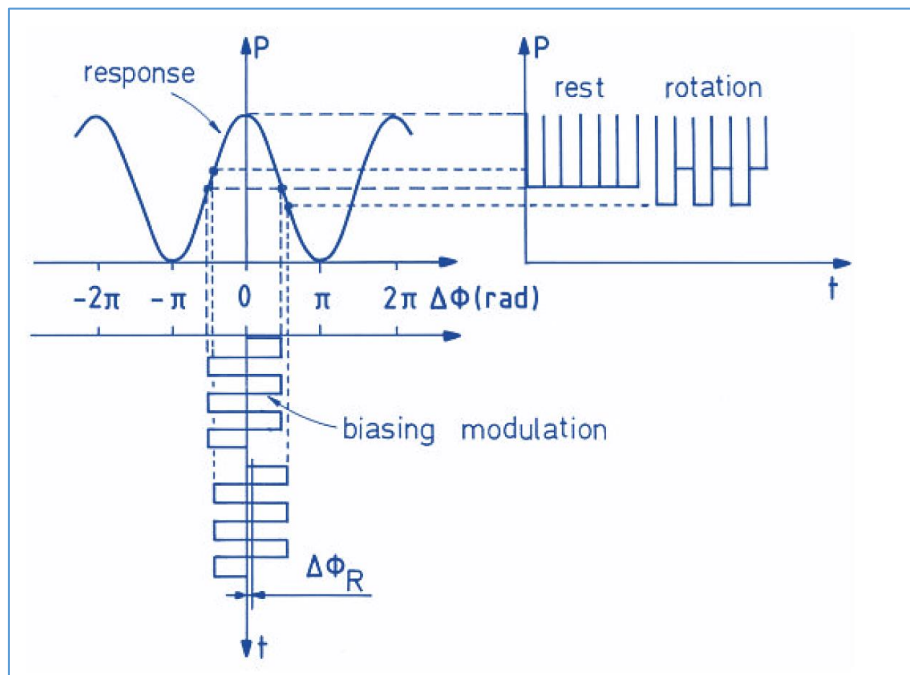


Figure 1.11. Two-level modulation output response [5]

The difference between the values of two-level modulation gives the rotation rate. However, the values of the corresponding point may vary due to temperature effects. The stability of the gain-control feedback loop is significantly increased using four-level modulation whose output characteristic is given in Figure 1.12 and Figure 1.13.

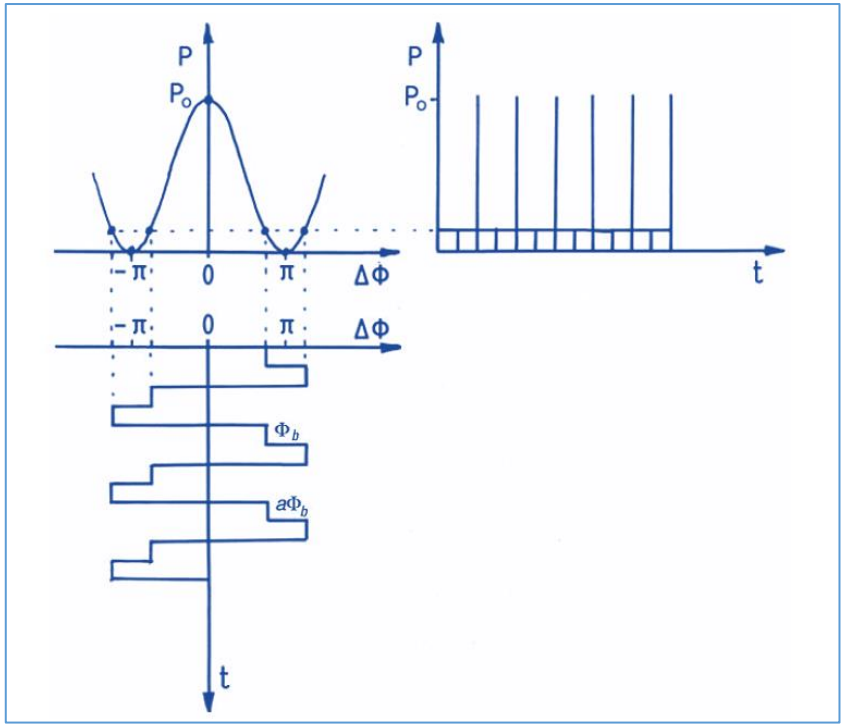


Figure 1.12. Four-level modulation output response [5]

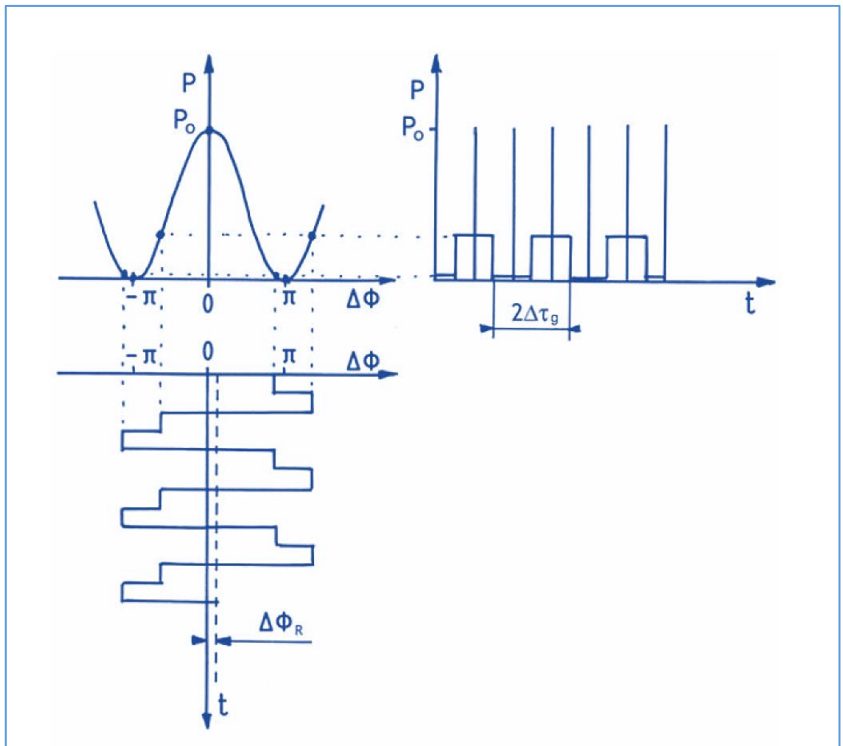


Figure 1.13. Four-level modulation output response with rotation [5]

#### 1.4 State of the Art in Rare-Earth Doped FOG

Many applications require a narrow-band source. On the other hand, interferometry-based applications and several sensors such as gyroscopes require sources having broad bandwidth to suppress coherent errors in addition to high power requirements. At least 5nm broad spectral bandwidth eliminates coherent errors due to Rayleigh backscattering [16], polarization cross-coupling [17], and the Kerr effect [18]. Phenomena of interferometry require single operation as in single-mode fibers. Depending on the application, several milliwatts of the light source are required for an improved signal-to-noise ratio. One of the most critical parameters is mean wavelength stability with respect to temperature change or other environmental effects. The stability of the spectrum determines the stability of the relation between input rotation and output of the gyroscope.

Although, there are studies that use lasers as a source in IFOG, Amplified Spontaneous Emission (ASE) sources are the most common choice for IFOG light sources [19]. Especially, fiber sensors such as IFOG motivated scientists to further development of Er-doped superfluorescent fiber sources (SFS) in this manner.

Superluminescent laser diode (SLD) is another attractive source in IFOG [20]–[22]. Miniaturized size and broadband spectrum make them suitable for many applications. However, they have a high-temperature dependency on mean wavelength in the order of hundreds of ppm. This results in the requirement of high-temperature stability which may not be so practical.

Using an ASE source is advantageous under stringent environmental conditions and broad operating temperature ranges. Rare-earth doped fiber-driven ASE sources are optimized in terms of broad spectrum, optical power, and mean-wavelength stability [23]. Many design configurations have been studied in order to further improve power and wavelength stability performance under different temperature ranges [24], [25]. As detailed in Section 3.3, the white noise of a FOG is generally limited by optical noises. A broader optical spectrum decreases the optical noise

contribution. In this manner, new methods such as gain flattening have been developed [26]. Optical noise namely excess relative intensity can be reduced by monitoring the noise and subtracting it from correlated signal power [27]. Besides, stabilizing the central wavelength is another critical task for improved FOG performance. Some portion of the emission spectra of rare-earth element doped fiber is enhanced for further spectral stabilization [28].

Yb-doped gain medium has many attractive features including a broad gain spectrum, higher efficiency and more radiation resistance compared to Er-doped fibers [23], [29], [30]. Radiation creates point flaws in amorphous silica ( $a\text{-SiO}_2$ ) through ionization which increases. Additionally, energy level lifetimes of rare-earth-doped fiber versus doses of various radiation types is affected drastically. Energy level of Yb-doped fiber is less affected compared to Er-doped fiber especially for high loss of radiation which is critical for future long-term operations [31], [32]. However, Er-doped fiber has been commonly used due to its lower propagation losses, low-cost telecom components. An optical spectral region around  $1\mu\text{m}$  was used in FOG in order to increase sensitivity [33]. However, the advantages of a Yb-doped ASE source operating at  $1030\text{nm}$  were demonstrated in this study.

In this thesis, a novel interferometric fiber optic gyroscope is demonstrated. During the study, a Yb-doped fiber-based ASE source is used as the light source of IFOG. The ASE source has a broad spectrum in order to suppress coherent errors and higher power for enhanced signal-to-noise ratio (SNR). Central wavelength and a broad spectrum of light sources enable to have better sensitivity. A novel control loop inside the ASE structure is used for further improvement in SNR with respect to optical power. There are four main chapters in this dissertation including the Introduction chapter.

Chapter 2 examines IFOG architecture including active and passive optical components. Fiber types, optical components optical sources and optoelectronic components are explained in detail. Additionally, emphasis is given to Yb-doped fiber-driven ASE sources including simulation and test results of the source for

various fiber lengths and pump power levels. Performance is tested at a temperature range of  $-40/+60^{\circ}\text{C}$ .

In Chapter 3, the noise characteristic of IFOG is analyzed. First, specific noise types for a gyroscope are explained. After the noise output of an IFOG is characterized, various noise sources of Angular Random Walk (ARW) which is one of the main noise components are examined in detail. Theoretical analysis is given for ARW and SNR performance in the final sections.

The last chapter includes experimental test results of IFOG including specifications components used. The fiber optic coil which is the heart of the gyroscope is also characterized. Finally, ARW is investigated using the Allan variance analyze method.



## CHAPTER 2

### IFOG ARCHITECTURE

#### 2.1 Fiber Types

The fiber types used in fiber optic gyroscope technology depending on the application area and requirements can be divided into three groups such as single mode (SM), polarization maintaining (PM) and active fibers.

##### 2.1.1 Single Mode Fiber

As in the telecom industry, standard SM fibers are also used in fiber optic gyroscopes. It is preferred due to its low price and easily adaptable structure to the systems. Fiber structure basically; consists of a core, cladding and coating. Standard SM cables are available in the market. The most commonly used and low-cost SM fibers are SMF-28e+ and HI1060.

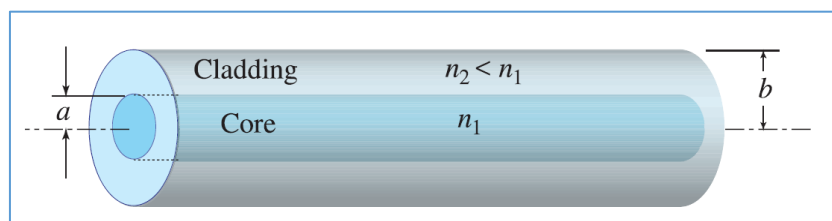


Figure 2.1. Fiber cable [7]

##### 2.1.2 Polarization Maintaining Fiber

In ordinary single-mode fibers, the beam travels with two polarization modes perpendicular to each other. Ideally, the beam travels at the same speed in these two

modes. However, these two modes cannot propagate at the same speed due to the roughness, temperature, vibration and bending that occur in the production of the fiber. For this reason, one mode travels faster or slower than the other and there is a phase difference between these two modes. This phenomenon is called Polarization Mode Dispersion (PMD).

Before 1980, the polarization modes of light traveling through a single-mode fiber could not be controlled due to a lack of technology. Due to birefringence, the beams in different modes reach the detector at the end of the optical path. This introduces phase differences. The polarization control problem creates non-reciprocity in the system which results in measurement errors.

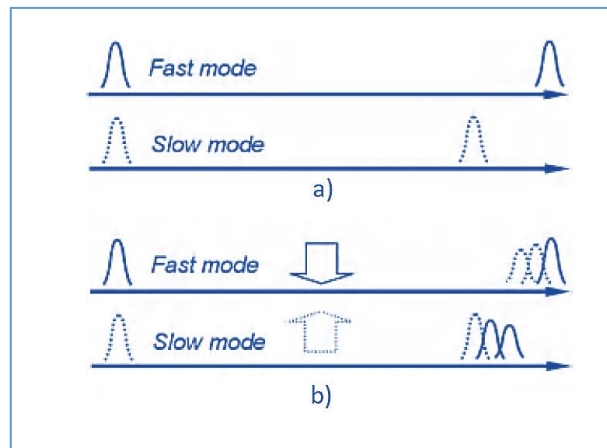


Figure 2.2. PMD effect a) without and a) with mode coupling [34]

There is no method to discard PMD. Therefore, the method of increasing the phase difference between two orthogonal modes is preferred. PM fibers increase the birefringence of the fiber to increase PMD so that the mode on the fast axis can travel normally along the fiber, while the mode on the slow axis is delayed and separated over time.

There are two methods to increase the birefringence of fiber material: Geometrical effect and stress-induced effect. The geometric effect is created with the production of the fiber center in an asymmetrical structure. The stress effect is obtained by producing the structures around the fiber center with asymmetric refractive indices.

PM fibers with geometric effects have more optical losses due to their structurally large refractive index difference and deformities of the center. Stress-induced PM fibers have low optical losses and low cross-talk.

The polarization extinction ratio (PER) is the ratio of the powers of the beam traveling along the fiber path along the vertical axis and the beam traveling along the horizontal axis. It is expressed in units of [dB] [34].

$$PER(L) = \frac{P_{\perp}(L)}{P_{\parallel in}} = h \cdot L \quad (2.1)$$

$P_{\perp}(L)$ : Vertical polarization mode

$P_{\parallel in}$ : Parallel axis input polarization mode

$h$ : h-parameter

$L$ : Fiber length

The h-parameter in commercial PM fibers is typically between  $10^{-6}$  and  $10^{-4}/\text{m}$  [3]. The PER value of a 1km coil is about 30dB.

Different types of PM fibers are given in Figure 2.3. Their names are derived by analogy with their shape. The most preferred types for fiber optic gyroscopes are Panda and bow-tie types with stress bars. Bow-tie fibers are more difficult and expensive to manufacture than the Panda type but have better PER control.

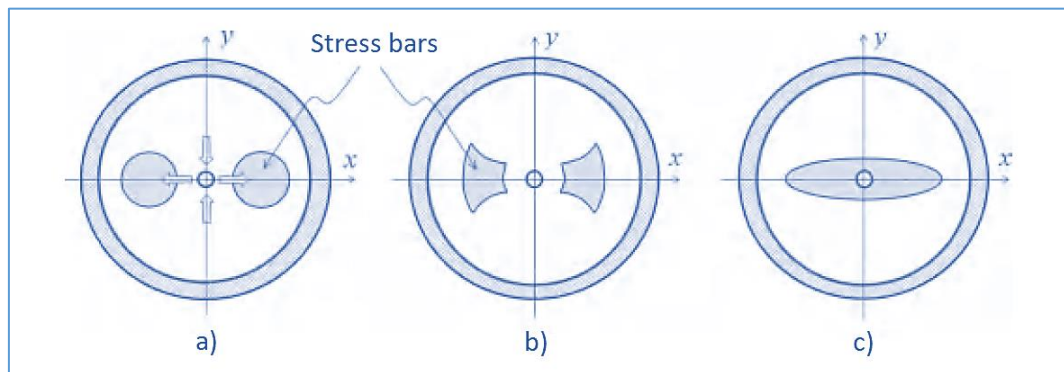


Figure 2.3. PM fiber types a) panda b) bow tie c) elliptical [34]

In panda and bow-tie type PM fibers, refractive index differences are created axially around the center where the light travels, with the effect of stress bars. The axis with stress has a low index and the axis without stress has a high refractive index. The difference in refractive index between the axes creates birefringence which is displayed in Figure 2.4.

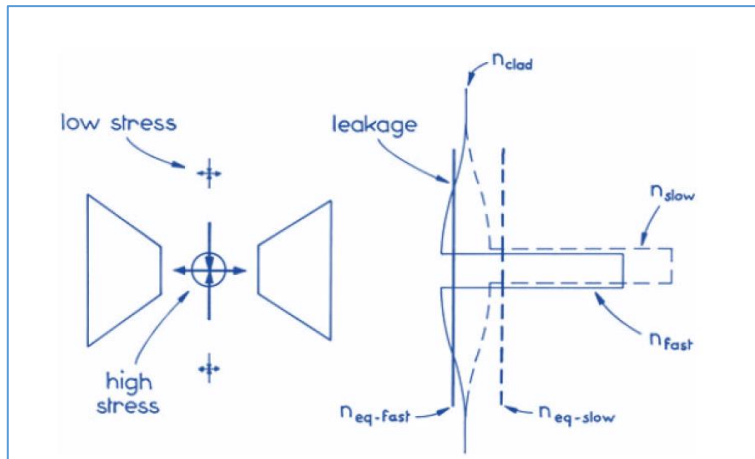


Figure 2.4. Fast and slow axes with the effect of stress bars in PM fiber [5]

The birefringence characteristic of PM fibers depends on their beat length. PM fibers with short and long beat lengths are available. The beat length is shown in Figure 2.5.

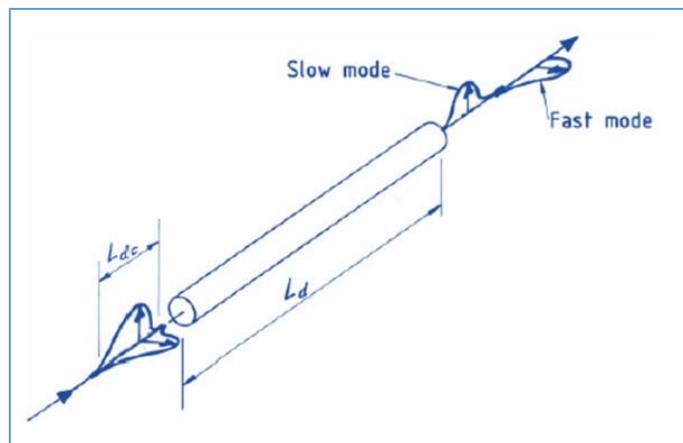


Figure 2.5. PMD, decoherence length and beat length [5]

Beat length is a cycle of periodically changing polarization along the PM fiber and is calculated as [5]:

$$\Lambda = \frac{\lambda}{\Delta n_b} \quad (2.2)$$

$\Lambda$ : Beat length

$\Delta n_b$ : Birefringence

$$\Delta n_b = n_{fast\ axis} - n_{slow\ axis} \quad (2.3)$$

Typically,  $\Delta n_b = 5 \times 10^{-4}$ . When operating at a wavelength of 1550 nm, the beat length ( $\Lambda$ ) becomes 3.1mm.

Depolarization is the loss of correlation between the phase difference between the beam modes traveling at different speeds due to the difference in the refractive index between the axes. The decoherent length ( $L_{dc}$ ) depends on the light source used.

$$L_{dc} = \frac{\lambda^2}{\Delta \lambda_{FWHM}} \quad (2.4)$$

Here,  $\Delta \lambda_{FWHM}$  the bandwidth of the light source at full-width half maximum. Depolarization length ( $L_d$ ) and decoherent length ( $L_{dc}$ ) are proportional to beat length and wavelength.

$$\frac{\Lambda}{\lambda} = \frac{L_d}{L_{dc}} \quad (2.5)$$

Accordingly,  $L_{dc} = 300 \mu\text{m}$  and  $L_d = 60 \text{ cm}$  formed by a light source with a wavelength of 1550 nm and a bandwidth of 8 nm. With the depolarization length, the fiber length ( $L$ ) in the coil can be modeled using the equation  $L = N \cdot L_d$ .  $N$  is the number of depolarization lengths [5].

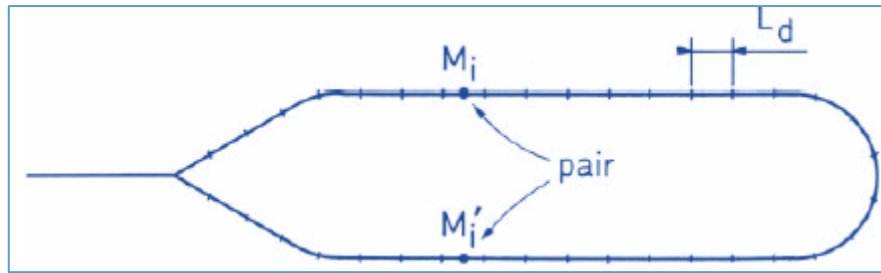


Figure 2.6. Symmetrical depolarization lengths [5]

Birefringence maintains linear polarization in the fiber. The axial power change depending on polarization grows linearly through the path. The average power transfer rate from one polarization to another in the fiber is expressed as the parameter  $h$ .  $h$  parameter of a PM fiber is  $3 \times 10^{-5}/\text{m}$  to  $1 \times 10^{-5}/\text{m}$  typically [5].

Elliptical core fiber is used in tactical fiber optic gyroscopes in the market. It provides efficient and sufficient polarization continuity in tactical-level products. However, due to the elliptical nature of the center in such fibers, the birefringent index difference ( $\Delta n_b$ ) is significantly dependent on the wavelength and the power loss between the core and cladding is greater. Therefore, it is not used for higher accuracy levels.

Typically, fibers used in the Telecom industry have a core/clad diameter of 125/250  $\mu\text{m}$ . PM fibers with a core/clad diameter of 80/170  $\mu\text{m}$  are available in fiber optic gyroscopes. These fibers, named reduced cladding diameter, are used to minimize the volume in coil design.

### 2.1.3 Active Fibers

Ions of rare-earth elements are doped inside fiber silica and the resulting material is used as a gain medium of lasers and fiber amplifiers and optically pumped using pump laser diodes [35]. Active fiber technology has many advantages such as excellent beam quality, efficient heat dissipation, high energy efficiency and

compatibility with fiber communication systems. Most commonly used one is Erbium-doped (Er) fiber. The energy level diagram is shown in Figure 2.7.

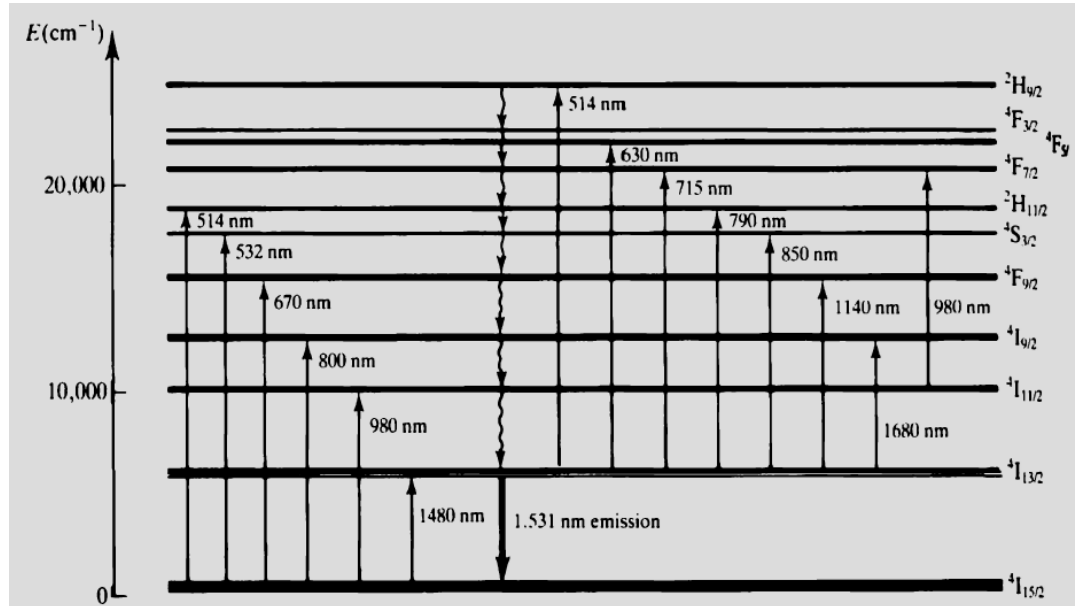


Figure 2.7. Energy level diagram of Er-doped fiber [35]

The lowest loss for silica fibers is around 1550nm and is emitted when pumped around 980nm or 1480nm. This makes Er-doped fiber suitable for long transmission lengths of telecommunication applications. Erbium-doped fiber amplifier systems (EDFA) have been well developed through C-band and L-band with longer wavelengths [35]

Ytterbium (Yb) rare-earth element is another commonly used as a dopant, particularly for high-power fiber lasers where higher efficiency compared to Er-doped fiber is required. In Figure 2.8 energy level diagram of Yb is given which is the two-level system.

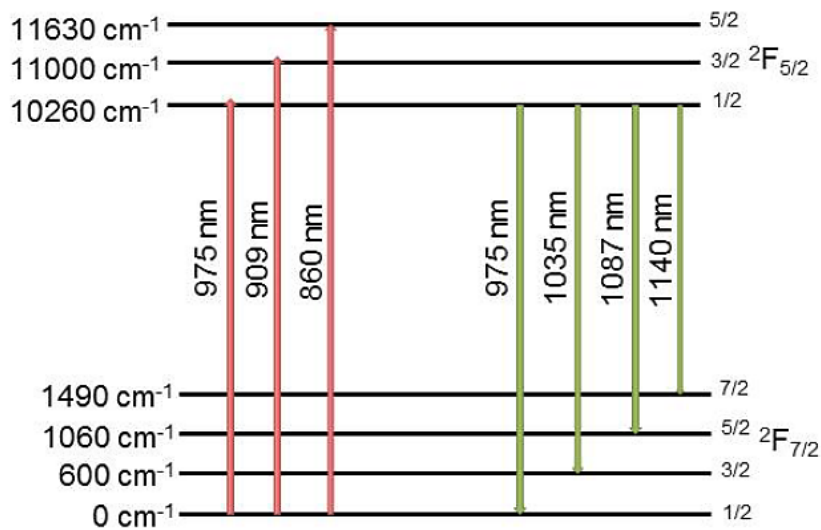


Figure 2.8. Energy level diagram of Yb-doped fiber [36]

The energy levels of the ground-state and excited-state are  $2F_{7/2}$  and  $2F_{5/2}$ , respectively. The broad emission spectrum of Ytterbium which will be discussed further in the next Chapter enables to build highly efficient and tunable system. On the other hand, Erbium has lower efficiency. The segregation effect limits the doping concentration of Er to an order of  $10^{25}\text{m}^{-3}$  which lower the efficiency. Erbium has other disadvantages such as excited-state absorption and lifetime quenching. Different techniques such as co-doping or using new host materials have been developed in order to overcome efficiency problems.

## 2.2 Fiber Coil

The refractive index of the silica material constituting the fiber is affected by environmental temperature and rate of temperature changes. The Shupe effect is the change of the refractive index of the fiber material due to the sensitivity of the fiber material due to the temperature change, causing the light to take different paths and the formation of undesirable phase differences. This effect is dominant in fiber coils that are a few hundred to kilometers long. In order to minimize this problem, it has been tried to ensure that the rays traveling mutually along the coil are exposed to this

effect symmetrically. For this reason, various symmetrical winding techniques have been developed.

The working principle of fiber winding machines which is shown in Figure 2.9 creates a mutual symmetry. It is the rotation of two arms with equal lengths of fiber wrapped around the structure called a mandrel in the middle, forming the fiber coil in turn. The aim is to ensure that the mutually rotating rays travel an equal distance to the midpoint and center axis of the fiber coil.

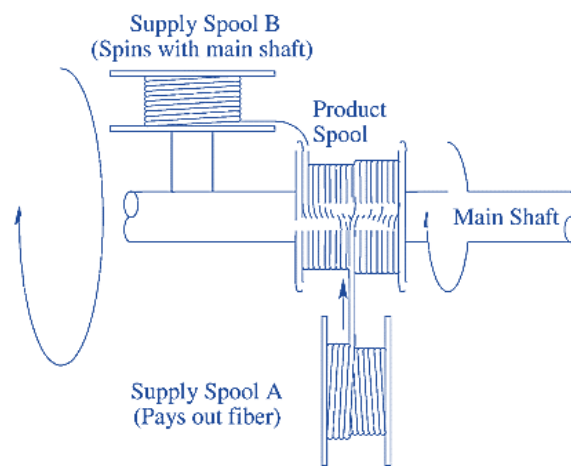


Figure 2.9. Representation of windings in order to create winding pattern [37]

After fiber winding, a free-standing coil can be obtained by removing the mandrel in between. The resulting coil image is given in Figure 2.10. Winding quality is very important during the winding process. It is necessary not to wind using very high tension, to keep the degree of tension constant, to wind the fibers with 2% to 5% of the diameter of fiber between the fibers, to pre-calculate the number of fibers suitable for the mandrel length and the length of the spaces between them.



Figure 2.10. Various fiber coils [38]

Many winding methods have been developed so far. These are dipolar [5], crossover-free [39], double cylinder [40], random wound [40], quadrupole [41] and octupole [42]. The most common winding techniques used for fiber optic gyroscopes today are quadrupole and octupole winding techniques.

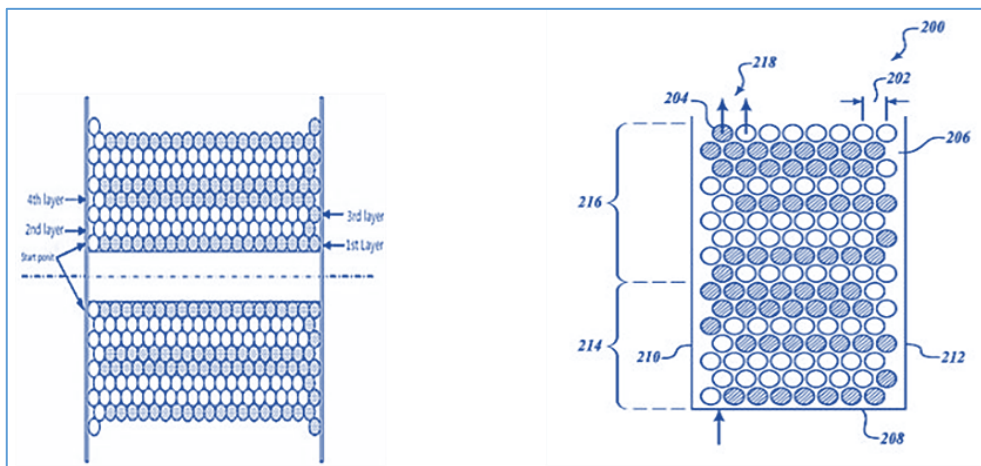


Figure 2.11. Quadrupole and octupole winding patterns [5], [42]

During the winding process, several types of winding defects may occur that result in gyroscope performance errors. The relation between various defects and gyroscope errors is given in Figure 2.12.

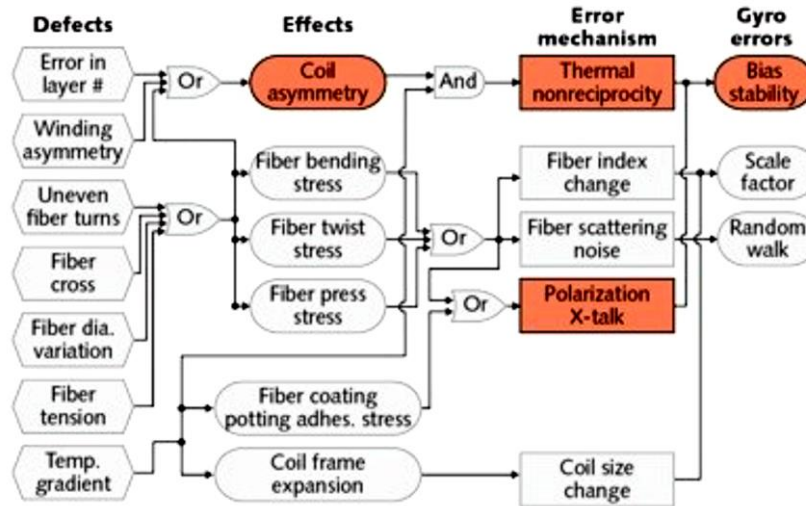


Figure 2.12. Winding errors [43]

Fiber coils can be wound in different lengths and diameters using different winding techniques in order to provide the performance given in the application area. Fiber length and coil diameter parameters are critical parameters that affect gyroscope errors. Details are given in the next chapters.

The fiber material inherently tends to lie flat when released. When the fiber made of Silica material with a glassy structure is bent as shown in Figure 2.13, bending increases the stress in the region of  $T^-$  while the refractive index decreases in the region of  $T^+$  stress. This changes the optimum refractive index between the inner and outer parts. The smaller the radius  $R$ , the greater the probability that the beam will escape from regions of decreasing refractive index, causing bending-dependent loss of power.

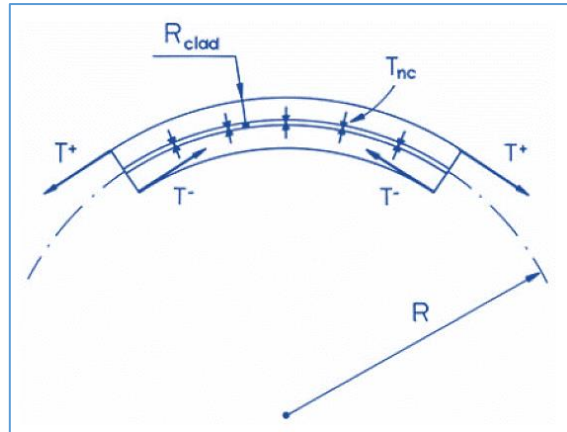


Figure 2.13. Fiber subjected to bending stress [10]

The loss to occur in fiber bending is different in fibers with different Numerical apertures (NA). The following equation can be used to calculate bending loss [44].

$$\alpha_c = 3 \times 10^7 (\Delta n)^{-1/4} (\lambda_{op} R)^{-1/2} \left( \frac{\lambda_c}{\lambda_{op}} \right)^{1/2} \cdot \exp \left( -7.1 \times 10^5 \frac{R}{\lambda_{op}} (\Delta n)^{1/2} \left[ 2.743 - 0.996 \frac{\lambda_{op}}{\lambda_c} \right]^3 \right) \quad (2.6)$$

$\alpha_c$ : Constant bending loss,

$\Delta n$ : Core/clad refractive index difference,

$\lambda_{op}$ : Operating wavelength ( $\mu\text{m}$ ),

$R$ : Bending radius

$\lambda_c$ : Cut-off wavelength propagates at LP11 polarization mode ( $\mu\text{m}$ ).

Bending loss for various NA and coil diameters is given in Figure 2.14.

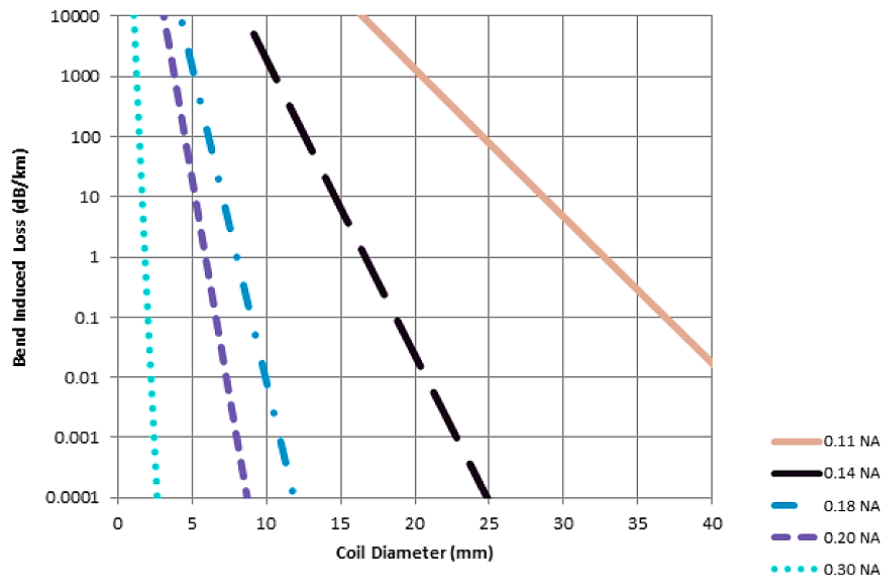


Figure 2.14. Bending loss depending on coil diameter and numerical aperture

### 2.3 Passive Components

In FOG, several types of in-line fiber-coupled passive components are used such as couplers, wavelength division multiplexers (WDM), optical circulators, fiber Bragg grating, and isolators.

Various coupler types are used depending on the design of the optical path in the optical architecture. The working principle of the couplers, which exist in many types in the market, depends on the mode field diameter (MFD) between the fibers that are very close to each other as shown in Figure 2.15.

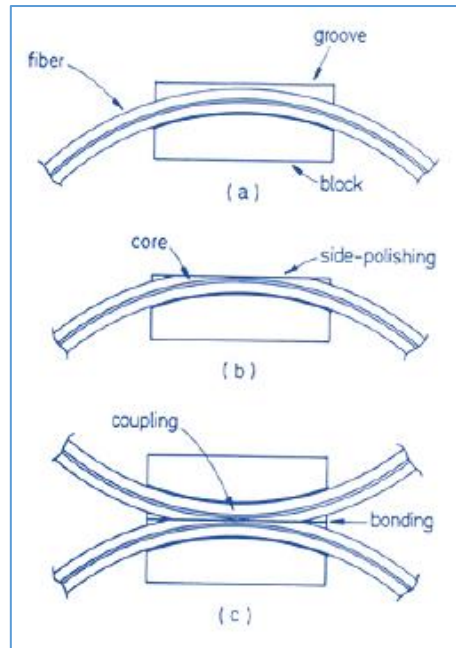


Figure 2.15. Coupling of two fiber using side polishing [5]

The fiber cable is placed inside the silica block. It is polished to a certain length from the clad part to near the core. It is welded with another equivalent fiber cable, with the side of its core by side. Thus, the coupling event occurs along a certain path between the two centers and the electromagnetic wave density is transferred as it propagates.

There are different types of couples available in the market. They are named according to their type and function. There are 2x2 and 1x2 variants of the 50:50 (3dB coupler) divider. They are also called X couplers due to their X-like shape as given in Figure 2.15.

The optical power of incoming light is evenly or selectively distributed over the two fiber arms as it travels similarly to a Y-shape that divides 1:99 (Y or 1x2 coupler). In Figure 2.16,  $P_0$  is the input power,  $P_1$  is the radiated power, and  $P_2$  is the power split into the second fiber.  $P_3$  and  $P_4$  correspond to a low-level signal (-50, -70 dB below the entering beam) due to the back reflection and backscatter errors in the system [3].

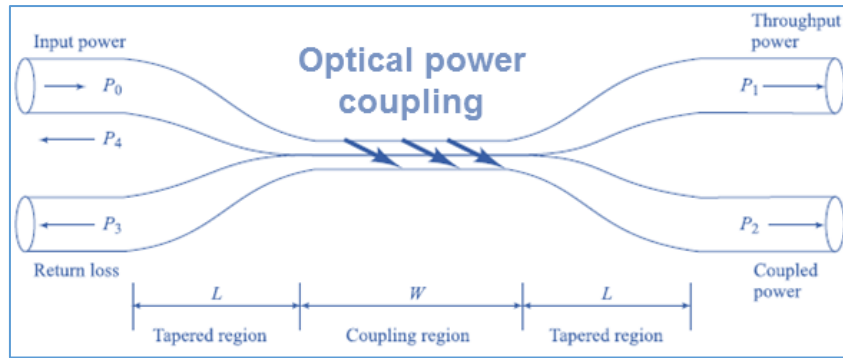


Figure 2.16. Coupler ports

For X coupler:  $P_1 = P_2 = 0.5 P_0$ . Losses in the coupler can be calculated using the following equations.

$$\text{Splitting loss} = \left( \frac{P_2}{P_1 + P_2} \right) \times 100\% \quad (2.7)$$

$$\text{Excess loss} = 10 \log \left( \frac{P_0}{P_1 + P_2} \right) \quad (2.8)$$

$$\text{Insertion loss} = 10 \log \left( \frac{P_i}{P_j} \right) \quad (2.9)$$

$$\text{Return loss} = 10 \log \left( \frac{P_3}{P_0} \right) \quad (2.10)$$



Figure 2.17. Coupler [45]

Some couplers divide the power into 3 in a ratio of 33:33:33. It is a common 1x3 coupler suitable for optical architectural design. If it is required to use a single light source as an input for 3 gyroscopes, a 1x3 coupler can be used.

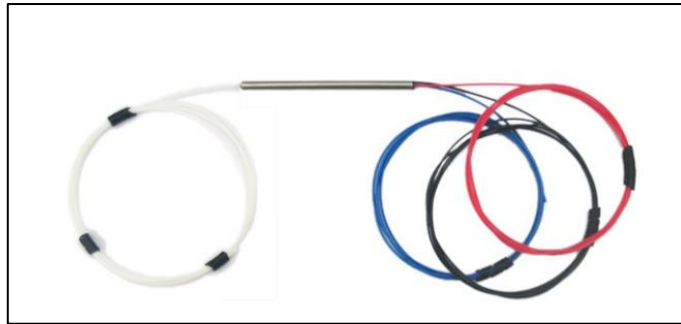


Figure 2.18. 1x3 coupler [46]

Briefly, couplers can be designed depending on application as MxN as in Figure 2.19.

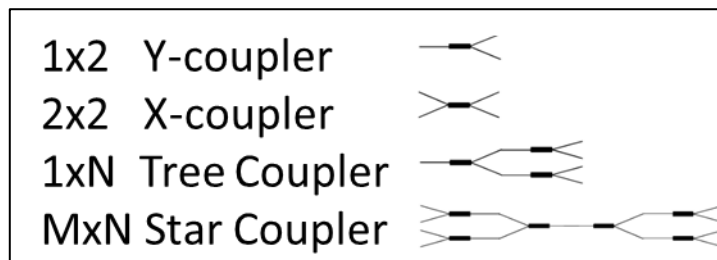


Figure 2.19. Coupler port types

The couplers produced with SM fiber have a length of approximately 10mm and are highly resistant to temperature changes. It can also be produced with any PM fiber. Correct and precise alignment of the stress points of the PM fibers is crucial as shown in Figure 2.20.

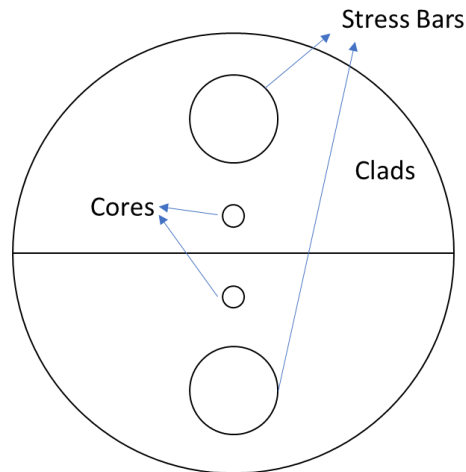


Figure 2.20. Alignment of stress bars of PM fibers

The fiber optic gyroscope may be designed in many spectral ranges. While the wave in the 1520-1570 or 1030-1060 nm spectrum is transmitted to the system, the generation of such wavelength ranges requires 980nm wavelength range pumping. Wavelength Division Multiplexer (WDM) with single-mode fiber has the capacity to combine the wave at 980 nm wavelength are used. There are WDM products on the market designed for different purposes and applications.

WDM products work by multiplying the wavelength (optical multiplexer-mux) in certain band ranges. By increasing the capacity of a single-mode fiber, they show the ability to carry many wavelengths. They can combine and separate many signals of wavelengths to be transmitted.

They can operate at temperatures between -40°C - +85°C. Generally, passive components can continue to operate outside of the operating temperatures usually given in their specifications. Their stability does not change significantly. In Table 2.1, various operational wavelength ranges are given.

Table 2.1. Various operational wavelength ranges

| Band   | Description | Wavelength Range (nm) |
|--------|-------------|-----------------------|
| O-Band | Original    | 1260 – 1360           |
| E-Band | Extended    | 1360 – 1460           |

|        |                      |             |
|--------|----------------------|-------------|
| S-Band | Short wavelength     | 1460 – 1530 |
| C-Band | Conventional         | 1530 – 1565 |
| L-Band | Long wavelength      | 1565 – 1625 |
| U-Band | Ultralong wavelength | 1625 – 1675 |

Filter DWM (FWDM) can transmit multiplexed or single wavelengths 2-way over a single fiber. Owing to its filtering feature, it prevents certain returning wavelengths from continuing on the optical path like an isolator.



Figure 2.21. FWDM [47]

The optical circulator, which is a passive optical component, may have 3 or 4 ports. A beam that moves sequentially between ports (1 to 2, 2 to 3, 3 to 1) cannot return from the same direction.

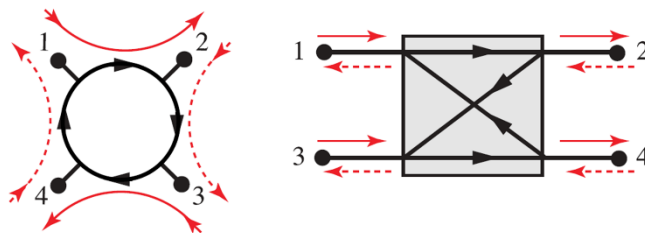


Figure 2.22. 4 port circulator representations [7]

It can be used to give a certain orientation to the light and prevent it from returning. There are circulators in the market that can only be used for 1550nm wavelength.



Figure 2.23. Circulator with 3 ports [47]

Fiber Bragg Grating (FBG) is the structure obtained as a result of periodic or aperiodic differentiation of the refractive index to the fiber waveguide via ultraviolet (UV) radiation. Its total length is about 8-10mm.

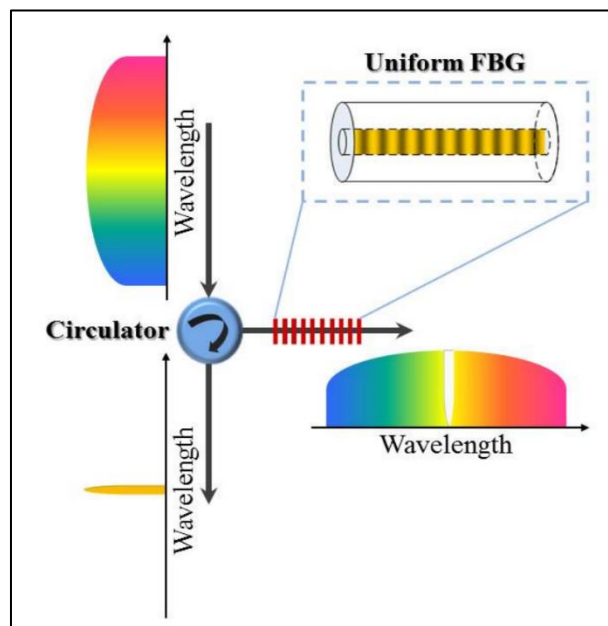


Figure 2.24. FBG refractive index difference [48]

Grating structures show multilayer dielectric mirror properties. These mirrors are transparent glassy structures covered with a thin dielectric material and their thickness is equal to each other. It causes the refractive index to be high-low in sinusoidal variability along the fiber center path. Its surface can reflect 99.99% of

the wavelength studied. The reflected wavelength is the wavelength used in the FOG system. The spectrum of rays transmitted through the FBG is not used.

FBGs, which can be designed in different grating periods ( $\Lambda$ ), reflect rays of different wavelengths according to the Bragg equation [49].

$$\lambda_R = 2n_{SiO_2}\Lambda_{Bragg} \quad (2.11)$$

$\Lambda_{Bragg}$  : Bragg period

$n_{SiO_2}$  : Refractive index ( $\approx 1.45$ )

$\lambda_R$  : Reflected wavelength

The FBG period selected for the study at 1550nm wavelength should be  $\Lambda_{Bragg}$  535nm.

The number of periods ( $N$ ) is inversely proportional to the reflection bandwidth range  $\frac{\Delta\lambda_R}{\lambda_R}$  [5].

$$\frac{\Delta\lambda_R}{\lambda_R} \geq \frac{1}{N} \quad (2.12)$$

According to equation (2.13), FBG with a center wavelength of 1550nm, a period of 535nm and a period of 104 (the grating length corresponds to a 5mm length) is found as  $\Delta\lambda_R$  0.15nm.

The wavelength of the reflected light changes proportionally with the grating period. Consequently, as in Figure 2.25, red light requires FBG with a longer period as it has a longer wavelength.

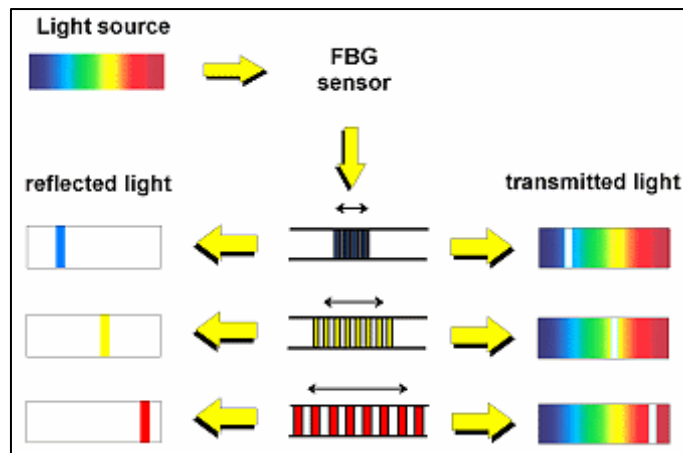


Figure 2.25. Reflection of selected wavelength [50]

Owing to the FBG technology, the wavelength stability of the laser diodes can be increased and the desired wavelengths in the spectrum can be studied. It acts as a kind of in-line optical filter. There are FBG types with different properties and purposes such as uniform FBG, chirped FBG, blazed FBG and superstructure FBG [49].

The grating structure produced with a uniform periodic distribution reflects the optical signal back for a certain wavelength. This type of FBG is generally used to provide wavelength stability in front of laser diodes. Although a beam produced in a laser has a specific wavelength and narrow full width at half maximum (FWHM), wavelength fluctuations occur due to its internal heating or environmental temperature effects. The uniform FBG will not transmit the shifted wavelengths generated during this fluctuation back to the system.

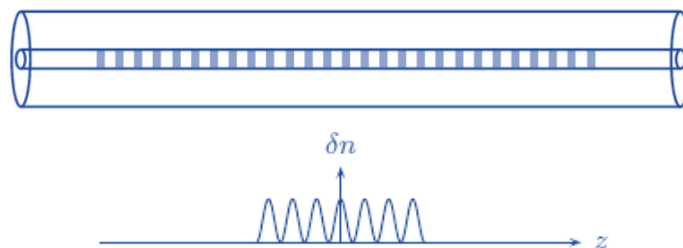


Figure 2.26. Difference of uniform FBG and periodic refractive index

Chirped FBG (CFBG) with increasing periodic distribution can be produced with periods as linear or quadratic functions. With this type of grating, a certain wavelength range can be reflected back. The wave profile to be studied is the reflected spectrum. The FWHM and center wavelength of this spectrum can be tuned with the chirped FBG.

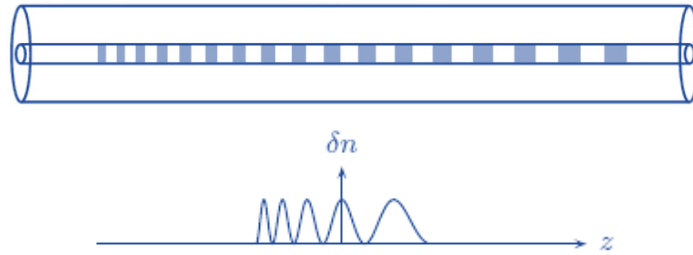


Figure 2.27. Chirped FBG and periodic refractive index difference

Also called Blazed FBG, Tilted FBG, or Slanted FBG in the market. The variation of the refractive index in FBG, which has an oblique grating, is at an angle with respect to the optical axis. The tilt angle affects the reflected wavelength and bandwidth (FWHM). Its curved structure creates a wave with different amplitude by overlapping the nonlinear distribution and 2 linear polarization modes (LP<sub>01</sub> and LP<sub>11</sub>), it has different polarization compared to the first wave and continues on its way in this way [49]. For this reason, Blazed FBG serves to obtain odd-order radiation modes. Inclined FBGs are not used in the fiber optic gyroscope application, since it works in only one mode (LP<sub>01</sub>).

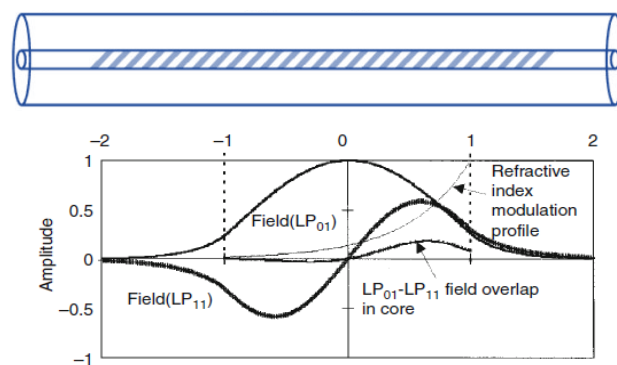


Figure 2.28. Blazed FBG and resulting polarization modes [49]

Superstructure FBG is formed by fabricating sections with co-refractive indices in clusters along the fiber path, spaced at fixed intervals or periodically incrementally. By changing the distance and frequency of the created refractive indices, waveforms with different phase shifts and amplitudes can be reflected.

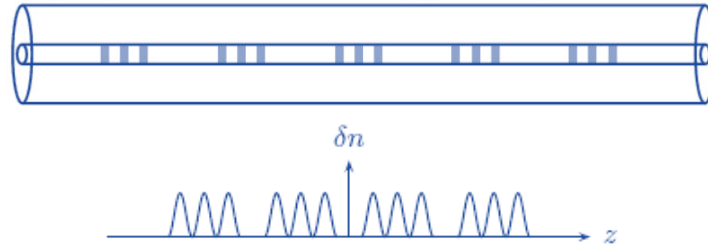


Figure 2.29. Superstructure FBG

Isolators work unidirectionally with the filters used in their structure. It prevents the returning beam from propagating on the optical path. It is especially used at the output light sources. Thus, it ensures that the light source is not damaged or affected by back reflections.

As in Figure 2.30, the beam coming to the isolator is collected by a collimating lens and split with the help of a spacer with high double refraction. Its polarization is controlled with the help of a faraday rotator and half-wave plate. With the help of a spacer with high birefringence, the rays are collected and their continuity is ensured in the optical path. The returning rays, indicated by the red arrows, are blocked on the optical path as they cannot enter in the direction of input.

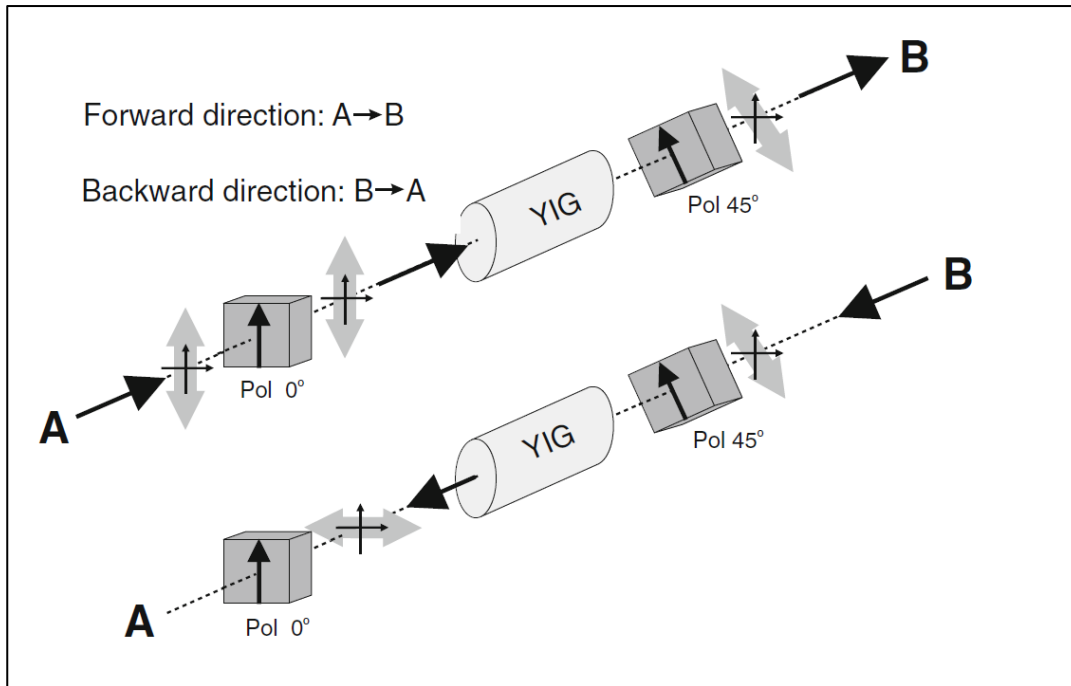


Figure 2.30. Isolator operation principle [51]



Figure 2.31. Isolator [51]

## 2.4 Types of Light Sources

In FOG products, monochromatic wavelength as well as single-mode fibers are used in order to measure the phase difference precisely. In order to prevent non-linear errors that may occur due to the nature of the silica material, a wide FWHM range is preferred instead of operating in a narrow bandwidth (FWHM) of the light source as in the laser. Working with a coherent light source increases the possibilities such as back reflection and scattering. For this reason, light sources with low coherence levels are preferred.

There are critical parameters to consider when choosing a light source. These; which wavelength to work at, FWHM, center wavelength, optical power and stability of the wavelength. With the development of Erbium Doped Fiber Amplifier (EDFA) light source technology in the 1990s, the stability of the light source output optical power has increased. However, with some passive optical components used, FWHM and center wavelength has become adjustable. Before that, in medium and low-performance FOG products, working with ASE principles, but not as stable as Erbium-doped Fiber Source (EDFS); superluminescent laser diode (SLD), Super-radiant Diode (SRD) and light emitting diodes (LED) light sources were used.

In order to better understand light sources and light sensors, the principle of the diode should be explained first. After briefly mentioning the concept of a diode, light source types and light-sensing devices are explained in the next sections.

#### 2.4.1 Diode

A diode is a semiconductor optoelectronic circuit element that only conducts current in one direction. Elements whose resistance in one direction is negligibly small, and whose resistance in the other direction is very large. The direction in which the resistance is small is called the forward direction or conduction direction, and the direction where it is large is called the reverse direction. The diode symbol is in the form of an arrow indicating the direction of the current flow.

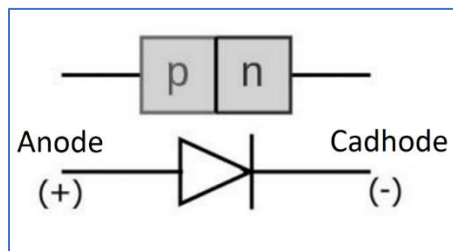


Figure 2.32. Diode symbol

The most commonly used materials used in the construction of semiconductors are silicon and germanium. After these substances are purified and active substances are

added, two different semiconductor substances are obtained P-type and N-type. Basically, the diode consists of an N and a P-type semiconductor placed side by side with a barrier between them.

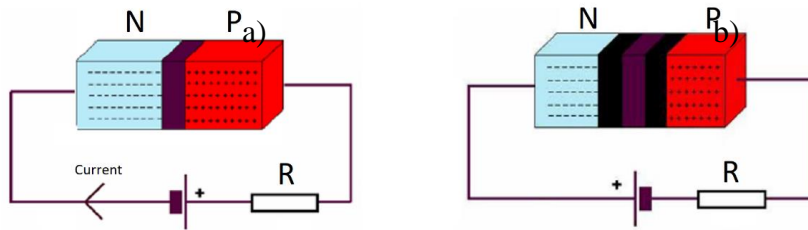


Figure 2.33. (a) Forward biasing of the diode (b) Reverse biasing of the diode  
(Black regions represent electron-free regions.)

When the diode is forward biased and the voltage value to overcome the barrier, the region is applied or exceeded, the current flowing through the diode is called the conduction current  $I_d$ . Normally, the diode should not conduct current in case of reverse polarity. Because the barrier region will become larger with the applied reverse polarity. However, in practice, a very small leakage current flows through the diode in the opposite direction during reverse polarity. This leakage current is called reverse saturation current,  $I_s$ . There is a relationship between the saturation current and the conduction current as follows.

$$I_d = I_s \cdot [e^{\frac{V_d}{n \cdot V_t}} - 1] \quad (2.13)$$

$I_d$ : Diode current

$V_d$ : Applied voltage to the diode

$n$ : Ideality factor

$V_t$ : Thermal Voltage,  $V_t = k \frac{T}{q}$

$I_s$ : Reverse bias saturation current

A typical diode current-voltage variation graph is given in Figure 2.34.

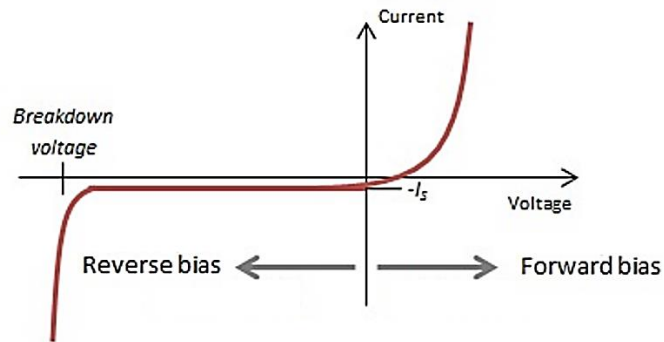


Figure 2.34. Current flowing across a diode versus the voltage applied

When a diode is forward-biased, the diode voltage turns on after a certain threshold voltage, acting as a conductor. When the diode is reverse biased, it allows very little reverse saturation current to pass, even if the voltage increases in reverse. But after a certain feedback voltage, the structure of the diode deteriorates (breakdown) and becomes conductive.

Diodes can be used to serve different purposes by using semiconductor technology and infrastructure. Devices such as laser diode (LD), super bright superluminescent diode (SLD), and light emitting diode (LED) photodetectors are used to generate or detect light. Figure 2.35 shows various diode applications. In the next section document, LD, SLD, LED and detectors will be examined.

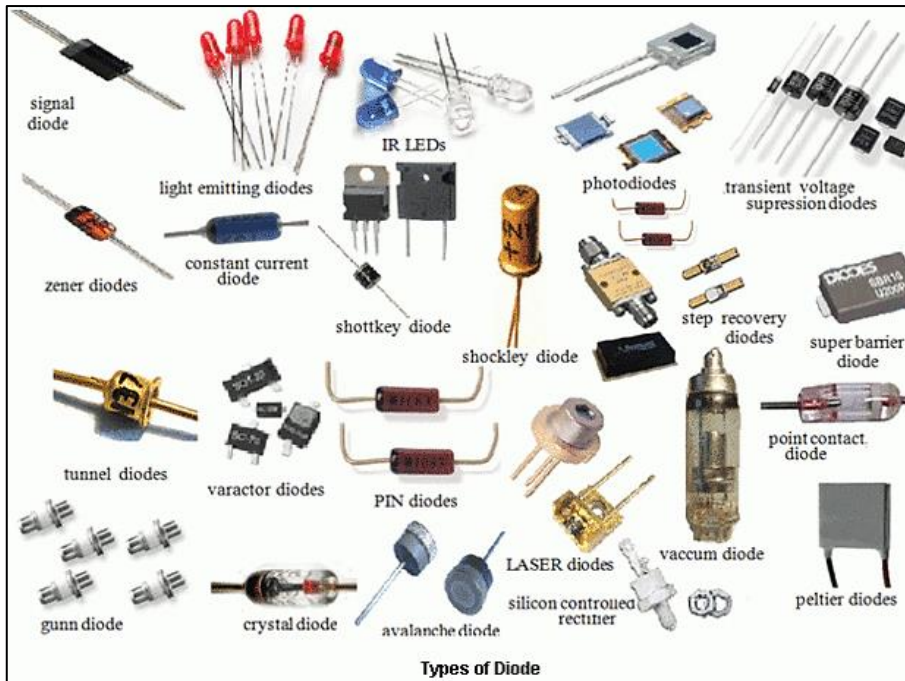


Figure 2.35. Diodes examples [52]

In Figure 2.36, the difference between LD, SLD and LED wavelengths is visualized. LDs have a fairly narrow bandwidth, while LEDs have a wider bandwidth. These light sources are used selectively for the purpose of application.

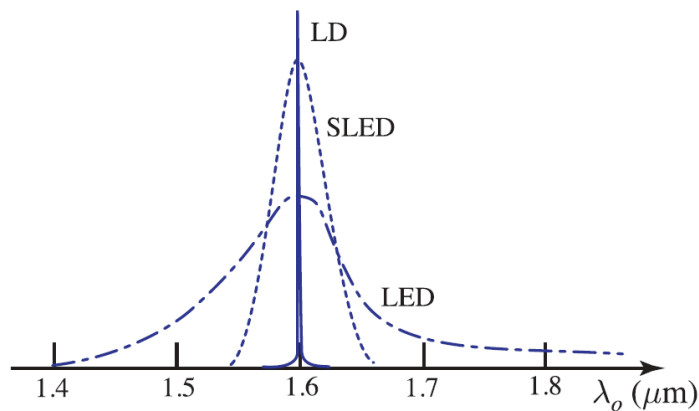


Figure 2.36. Laser diode, SLD and LED spectrum for InGasAsP/InP devices [7]

## 2.4.2 Laser Diode

A laser diode (LD) is an optoelectronic light source developed with semiconductor technology and working with diode principles. Spontaneous emission with a broad spectrum occurs by stimulated emission in a spatial single-mode optical oxidizing waveguide. With the simultaneous occurrence of these two emissions in the laser diode, a light beam that is neither as coherent as a laser nor as coherent as an LED is obtained.

Semiconductor diode lasers emit light like LEDs, but unlike LEDs, semiconductor lasers consist of a single coherent, strong and straight beam of light. Semiconductor lasers have a normal diode structure, that is, they have a P-N junction. By applying voltage, an electron in the p-n-transition is allowed to recombine with a hole. As the electron falls from a higher energy level to a lower one, radiation in the form of an emitted photon is produced. This is spontaneous emission. Stimulated emission, on the other hand, can be produced when the process is continued, and the light thus produced has the same phase, coherent level and wavelength.

Amplified Spontaneous Emission (ASE) architectures are obtained by the inclusion of different passive optical components in the configuration of the LDs, since SLDs and LEDs have a narrower spectrum compared to their bandwidth. The purpose of these architectures; is to determine the wavelength and optical power stability of the wave for application.

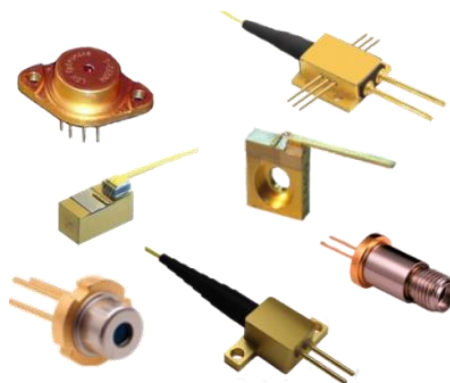


Figure 2.37. Laser diode [53]

### 2.4.3 Light Emitting Diode

LED is the abbreviation of Light Emitting Diode. LED is a semiconductor, diode-based, light-emitting electronic circuit element. LEDs can give high brightness light in various wavelengths such as visible light, ultraviolet and infrared. Low energy consumption, long life, durability, small size and fast switching on and off have advantages over traditional light sources such as bulbs or fluorescents.

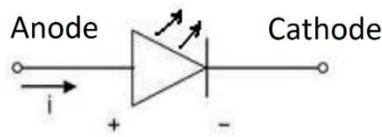


Figure 2.38. LED electronic symbol

Its main material is silicon. They emit light by releasing photons when current is flowing through them. They are produced to give light at different angles.

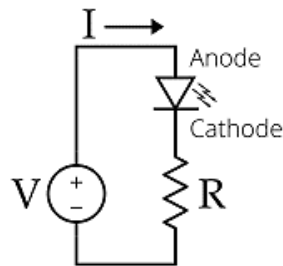


Figure 2.39. Basic LED circuit

In summary, when we examine it in terms of working principle; When the desired voltage is applied in the right direction, the energy released together with the movement of the electrons shown in red in Figure 2.40 to the spaces shown in white on the opposite side, is the transformation of the energy into a light source called photon with the effect of chemicals in the chip.

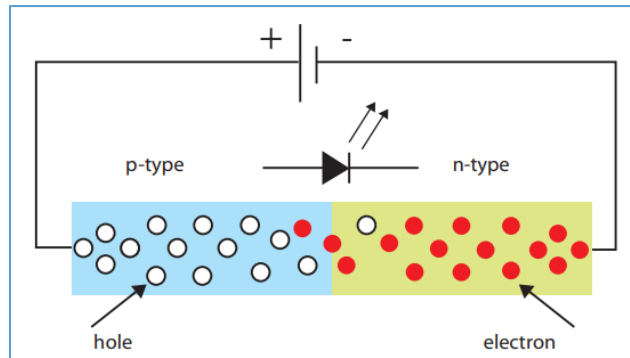


Figure 2.40. Light generation in PN-type semiconductor technology

The light emitted by LEDs is related to the semiconductor additives inside the LED chip. In which color the LED is desired to emit light, chemical materials such as gallium, arsenide, aluminum, phosphate, indium, and nitrite are added to the semiconductor material at the appropriate rate (GaAIAs, GaAs, GaAsP, GaP, InGaAlP, SiC, GaN). Thus, it is ensured that the LED chip radiates at the desired wavelength. Unlike other light sources, LEDs produce only one color.

In Figure 2.41, the visual of LEDs with different outer coatings for different applications is given. The plastic lens outside is usually the same color as the light it emits.

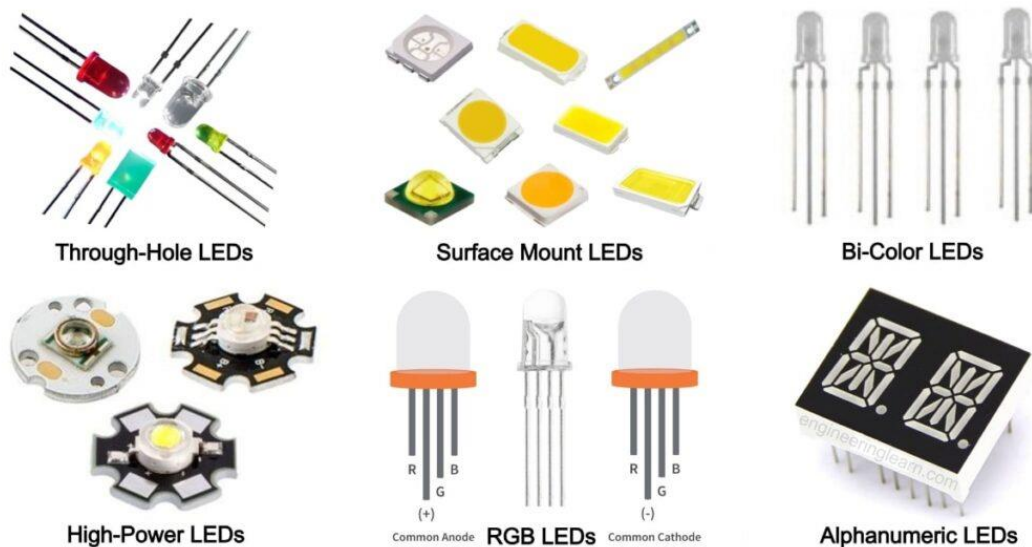


Figure 2.41. LEDs of different types and cladding [54]

The voltage-current graphs of the LEDs are exponential. A small voltage change on the led at the appropriate operating point causes a large current change. A series current limiting resistor is connected to the LEDs to prevent deterioration due to high current. This prevents deterioration of the non-sensitive LED voltage range.

The features and benefits of LEDs are as follows.

- Since the light is in the desired wavelength, they do not require filters or prisms to separate colors.
- All the light is used. In other lamps, some colors are filtered out.
- It saves energy.
- Very fast response (200ms)
- It is long-lasting. They can work for about 100,000 hours. (in a laboratory environment)
- Since they are small, they have many design features.
- It prevents the loss of energy as heat by producing low heat (110°C). This value goes up to 2700°C in incandescent lamps.
- Light intensity can be adjusted easily.
- It is resistant to impacts thanks to its plastic sheath.
- It does not contain heavy metals harmful to the environment, such as mercury found in other lamps.

#### **2.4.4 Superluminescent Laser Diode**

Superluminescent Diode (SLD - Super Bright Diode) are optoelectronic semiconductor devices with a wide wavelength range, also called super bright LED (SLED). Essentially, an SLD is a semiconductor optical amplifier with no input

signal, and weak spontaneous emission into waveguide mode followed by strong laser amplification.

SLD is an electrically driven p-n junction optical waveguide. Electric current will flow from the p-section to the n-section and through the active region sandwiched between the p- and n-section. During this process, light is produced through spontaneous and random recombination of positive (holes) and negative (electrons) electric carriers and then is amplified as it travels along a SLED's waveguide. The p-n junction of the semiconductor material of an SLD is designed in such a way that electrons and holes have a large number of possible states (energy bands) with different energies. Therefore, the combination of electrons and holes produces light with a wide optical frequency range.

Typical values for SLD modules on the market cover the range from 400 nm to 1700 nm for central wavelengths. In terms of bandwidth, it covers between 5 nm and 100 nm. In terms of typical wavelengths on the market, 840nm, 980nm, 1060nm, 1310nm, 1550nm, etc., with high output power and wide bandwidth selection. sizes are available.

There is a trade-off between maximum output power and bandwidth. Bandwidth is greater for devices with lower output power. Therefore, high-bandwidth SLDs appear to provide lower optical powers than laser diodes. Another factor important for some applications is wavelength stability, especially under varying temperatures and aging conditions. Typically, the center wavelength drifts by a fraction of a nanometer per Kelvin, following the shift of the semiconductor's gain spectrum.

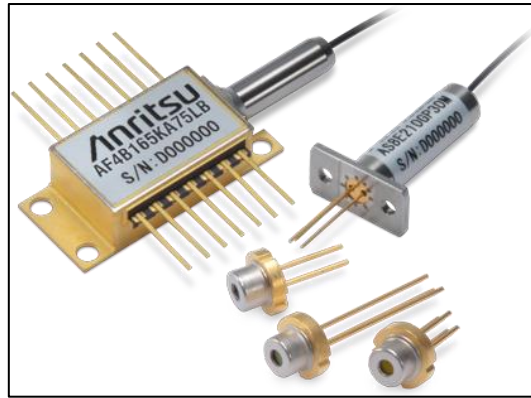


Figure 2.42. SLD examples [55]

An SLD combines the advantage of both LD and LED. This is because LD has diffraction-limited, spatially coherent, easy coupling to external components and the broadband spectrum of LED.

#### 2.4.5 Amplified Spontaneous Emission Source

Amplified Spontaneous Emission (ASE) light sources are optoelectronic components developed with semiconductor technology and working on the same principle. Spontaneous emission with a broad spectrum occurs by stimulated emission within a spatial single-mode optical oxidizing waveguide [3]. With the simultaneous occurrence of these two emissions, a light beam that is neither as coherent as a laser nor as coherent as an LED is obtained. Thus, a broad spectrum and low coherent light source with high optical power suitable for FOG products can be obtained.

Silica ( $\text{SiO}_2$ -Silicon dioxide) is used as fiber material in order to achieve low power losses.

In Figure 2.43, the y-axis shows a few dB power loss per km along the  $\alpha_R$  fiber path, while the x-axis shows different wavelengths. When the graph is examined; The loss is 2 dB/km at 850nm wavelength, 1 dB/km at 1060nm, 0.4 dB/km at 1300nm and 0.2 dB/km at 1550nm [5]. For applications with different performance requirements,

3 wavelengths often work in the FOG literature: 850nm, 1300nm and 1550nm. Nd-YAG lasers working with 1060nm are mostly used in the healthcare industry. Although wavelength around 1µm has more power loss compared to longer wavelength, it has higher quantum efficiency [5].

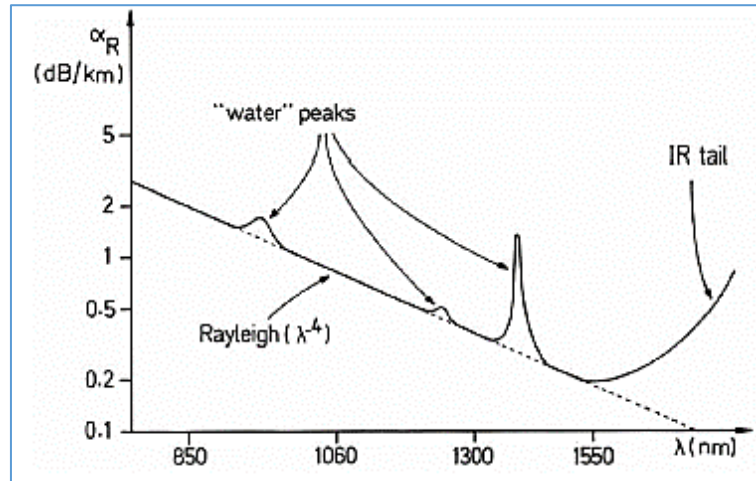


Figure 2.43. Graph of power loss in fiber versus wavelength [5]

At 1390nm, 1240nm and 950nm wavelengths, residual water absorption peaks, which is the effect of OH irregularities, cause high loss. After the 1700nm wavelength, the Infrared tail (infrared IR tail) rises rapidly and reaches 10 dB/km losses at 2000 nm.

The fiber material is not perfectly homogeneous; therefore, the beam may be subject to dispersion in rough areas. There are 3 types of dispersion: material dispersion, chromatic dispersion, and waveguide dispersion [7]. Chromatic scattering can be defined as the separation of the beam into different wavelengths due to Rayleigh scattering. In Figure 2.44, chromatic dispersion is ground zero for the wavelength of 1550nm.

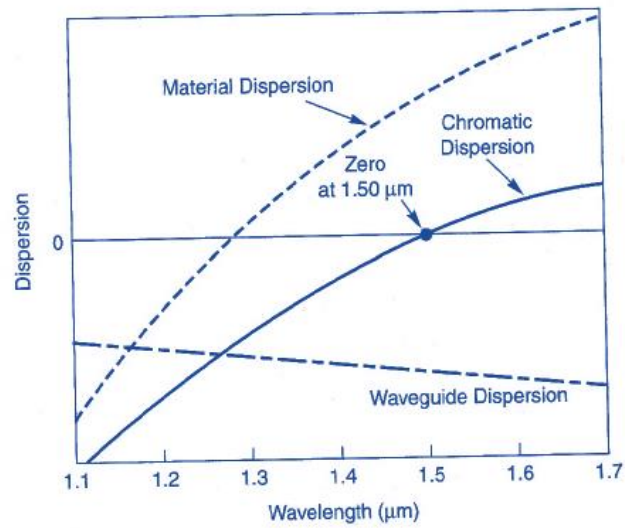


Figure 2.44. The scattering of the light in the fiber [5]

ASE light source sub-components are given in Figure 2.45. Different architectural designs can be developed in accordance with different performance values using the given sub-components of the ASE light source.

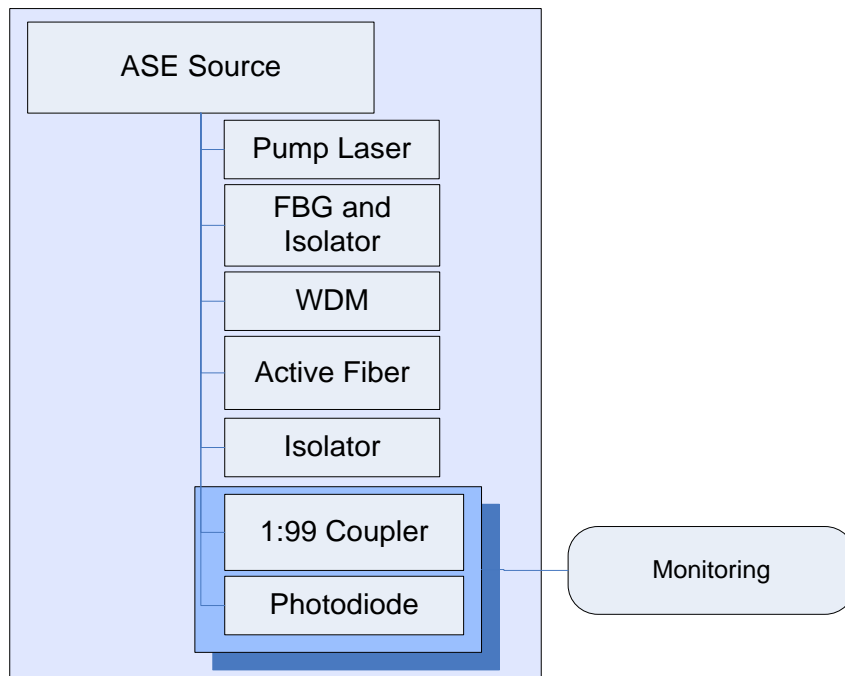


Figure 2.45. ASE source components

FBG is added to the output of pump lasers available in the market by the manufacturer. Thus, wavelength stability is tried to be ensured. A laser diode similar to the example given in Figure 2.46 operating at 980nm is expected to produce a spectrum as in Figure 2.47.

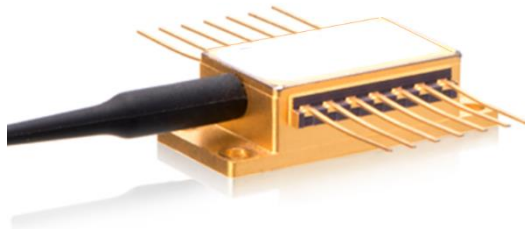


Figure 2.46. Pump laser [56]

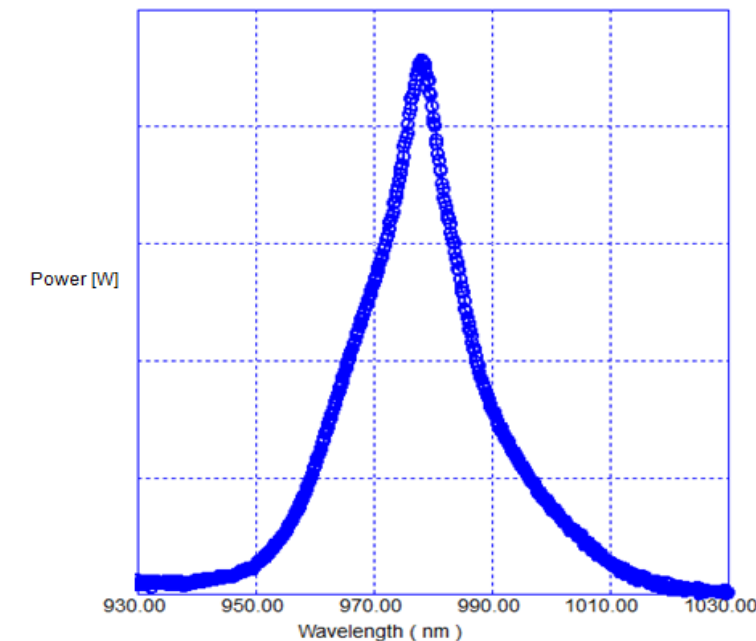


Figure 2.47. Pump laser spectrum

After the beam fed by the pump laser at a wavelength of 980 nm enters the Er+3 doped fiber, it is oxidized by spontaneously emitted photons between 1520nm and 1570nm and has a spectrum as in Figure 2.48. This spectrum wave propagates from both ends of the Er-doped fiber and has a broad FWHM to use in the IFOG optical

path. However, this broad spectrum has poor central wavelength stability over broad temperature range. Therefore, many techniques needed to lower this effect [35].

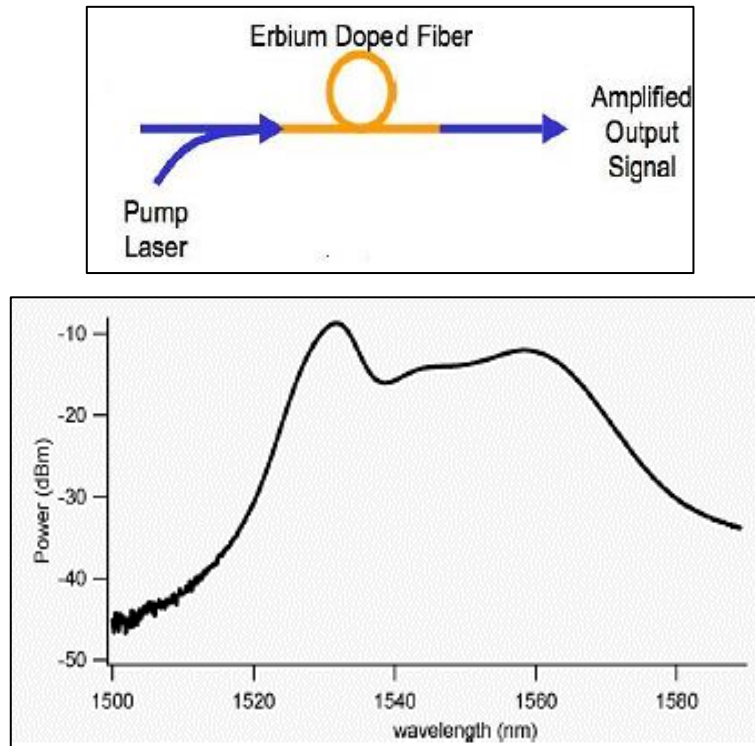


Figure 2.48. ASE output spectrum for 1550nm ASE source [35]

Depending on the application, optical filters such as CFBG can be used to operate in the desired wavelength range. Thus, the optical path continues with an oxidized output with a specific center wavelength and FWHM. Ytterbium-doped ASE sources are detailed in the next sections.

## 2.5 Optoelectronic

### 2.5.1 Phase Modulator

The piezoelectric phase modulator changes the refractive index and creates a phase difference by stretching the fiber material wrapped around the piezoelectric tube, which can be expanded and contracted by applying voltage.

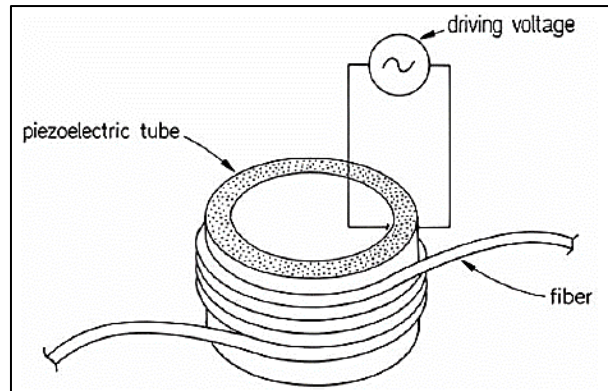


Figure 2.49. Piezoelectric phase modulator [5]

Today, the piezoelectric phase modulator is no longer used in fiber optic gyroscope applications. The reason is that it loses efficiency at certain mechanical resonances. The biggest disadvantage is that although it is efficient in open-loop configurations, it cannot perform wide-range feedback modulations such as the phase ramp used for closed-loop.

Instead of the piezoelectric phase modulator, MIOC (Multifunctional Integrated Optical Chip) product has started to be used as a phase modulator with improved production technology. The beam is transmitted to the MIOC through the fiber material. LiNbO<sub>3</sub> material produced with the Photon Exchange (PE) technique is used as an optical waveguide at the MIOC entrance. MIOC includes a linear polarizer, Y splitter/combiner and electrodes. The beam, coming to the entrance of MIOC with PM fiber, firstly moves through LiNbO<sub>3</sub> material by changing the waveguide, passes through the polarizer, splits into two with equal powers (50:50) and continues to enter the coil in two PM fibers joined to the output of MIOC by traveling between the electrodes.

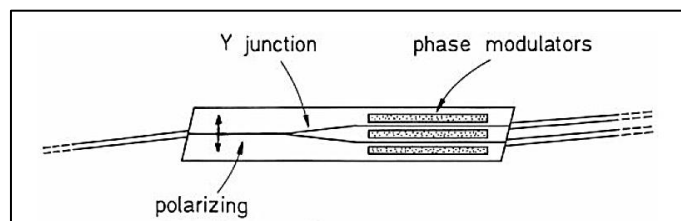


Figure 2.50. MIOC [5]

The cross-coupling or cross-talk in MIOC occurs at the junction of the PM fiber with the MIOC waveguide. During MIOC production, this parameter is measured and given in the description of the product features.

In order to reduce the cross-talk effects of the beam entering the MIOC, an extra PM fiber is added in front of it to control the polarization. PM fiber length to be added can be determined by controlled tests. By gradually shortening a long PM fiber, the appropriate length of fiber can be determined, minimizing the cross-talk error and saving space at the same time.

Polarization control in PM fibers is not perfect. Along the fiber, residual coupling occurs in crossed-polarization modes. This increases the polarization ratio in the vertical and horizontal axes of the fiber. PER occurs throughout the MIOC and fiber coil. For high-performance FOG, the PER measured from MIOC should be more than 60dB [57]. Therefore, whenever the PER of a gyroscope is to be measured, the test set-up must have MIOC and coil.

## **2.5.2 Photodetectors**

With the development of semiconductor technology, diodes, and photodiodes/detectors, which can convert optical signals to electrical signals, have also started to develop. There are different photodiodes according to their working principles and material type. Some of those are; the PN photodiode, PIN (p-type, intrinsic and n-type) photodiode, phototransistor, photoresistor, photoconductor and avalanche photodiode (APD). Among these; the PIN photodiode is used for fiber optic gyroscopes because it is easy to manufacture, has high reliability, low noise and has a high band gap compared to other photodiodes.

A photodiode is a diode that conducts light energy. It is a p-n junction device that always operates at reverse voltage. Although there are different types of photodiodes on the market, they all work on the same basic principles. These can be classified as

PN photodiode, metal-semiconductor photodiode, Schottky photodiode, PIN photodiode and avalanche photodiode.



Figure 2.51. Photodiode electronic symbol

Photodiodes are one of the important optoelectronic devices widely used in optical fiber communication systems. Of these, PIN photodiodes are preferred especially in fiber optic gyroscope technology, both for their high quantum efficiency and for the wavelength studied. There are three zones in the PIN diode. There are p-region, inner region and n-region. The p-region and n-region are relatively heavily doped from the p-region and n-region of common p-n diodes.

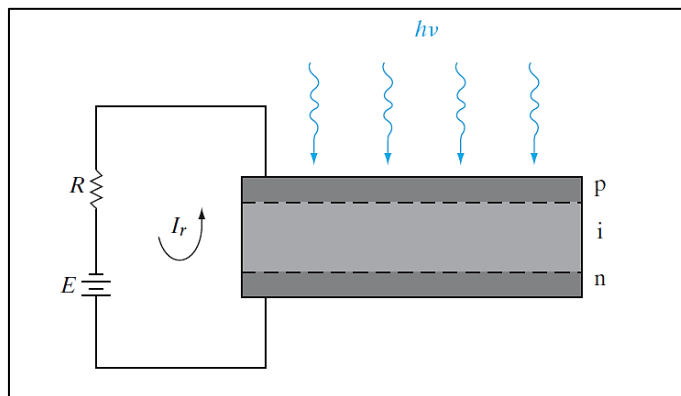


Figure 2.52. P-N type photodiode working principle [58]

When a typical diode is reverse biased, the reverse current flowing is leakage current and its value is very small. This current is caused by minority current carriers and its value will be very small if it is not interfered with from outside. The way to increase this current is possible by giving an external energy, breaking the valence bonds and thus increasing the number of minority current carriers. This energy can be heat energy or light energy. For this purpose, the light energy collected by a lens can be focused on the full junction surface, and the valence bonds can be broken, and the

number of minority current carriers and, accordingly, the reverse current can be increased. Such diodes are called photodiodes. These diodes are used as converters that convert light intensity and wavelength into the variable current in light intensity measurement and light control circuits by being reverse polarized in electronic circuits.

The minority carrier population in the PIN photodiode is very large compared to the PN junction photodiode. Therefore, the PIN photodiode carries a greater minority carrier current than the PN junction photodiode. When a forward voltage is applied to the PIN photodiode, it behaves like a resistor. Like capacitance, in the PIN photodiode, the p region and n region act as electrodes and the inner region acts as a dielectric. The separation distance between the p region and the n region in the PIN photodiode is very large due to the large depletion width. Therefore, the PIN photodiode has low capacitance compared to the PN junction photodiode.

The advantages of PIN photodiode are as follows:

- Wide bandwidth
- High quantum efficiency
- High response speed

The characteristic behavior of a photodiode against applied voltage and current is shown in Figure 2.53.

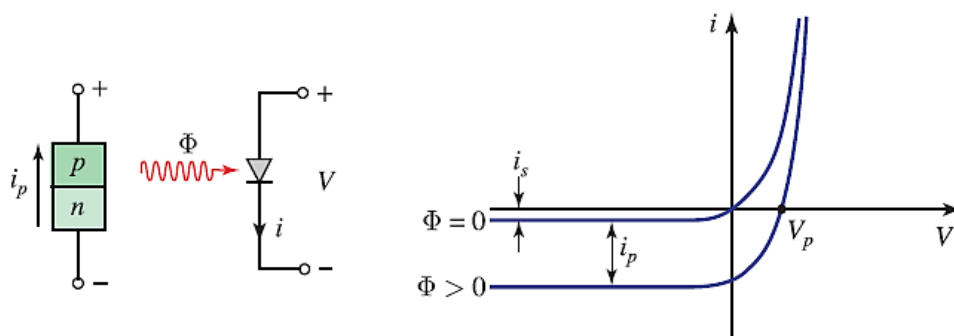


Figure 2.53. Photodiode characteristic [7]

The parameters of the photodetectors are as follows.

- Quantum Efficiency ( $\eta$ )

The probability that a photon generates an electron that will contribute to the detector current.

- Detector Response / Responsivity

It is the coefficient between the current formed in the detector circuit and the optical power (P) falling on the detector.

$$R = \frac{i_p}{P} = \frac{\eta e}{h\nu} = \eta \frac{\lambda}{1.24} \quad (2.14)$$

$R$ : Detector responsivity

$i_p$ : Detector current

$P$ : Optical power at the detector

$\eta$ : Quantum efficiency

$e$ : Electron charge

$h$ : Planck constant

$\nu$ : Photon frequency

$\lambda$ : Wavelength

- Response Time

In detectors, the response time depends on the transition time delay and the RC time constant. The transition time delay is related to the motion of the electron-hole pair formed by the detector to detect the light falling on the semiconductor region. If the RC time constant is considered as the sum of the PIN region of the semiconductor, R (resistance), and C (capacitance), it is the current time created by this region.

- Gain

It is the total amount of charge that a photon creates in the detector circuit. If 1 photon creates a charge Q instead of 1 free charge:

$$Q = G \cdot e \quad (2.15)$$

Gain:

$$G = \frac{Q}{e} \quad (2.16)$$

Detector responsivity

$$R = G \frac{i_p}{P} \quad (2.17)$$

- Gain-Bandwidth Product
- Signal-to-Noise Ratio (SNR)

The most common materials in the semiconductor industry are Si, Ge, GaAs, GaP, and InGaAs. Since these materials have different energy ranges, they have their own characteristics and different responses when detecting light falling on them. Specific sensitivity to the working wavelengths of the PIN photodiode manufactured in different materials is given in Figure 2.54.

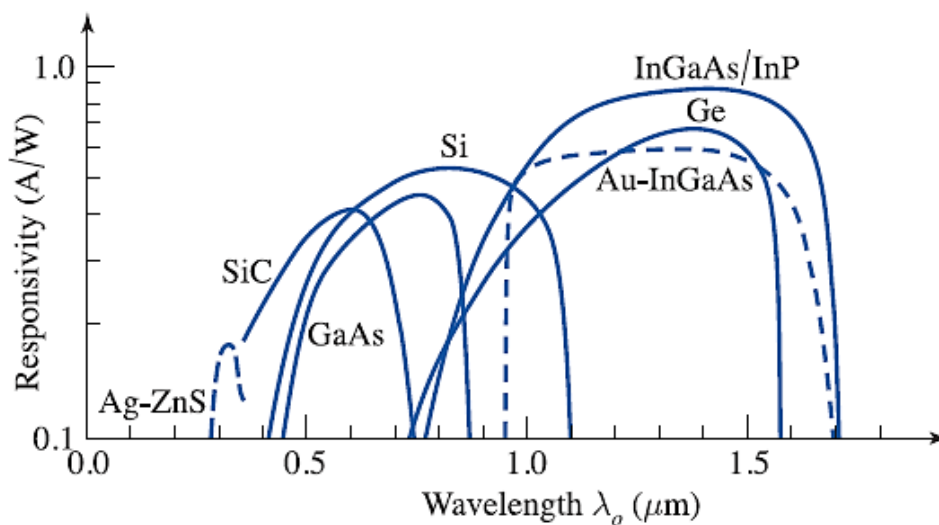


Figure 2.54. Comparison of detector material types [7]

Responsivity is an important parameter for photodetectors. It characterizes the relationship between the input and output power of the photodiode. It is expressed by  $\rho$  or  $R$  [A/W]. It is proportional to the power of the light falling on it and the photocurrent generated.

$$R(A/W) = \frac{I_p}{P} \quad (2.18)$$

The parameter that shows how efficiently a photodiode converts a light signal to an electrical signal is sensitivity. Typically, it should be between 0.5 A/W and 1.0 A/W. R can be determined by the manufacturer. Photocurrent can be calculated by including the sensitivity value and input power given by the user. When high light power is applied in photodiodes, saturation is expected after a certain level and in this saturation situation, the above equation) cannot be used. Therefore, it should be studied in unsaturated conditions.

The sensitivity parameter is also related to the wavelength studied. Theoretically; The quantum efficiency  $\eta$ , the speed of light  $c$ , the plank constant  $h$ , and the wavelength  $\lambda$  and the sensitivity R is calculated. 1248 eV.nm is evaluated for  $hc$ .

$$R(A/W) = \frac{\eta}{1248} \cdot \lambda \quad (2.19)$$

According to the above equation, quantum efficiency and high wavelength are preferred in terms of increasing sensitivity and taking good measurements. When examined; It is preferred to work with the InGaAs material, whose efficiency is closest to one hundred percent, at a wavelength of 1550nm. Assuming the efficiency of the InGaAs material at 70 percent, its sensitivity is 0.869 A/W when operating at 1550nm. This value is a good value to be reached. In practice, less theoretical computation is expected.

Dark current sensitivity in photodiodes refers to the minimum light power that the photodiode can measure. If the photocurrent that will generate the light power stays below the dark current, the measured value will not reach the expected value. In modern photodiodes, typically at room temperature the dark current sensitivity is about 5nW. As the temperature rises, the dark current also increases.

In Table 2.2, typical parameters of a PIN photodiode and APD, which are widely used in the market with the highest efficiency for three different materials. When the operating wavelength, dark current, quantum efficiency and sensitivity parameters

are evaluated; the PIN photodiode, produced with an optimum level of InGaAs material, is preferred in fiber optic gyroscope applications.

Table 2.2. Comparison of materials used in photodetectors [59]

| Photodetector Type | Gain                             | Spectral Range (nm) | Quantum Efficiency (%) | Response Time (ns) | Dark Current (nA) |
|--------------------|----------------------------------|---------------------|------------------------|--------------------|-------------------|
| Si PIN             | 1                                | 400-1150            | 60-90                  | 0.3-3              | -                 |
| Si APD             | 50-300                           | 400-1150            | 70-80                  | 0.5-5              | 0.1-1.0           |
| Ge APD             | 10-100                           | 800-1750            | 50-80                  | 0.3-3              | 5-100             |
| InGaAs PIN         | 1                                | 900-1700            | 70-90                  | 0.05-1             | -                 |
| InGaAs APD         | 10-40                            | 900-1700            | 60-90                  | 0.1-1              | 0.5-5             |
| Photomultiplier    | 10 <sup>5</sup> -10 <sup>7</sup> | 160-850             | 30                     | 0.15-13            | 10-200            |

PINFET (p-type-intrinsic-n type field effect transistor) is developed by combining a trans-impedance circuit to the PIN diode and current amplifier. An example of a PINFET suitable for use in commercially available FOG is shown in Figure 2.55.

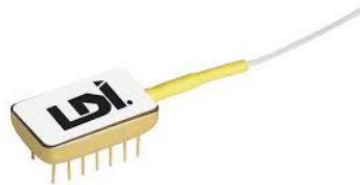


Figure 2.55. PINFET example [60]

PINFET has a PIN photodiode and FET op-amp circuit in its structure. Its output is the voltage as shown in Figure 2.56.

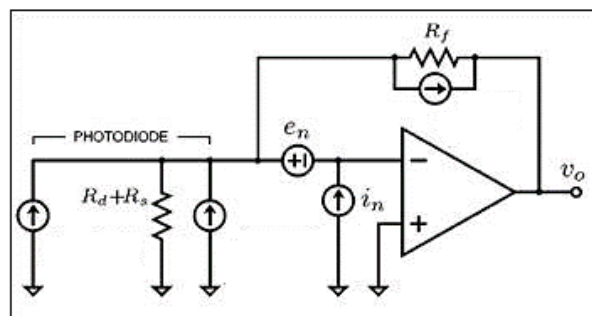


Figure 2.56. Basic FET circuit

## 2.6 ASE Source for 1030nm IFOG

Ytterbium (Yb) is a rare earth element and used its ions used as dopants in the active medium of fiber lasers and solid-state lasers. Generally, ytterbium gain medium is pumped at 900-1000nm wavelength range and the such system operates at 1.03–1.12 $\mu\text{m}$  wavelength range [61].

### 2.6.1 Ytterbium Gain Medium

The interest in Ytterbium-doped fiber lasers has been increasing rapidly since its first development in late 80s [62]. Having broad emission bandwidth and high excited state absorption makes Ytterbium-doped fiber attractive compared to other rare-earth element fibers. Emission bandwidth spans between 975 and 1200 nm wavelength range and the simple energy level structure of Ytterbium enables to use of such systems in various diode pumping applications [63], [64].

The shell of ytterbium ions has one lack of an electron. Energy levels of Yb ions that correspond light emission are  $^2F_{7/2}$  and  $^2F_{5/2}$  which are ground level and excited level, respectively [61].

The stark effect which is energy level splitting under the exterior electric field results in the splitting of the pump and laser's energy levels into sub-energy levels. These energy levels are shown in Figure 2.57.

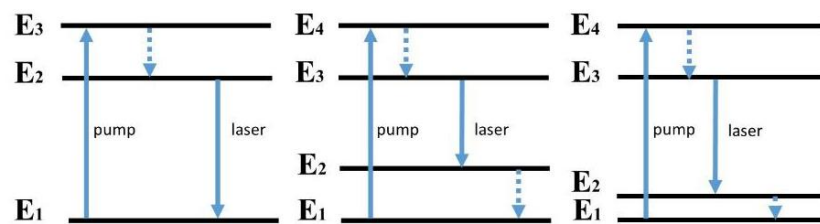


Figure 2.57. a) Three-level b) four-level c) quasi-three-level systems

In Figure 2.57, horizontal lines correspond to energy levels. The higher lines have higher energy. For three-level systems, the transition of the laser ends at a ground

energy level. On the other hand, the transitions of the laser end at an energy level higher energy compared to ground level for four-level systems. In the case of quasi-three-level systems, population occurs at the lower laser energy state in thermal equilibrium.

Compared to other rare earth elements, ytterbium active medium has only one excited level which increases conversion efficiency greatly. Quantum defect which is a parameter related to energy band difference between ground and excited states is very low for Yb-doped gain mediums. Stokes shift means that lasing photons have lower energy compared to pumping photons. In other words, the emission wavelength is longer than the pump wavelength. This efficiency is determined by quantum defect and can be calculated as [61]:

$$q = h\nu_p - h\nu_l = h\nu_p \left( 1 - \frac{h\nu_l}{h\nu_p} \right) \quad (2.20)$$

Here,  $\nu_p$  and  $\nu_l$  are pump and lasing frequency, respectively and  $h$  is the Planck constant. A small difference between the frequency of the pump and lasing emission results in small quantum defects, high power conversion efficiency and low heat dissipation for a Yb-doped active medium. Quasi-three-level behavior is observed for a system having a small quantum defect. During laser transition, the emitted light is strongly absorbed in the unpumped region of an active medium that creates an intermediate level close to ground level in quasi-three-level. This increases the pump power threshold [61]. The intermediate level has mainly populated by ions that have a temperature of their environment. Therefore, unpumped active region reabsorbs emitted wavelengths. For an amplifier system, the pump and signal wavelength determine which energy level behavior is presented. 1030nm region dominates three-level behavior whereas longer wavelengths than 1080nm present four-level behavior where the reabsorption level is lower. In this condition, the energy gap between excited and ground level increases resulting in lower laser threshold levels [61].

Yb-doped active fibers are used in various applications including fiber laser and amplification systems. The range of 800 to 1064 nm can be used as pump wavelength to achieve 975 to 1200 nm of output wavelength. High absorption and emission cross-sections can be achieved due to simple electronic structure and high doping concentration options [61]. In Figure 2.58, absorption and emission cross-sections are displayed.

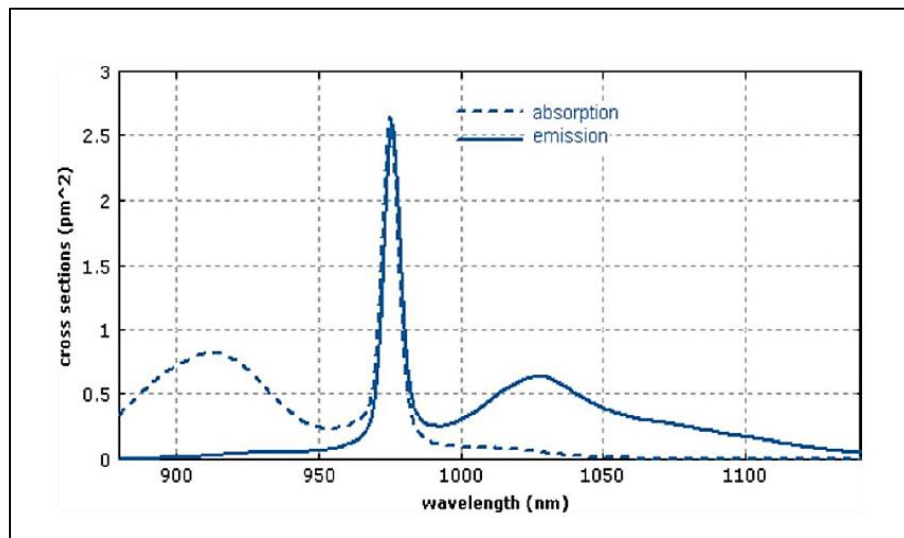


Figure 2.58. Absorption and emission cross-sections of Yb-doped fibers [63]

Two pump wavelength regions are optional according to Figure 2.58. 910nm region has a broad absorption cross-section although higher pump powers are needed to achieve a higher gain level. This will result in ASE which limits the maximum achievable gain. On the other hand, the 975nm wavelength region has higher efficiency in both pumping and absorption cross-section which mitigates ASE. Quasi-three-level behavior for the 975nm region has high re-absorption loss where total gain fiber length should be optimized carefully. For ASE structure, fiber length optimization results are explained in the next sections.

## 2.6.2 Gain Dynamics

In the case of having extremely rapid nonradiative relaxations to the meta-stable state, reduced two-level systems can be used as an alternative to three-level systems [65]. Ytterbium gain medium can be modeled as a simple two-level laser scheme when the medium is pumped at a 975 nm pump wavelength.

In Equations (2.21) and (2.22), the rate equations of Ytterbium ions in the excited energy state and ground energy state are given.

$$\frac{dn_2}{dt} = (R_{12} + W_{12})n_1 - (R_{21} - W_{21} + A_{21})n_2 \quad (2.21)$$

$$\frac{dn_1}{dt} = -(R_{12} + W_{12})n_1 + (R_{21} - W_{21} + A_{21})n_2 \quad (2.22)$$

Here  $n_2$  are normalized populations of excited energy state and  $n_1$  is normalized populations of lower energy states.  $R_{12}$  and  $R_{21}$  are rates of pump excitation and relaxation, respectively.  $W_{12}$  and  $W_{21}$  rates of signal absorption and emission, respectively.  $A_{21}$  is the rate of spontaneous emission.

The total number of the excited and ground state is normalized and the conservation of energy law states this number equals 1.

$$n_1 = 1 - n_2 \quad (2.23)$$

The normalized population equations are given in Equations (2.24) and (2.25) when the system is in a steady state (i.e.,  $\frac{dn_i}{dt} = 0$ ).

$$n_1 = \frac{R_{21} + W_{21} + A_{21}}{R_{12} + R_{21} + W_{12} + W_{21} + A_{21}} \quad (2.24)$$

$$n_2 = \frac{R_{12} + W_{12}}{R_{12} + R_{21} + W_{12} + W_{21} + A_{21}} \quad (2.25)$$

In an optical fiber, the absorption and emission cross-sections of the ions which are found in the gain medium determine the pump and signal transition rates. These transition rates are given in Equations (2.26), (2.27), (2.28) and (2.29).

$$R_{12} = \frac{\sigma_{ap} I_p}{h\nu_p} \quad (2.26)$$

$$R_{21} = \frac{\sigma_{ep} I_p}{h\nu_p} \quad (2.27)$$

$$W_{12} = \frac{\sigma_{as} I_s}{h\nu_s} \quad (2.28)$$

$$W_{21} = \frac{\sigma_{es} I_s}{h\nu_s} \quad (2.29)$$

Here  $\sigma_{ap}$  and  $\sigma_{ep}$  are effective pump absorption and emission cross-sections, respectively.  $\sigma_{as}$  and  $\sigma_{es}$  are effective signal absorption and emission cross-sections, respectively.  $I_p$  and  $I_s$  are the intensities of the pump and signal field.  $\nu_p$  and  $\nu_s$  are frequencies of corresponding transitions. The rate of spontaneous emission is given in Equation (2.30).

$$A_{21} = \frac{1}{\tau} \quad (2.30)$$

Here,  $\tau$  is the lifetime of the Ytterbium ions in the excited state. Given formulas are used for quasi-two-level fiber systems. The propagation equations as given in Equations (2.31) and (2.32) are used in order to calculate the pump and signal power through the gain fiber.

$$\frac{dP_p}{dz} = \Gamma_p N_{tot} (\sigma_{ep} n_2 - \sigma_{ap} n_1) P_p(z) \quad (2.31)$$

$$\frac{dP_s}{dz} = \Gamma_s N_{tot} (\sigma_{es} n_2 - \sigma_{as} n_1) P_s(z) \quad (2.32)$$

Here,  $\Gamma_p$  is the overlap factor of the pump which can be explained as the pump signal area over the Yb-doped area ratio which is  $\frac{A_p}{A_d}$  and  $A_p$  is the pump light-field mode. Total ion density is shown by  $N_{tot}$ .  $\Gamma_s$  is the overlap factor of the signal which can

be explained as the pump signal area over the Yb-doped area ratio which is  $\frac{A_s}{A_d}$  and  $A_s$  is the signal light-field mode.

A new Ytterbium gain model is proposed by considering the ASE power in both forward and backward directions in addition to simple spontaneous emission  $A_{21}$ .

$$n_2 = \frac{R_{12} + W_{12} + AS_{12}}{R_{12} + R_{21} + W_{12} + W_{21} + A_{21} + AS_{12} + AS_{21}} \quad (2.33)$$

Transition rates for ASE are given as:

$$AS_{12} = \frac{\sigma_{aas} I_{AS}}{h\nu_{AS}} \quad (2.34)$$

$$AS_{21} = \frac{\sigma_{eas} I_{AS}}{h\nu_{AS}} \quad (2.35)$$

The sum of forward and backward traveling waves gives the total ASE intensity.

$$I_{AS} = I_{AS}^F + I_{AS}^B \quad (2.36)$$

Furthermore, the model can be extended with the inherent fiber loss. The final rates are given as:

$$n_2 = \frac{\frac{\sigma_{ap} I_p}{h\nu_p} + \frac{\sigma_{as} I_s}{h\nu_s} + \frac{\sigma_{aas} I_{AS}}{h\nu_{AS}}}{\frac{(\sigma_{ap} + \sigma_{ep}) I_p}{h\nu_p} + \frac{(\sigma_{as} + \sigma_{es}) I_s}{h\nu_s} + \frac{1}{\tau} + \frac{(\sigma_{aas} + \sigma_{eas}) I_{as}}{h\nu_{as}}} \quad (2.37)$$

$$\frac{dP_p}{dz} = \Gamma_p N_{tot} (\sigma_{ep} n_2 - \sigma_{ap} n_1) P_p(z) - \alpha_p P_p(z) \quad (2.38)$$

$$\frac{dP_s}{dz} = \Gamma_s N_{tot} (\sigma_{es} n_2 - \sigma_{as} n_1) P_s(z) - \alpha_s P_s(z) \quad (2.39)$$

$$\frac{dP_{as}^F}{dz} = \Gamma_{as}N_{tot}(\sigma_{eas}n_2 - \sigma_{aas}n_1)P_{as}^F(z) + \Gamma_{as}N_{tot}\sigma_{eas}h\nu_{as}\Delta\nu_{as} - \alpha_{as}P_{as}^F(z) \quad (2.40)$$

$$\frac{dP_{as}^B}{dz} = -\Gamma_{as}N_{tot}(\sigma_{eas}n_2 - \sigma_{aas}n_1)P_{as}^B(z) - \Gamma_{as}N_{tot}\sigma_{eas}h\nu_{as}\Delta\nu_{as} + \alpha_{as}P_{as}^B(z) \quad (2.41)$$

The second term in Equations (2.40) and (2.41) represents the contribution of the spontaneous emission into the mode [66].

These equations require two boundary conditions at  $z = 0$  and  $z = L$  with  $L$  being the length of the gain fiber. The bidirectional split-step method can be used to calculate the pump, signal and forward and backward ASE powers using these equations.

Equations (2.40) and (2.41) can be used to model SPF (single pass forward) and SPB (single pass backward) ASE sources. In order to model DPF (double pass forward) and DPB (double pass backward) ASE sources, results of single pass configuration are used. SPB acts as a forward signal after reflection and results in DPF configuration. Similarly, SPF acts as a forward signal after reflection and results in DPB configuration. These statements are displayed in Figure 2.59 and Figure 2.60.

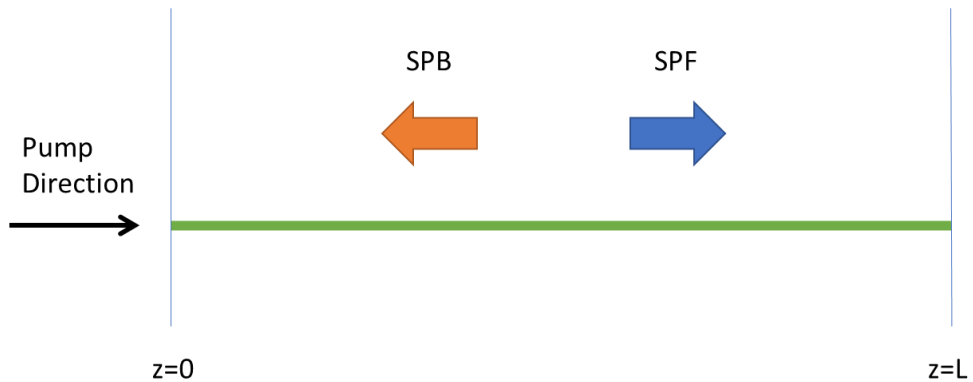


Figure 2.59. SPB and SPF representations

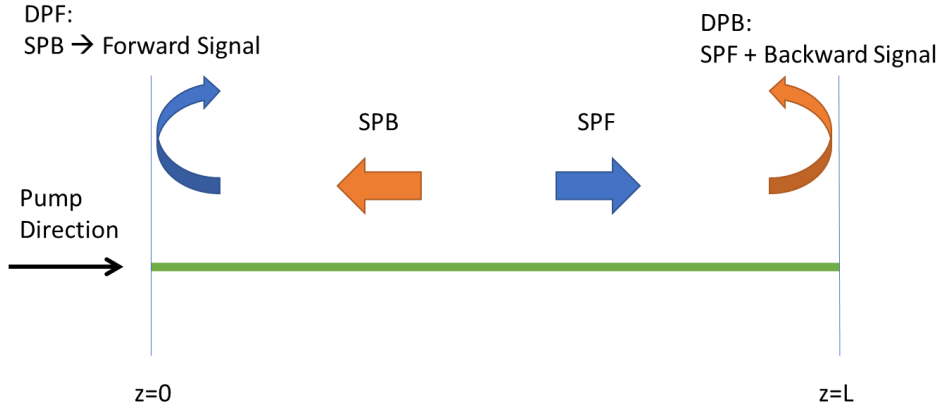


Figure 2.60. DPB and DPF representations

## 2.7 ASE Source Optimization

Generally, ASE can be classified into four groups single-pass forward (SPF), double-pass forward (DPF), single-pass backward (SPB), and double-pass backward (DPB). The preferred configuration determines the output characteristics of a Yb-doped ASE in terms of the central wavelength, spectral bandwidth, optical power, and wavelength and power stability.

Especially for fiber optic gyroscopes, mean wavelength stability is crucial for the scale factor which is the relation between the input and output of the sensor [25]. The mean wavelength of a spectrum is given as [67].

$$\bar{\lambda} = \frac{\int P(\lambda) \lambda d\lambda}{\int P(\lambda) d\lambda} \quad (2.42)$$

For an ASE source, there are certain parameters affect mean wavelength stability such as gain fiber temperature ( $T$ ), pump power ( $P_p$ ), pump wavelength ( $\lambda_p$ ), pump state polarization ( $SOP_p$ ), and feedback power ( $F$ ) reflected from the output [67].

$$\Delta\bar{\lambda} = \frac{\partial\bar{\lambda}}{\partial T} \Delta T + \frac{\partial\bar{\lambda}}{\partial P_p} \Delta P_p + \frac{\partial\bar{\lambda}}{\partial \lambda_p} \Delta \lambda_p + \frac{\partial\bar{\lambda}}{\partial SOP_p} \Delta SOP_p + \frac{\partial\bar{\lambda}}{\partial F} \Delta F \quad (2.43)$$

### 2.7.1 ASE Configurations

Four basic ASE source configurations are proposed including SPF, SPB, DPF and DPB. Each design commonly consists of a pump laser diode (LD), a wavelength division multiplexer (WDM) to combine pump and emission wavelength, Yb-doped fiber and an in-line isolator to block back reflections resulting from fiber outputs.

#### 2.7.1.1 Single Pass Configurations

For SP configuration, Yb-doped fiber is pumped in a forward direction. Output is observed either through the active fiber or the second input of WDM. APC is used to block back reflection. Designs are shown in Figure 2.61.

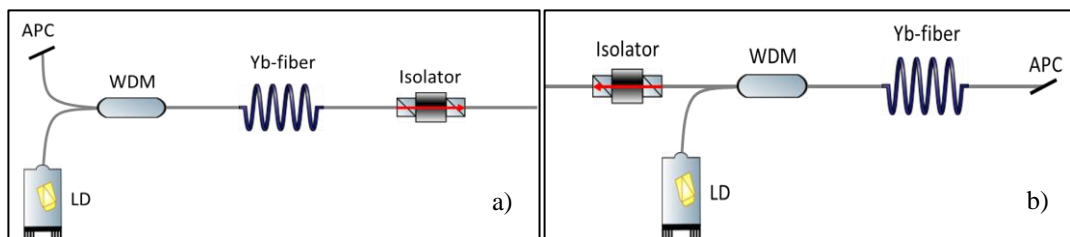


Figure 2.61. SP ASE architectures a) SPF b) SPB

#### 2.7.1.2 Double Pass Configurations

For DP configuration, Yb-doped fiber is pumped in a forward direction. Instead of APC, an in-line mirror is used to reflect some portion of the backward ASE through Yb-doped fiber for one-stage amplification. Designs are shown in Figure 2.62.

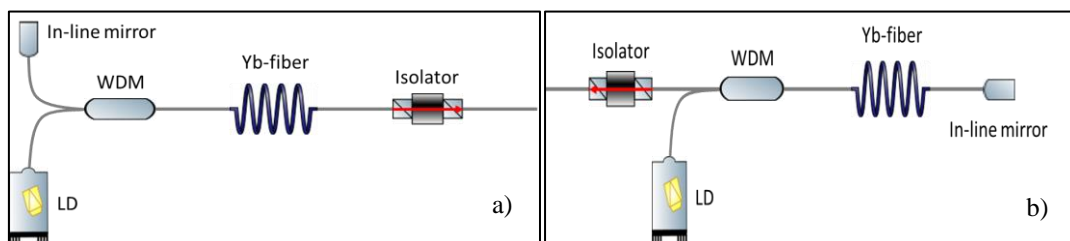


Figure 2.62. DP ASE architecture a) DPF b) DPB

## 2.7.2 Test Results

Output spectrum and power tests are conducted at room temperature. Temperature dependency of mean wavelength is tested using a thermal chamber. An optical spectrum analyzer (OSA) is used and data is collected via a computer. The temperature test setup is shown in Figure 2.63.

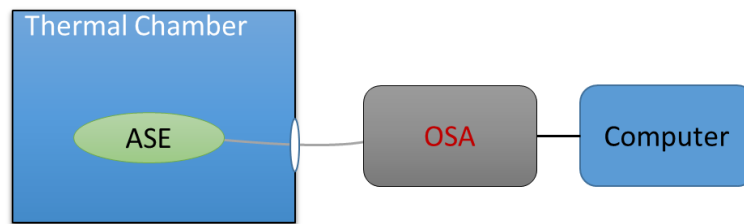


Figure 2.63. Temperature test setup

### 2.7.2.1 Single Pass Forward

Spectrum outputs of SPF configuration for different Yb-doped fiber lengths are given in Figure 2.64 for different pump currents.

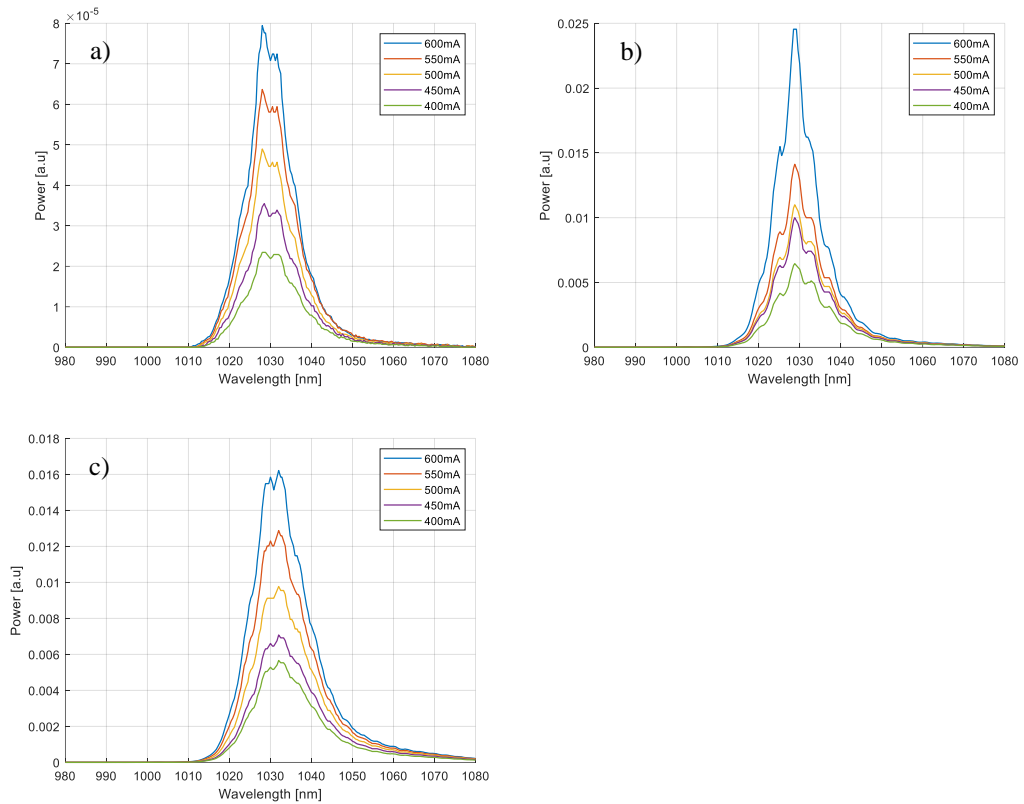


Figure 2.64. SPF configuration output spectrum for different pump currents a) 0.6m b) 0.8m and c) 1.0m

The result states that spectral characteristics change with the Yb-doped fiber length. Output power and mean wavelength analysis of ASE configuration are given in Figure 2.65.

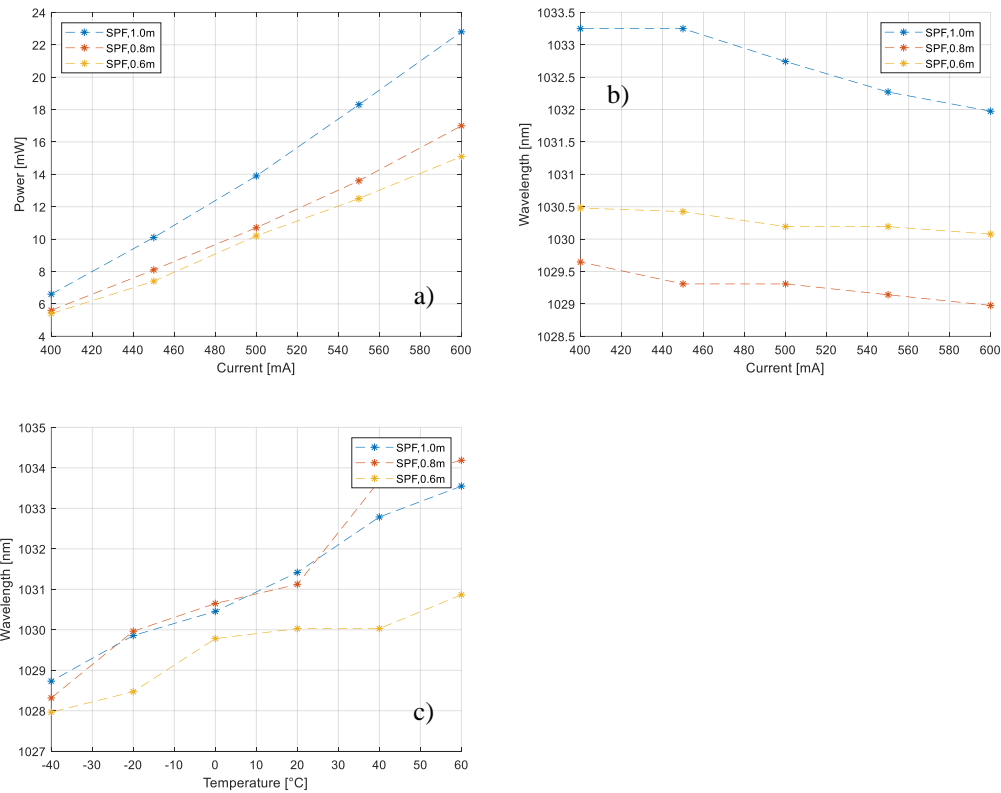


Figure 2.65. SPF a) output power and b) mean wavelength for different Yb-doped fiber lengths. c) Mean wavelength for different temperatures

Generally, the mean wavelength of the spectrum shifts towards shorter wavelengths as the output power increases. On the other hand, the mean wavelength of the spectrum shifts towards longer wavelengths with the increase in ambient temperature.

### 2.7.2.2 Single Pass Backward

Spectrum outputs of SPF configuration for different Yb-doped fiber lengths are given in Figure 2.66 for different pump currents.

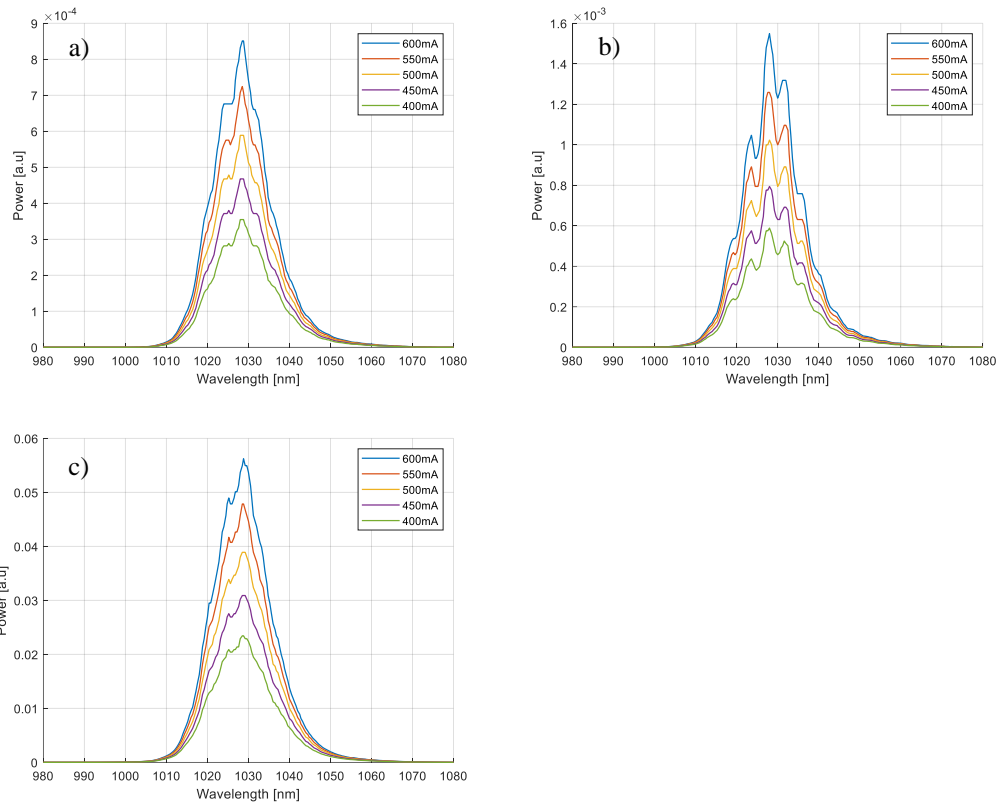


Figure 2.66. SPB configuration output spectrum for different pump currents a) 0.6m b) 0.8m and c) 1.0m

Output power and mean wavelength analysis of SPF configuration are given in Figure 2.67.

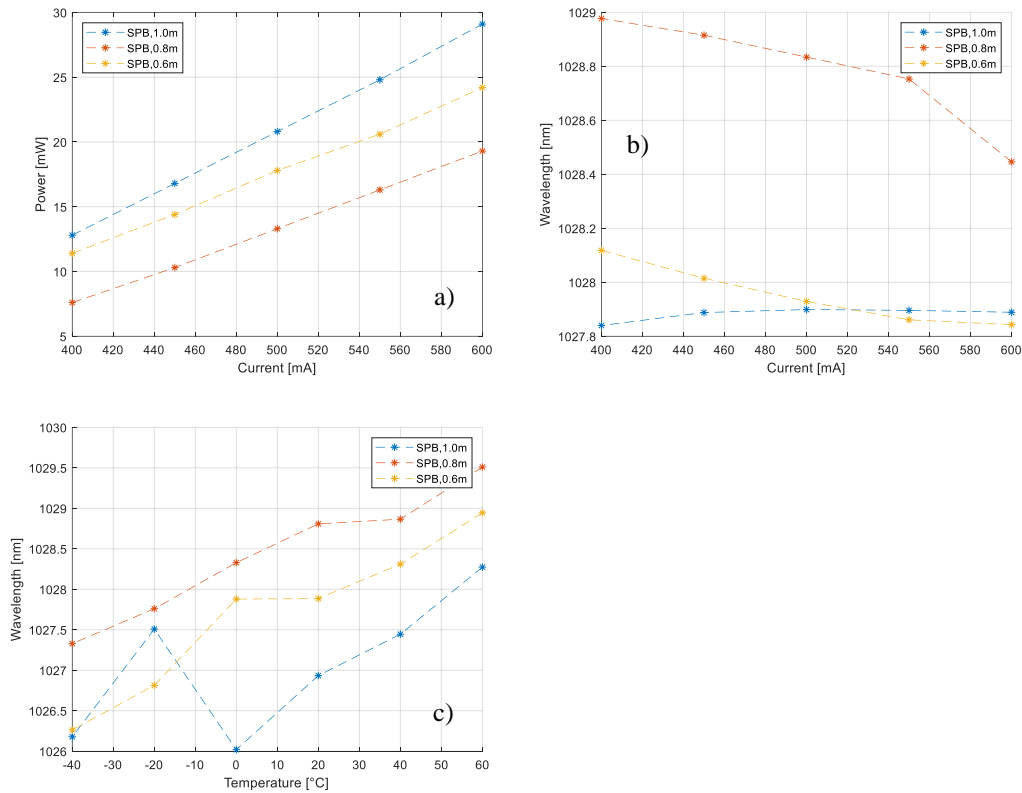


Figure 2.67. SPB a) output power and b) mean wavelength for different Yb-doped fiber lengths. c) Mean wavelength for different temperatures

### 2.7.2.3 Double Pass Forward

Spectrum outputs of DPF configuration for different Yb-doped fiber lengths are given in Figure 2.68 for different pump currents.

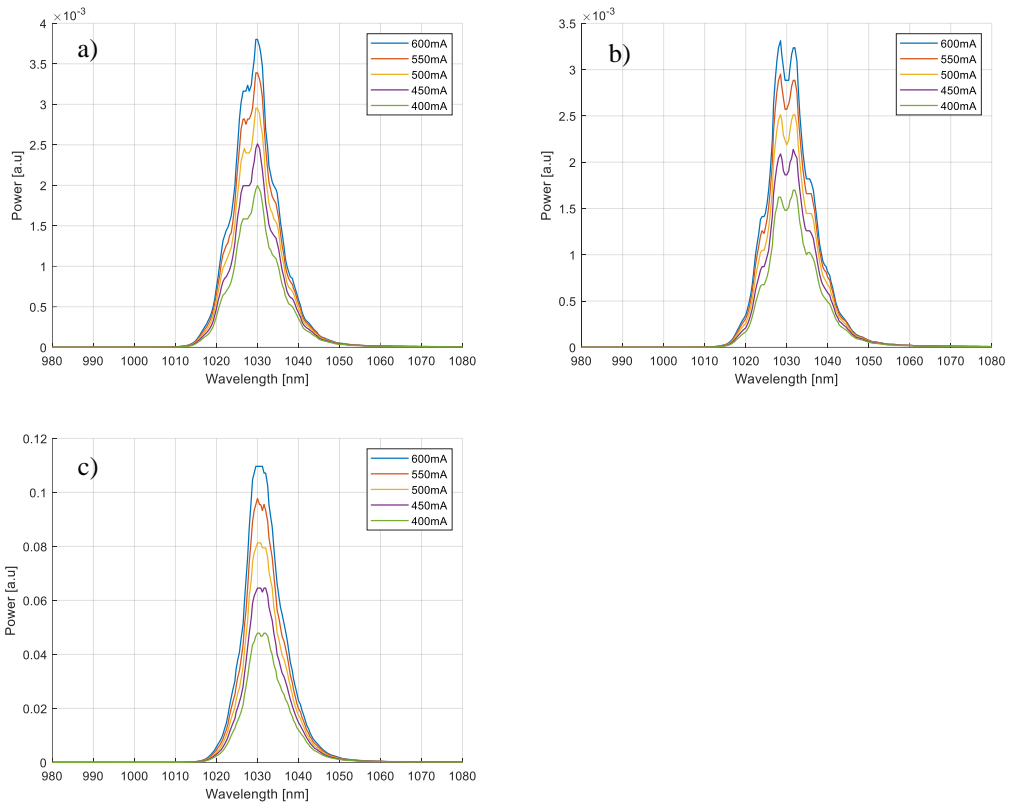


Figure 2.68. DPF configuration output spectrum for different pump currents a) 0.6m b) 0.8m and c) 1.0m

Output power and mean wavelength analysis of SPF configuration are given in Figure 2.69.

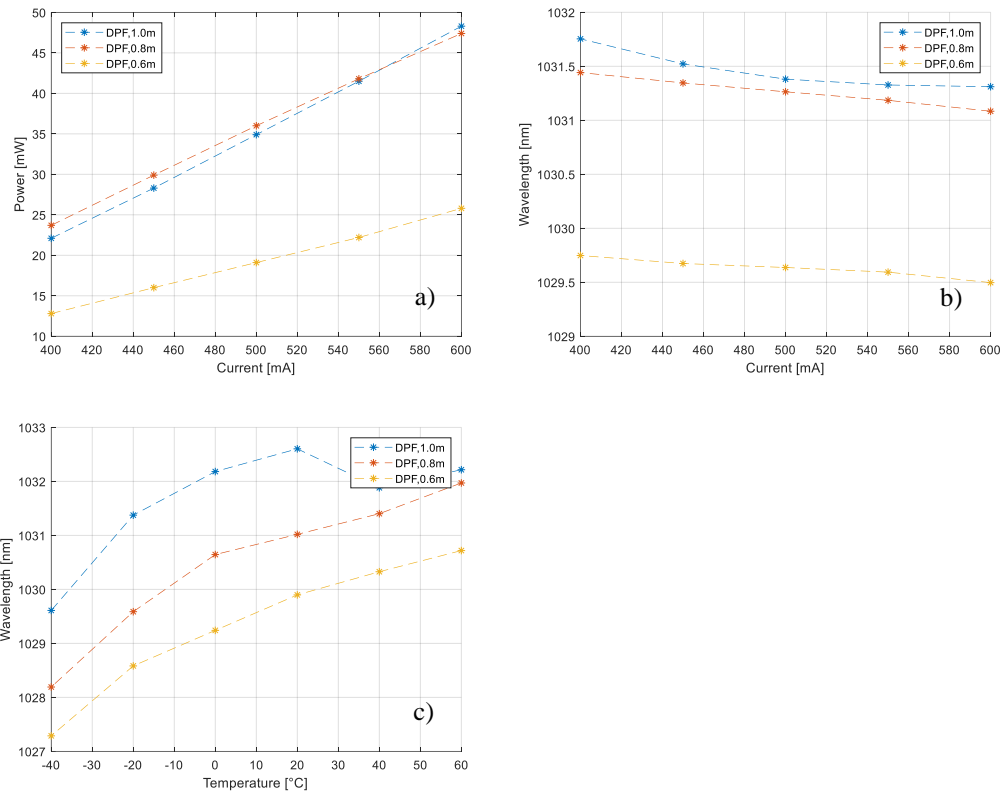


Figure 2.69. DPF a) output power and b) mean wavelength for different Yb-doped fiber lengths. c) Mean wavelength for different temperatures

### 2.7.2.4 Double Pass Backward

Spectrum outputs of SPF configuration for different Yb-doped fiber lengths are given in Figure 2.70 for different pump currents.

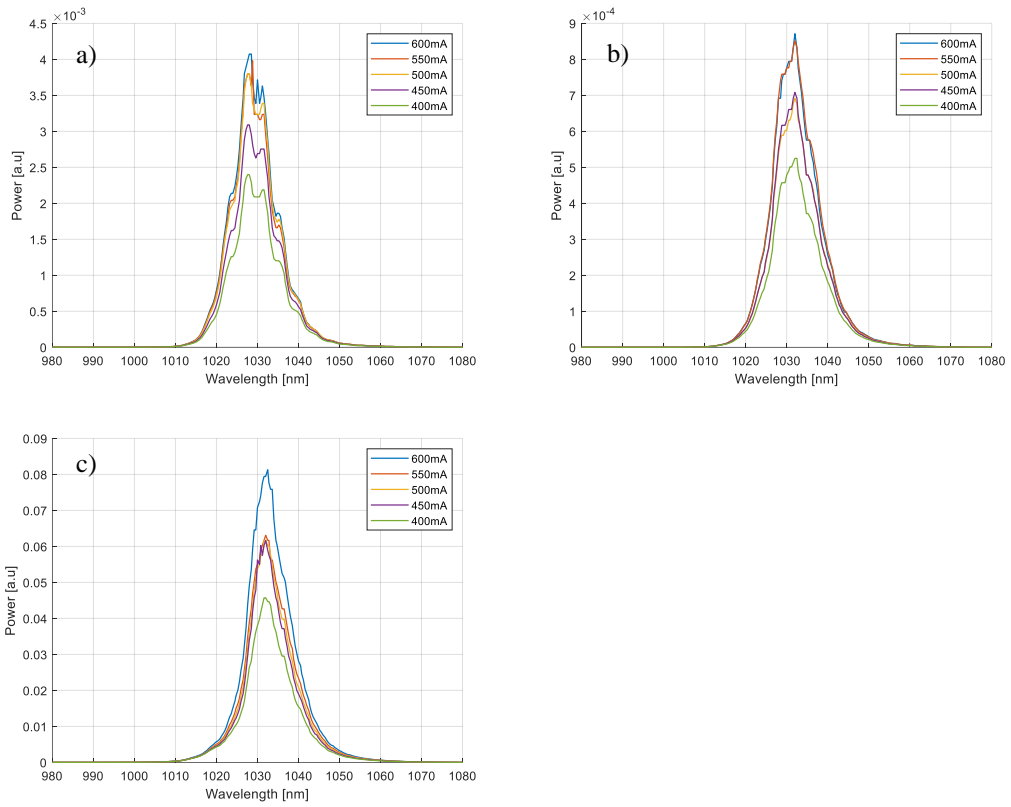


Figure 2.70. DPB configuration output spectrum for different pump currents a) 0.6m b) 0.8m and c) 1.0m

Output power and mean wavelength analysis of SPF configuration are given in Figure 2.71.

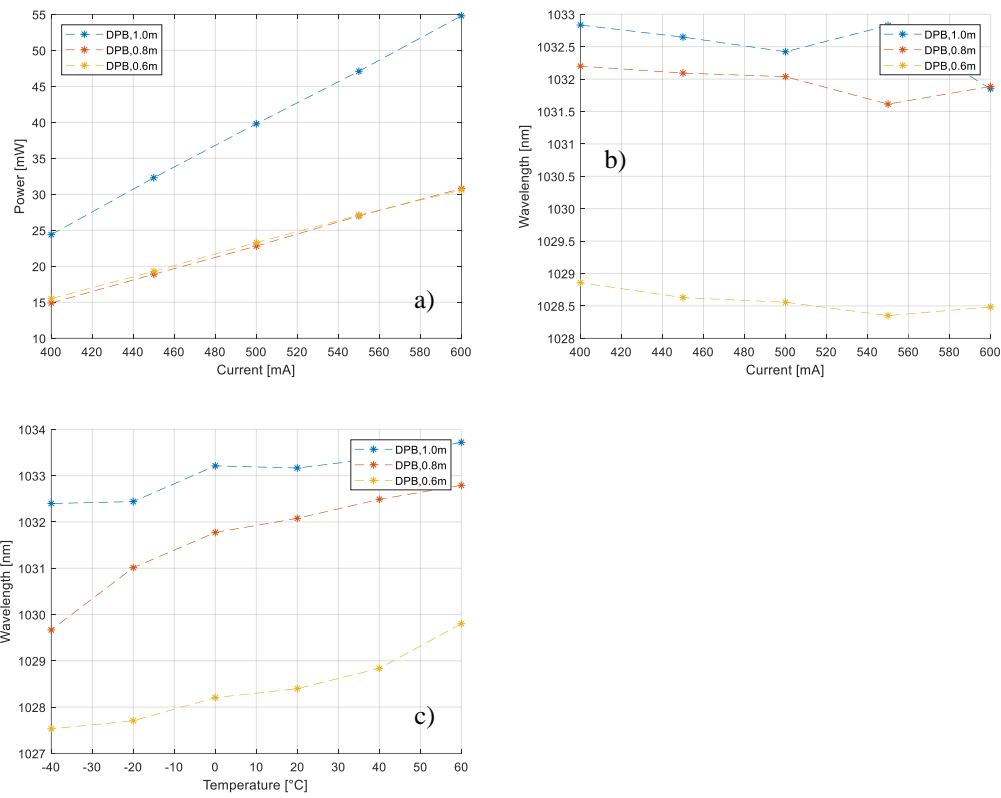


Figure 2.71. DPB a) output power and b) mean wavelength for different Yb-doped fiber lengths. c) Mean wavelength for different temperatures

## 2.7.3 Simulation Results

### 2.7.3.1 Single Pass Forward

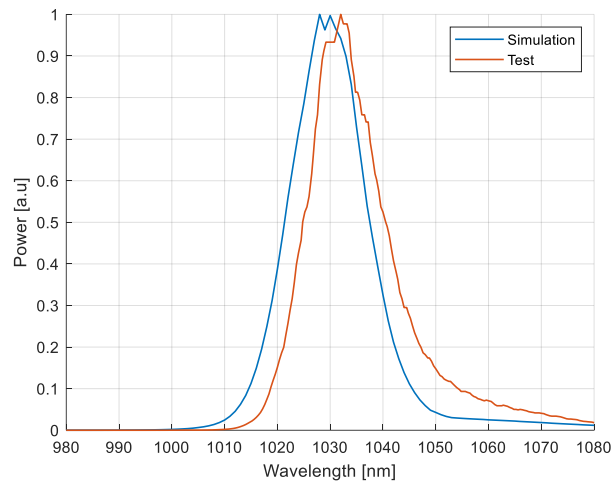


Figure 2.72. SPF spectrum simulation and test result

The mean wavelength for simulation results is 1031.0nm and the mean wavelength for 1.0m Yb-doped fiber test results is 1032.7nm at 500mA pump current. The mean wavelength difference is less than 2nm.

### 2.7.3.2 Single Pass Backward

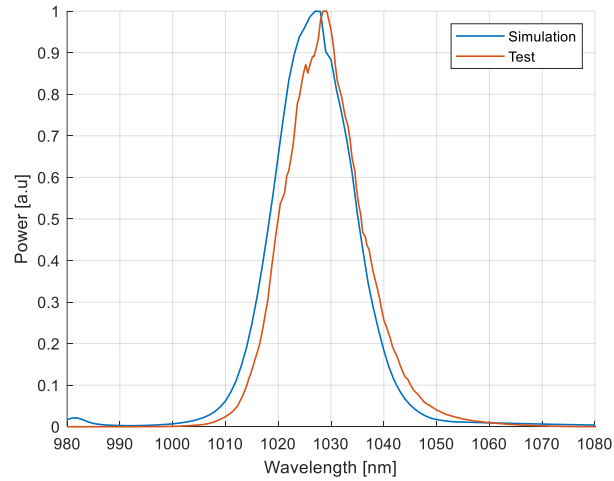


Figure 2.73. SPB spectrum simulation and test result

The mean wavelength for simulation results is 1027.1nm and the mean wavelength for 1.0m Yb-doped fiber test results is 1027.9nm at 500mA pump current. The mean wavelength difference is less than 1nm.

### 2.7.3.3 Double Pass Forward

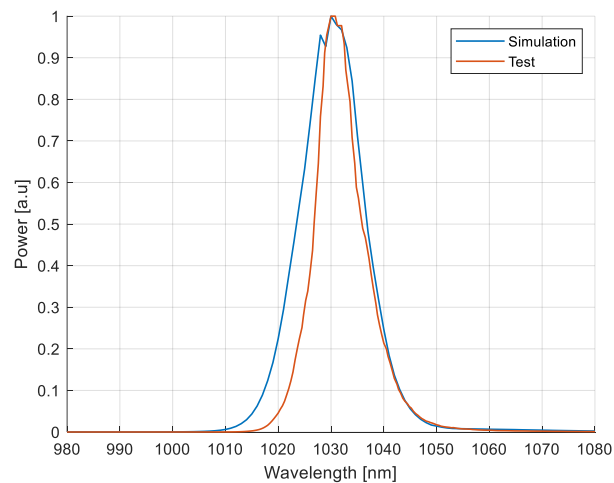


Figure 2.74. DPF spectrum simulation and test result

The mean wavelength for simulation results is 1030.7nm and the mean wavelength for 1.0m Yb-doped fiber test results is 1031.4nm at 500mA pump current. The mean wavelength difference is less than 1nm.

#### 2.7.3.4 Double Pass Backward

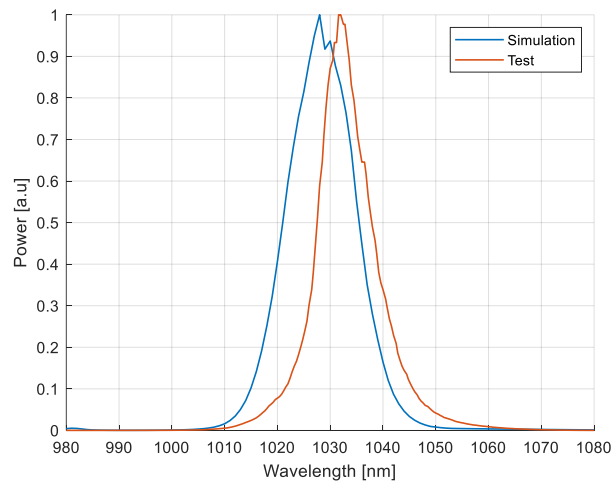


Figure 2.75. DPB spectrum simulation and test result

The mean wavelength for simulation results is 1028.5nm and the mean wavelength for 1.0m Yb-doped fiber test results is 1032.4nm at 500mA pump current. The mean wavelength difference is less than 4nm. The reason for the 4nm difference could be the spectral response of the back reflector in the DPB configuration.



## CHAPTER 3

### IFOG NOISE ANALYSIS

#### 3.1 Noise Types of IFOG

Main noises in gyroscopes can be listed in two categories depending on their time scale: bias instability and angular random walk (ARW). These noise relations are demonstrated in Figure 3.1.

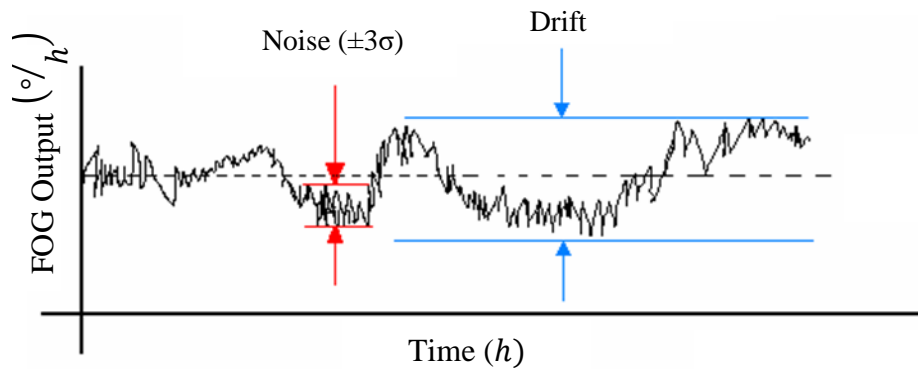


Figure 3.1. Noises in FOG [5]

FOG output is the sum of bias instability and ARW. Bias instability is the shift in gyroscope output in long term. Even if there is no rotation, the gyroscope produces an output due to various reasons and this output varies with time. The main effects causing this noise are the Kerr effect, Faraday effect, Shupe effect and instabilities in electronics.

ARW is the white noise at FOG output effective for short time intervals. ARW can be expressed in terms of the equivalent rotation rate per square root of bandwidth of detection.

Depending on the application ARW or bias instability becomes more dominant. Although bias instability is effective for navigational purposes, ARW is more crucial for control and stabilization applications [5].

Several optical and electronic phenomena are responsible for this noise type. ARW will be investigated detailed in the next sections.

### 3.1.1 Allan Variance Analysis

The frequency stability of oscillators was analyzed using the Allan variance method formerly [68]. Additionally, this technique has been used to characterize random noises in data of any system. The source of noise could be an inherent characteristic of the device or due to the test set-up. Therefore, understanding the physics of the device is critical to evaluate the results. The methodology applies to any inertial sensors such as accelerometers, and gyroscopes.

In general, Allan variance is used to determine five basic gyroscope noise types angular random walk, rate random walk, bias instability, quantization noise, and rate ramp. An Allan variance example and associated noise source are given in Figure 3.2. In this study, the most dominant sources for IFOG such as angular random walk and bias instability are detailed.

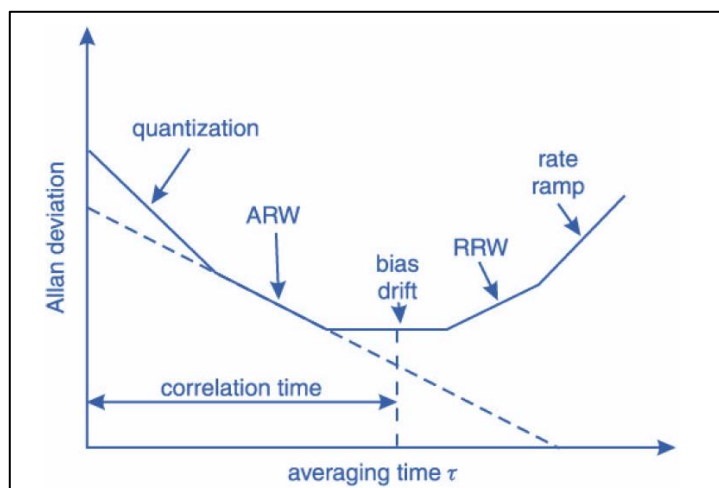


Figure 3.2. Allan variance graph and related noises [69]

Assume gyroscope output has  $N$  number of samples and sampling time interval  $\tau_0$ . Allan variance is a function of cluster intervals that have lengths  $\tau_0, 2\tau_0, \dots, k\tau_0$  ( $k < N/2$ ). Averages of the sum of the data points in each cluster interval over the total length of the cluster give Allan variance [69].

$$\sigma^2(\tau) = \frac{1}{2} \langle (\bar{\Omega}_{k+m} - \bar{\Omega}_k)^2 \rangle \quad (3.1)$$

$$\sigma^2(\tau) = \frac{1}{2\tau^2} \langle (\theta_{k+2m} - 2\theta_{k+m} + \theta_k)^2 \rangle \quad (3.2)$$

Here,  $\bar{\Omega}$  is an average rate calculated as:

$$\bar{\Omega}_k(\tau) = \frac{\theta_{k+m} - \theta_k}{\tau} \quad (3.3)$$

Here,  $\tau = m\tau_0$ . Estimated Allan variance is given as:

$$\sigma^2(\tau) = \frac{1}{2\tau^2(N-2m)} \sum_{k=1}^{N-2m} (\theta_{k+2m} - 2\theta_{k+m} + \theta_k)^2 \quad (3.4)$$

Instead of angular increment, PSD (power spectral density,  $S_\Omega(f)$ ) of output data can be used to calculate Allan's variance.

$$\sigma^2(\tau) = 4 \int_0^{\infty} S_\Omega(f) \frac{\sin^4(\pi f \tau)}{(\pi f \tau)^2} df \quad (3.5)$$

### 3.1.2 Bias Instability

Bias instability has resulted from the flickering of components such as electronics. The noise causes a shift in the output of sensors as bias drift. The PSD of bias instability is given as [69]:

$$S_\Omega(f) = f(x) = \begin{cases} \left(\frac{B^2}{2\pi}\right) \frac{1}{f}, & f \leq f_0 \\ 0, & f > f_0 \end{cases} \quad (3.6)$$

Here,  $B$  is the coefficient of bias instability,  $f_0$  is the cutoff frequency.

Using Equation (3.1), a variance of bias instability can be calculated as:

$$\sigma^2(\tau) = \frac{2B^2}{\pi} \left[ \ln 2 - \frac{\sin^3 x}{2x^2} (\sin x + 4x \cos x) + Ci(2x) + Ci(4x) \right] \quad (3.7)$$

Here,  $x$  is  $\pi f_0 \tau$ ,  $Ci$  is the cosine integral function.

In Figure 3.3, a log-log plot of Equation (3.7) is given. After cutoff frequency, Allan variance for bias instability flattens at which the values of this noise and cutoff frequency can be estimated for any sensor.

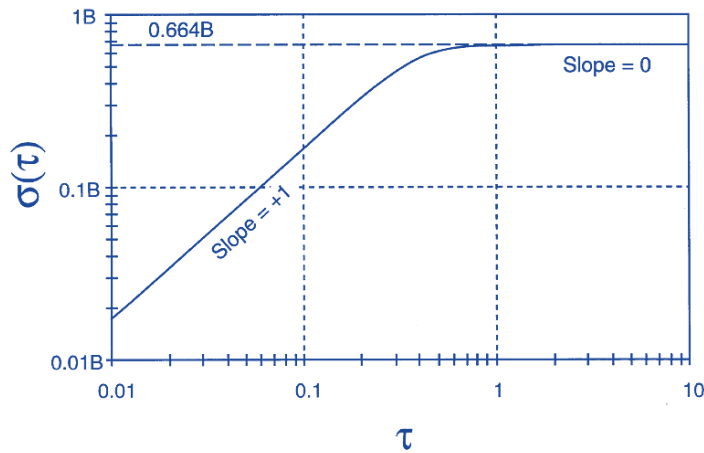


Figure 3.3. Bias instability parameter variance plot [69]

### 3.1.3 Angular Random Walk

Angular random walk is a white noise type error. The components of this noise will be detailed in the next section. The dominant source for angular random walk error is the spontaneous emission of photons which is characteristic of the light source. Therefore, the angle random walk cannot be eliminated and determines the quantum limit performance of the sensor [69].

Gyroscope angular random walk has noise components whose correlation time is shorter than the sampling time interval. Nevertheless, most of these noises can be prevented with design measures. These noise terms are all presented by a white noise characteristic of the gyroscope output. The related rate noise PSD is given by:

$$S_{\Omega}(f) = N^2 \quad (3.8)$$

Here,  $N$  is the coefficient of the angle random walk. Using Equation (3.8), a variance of bias instability can be calculated as:

$$\sigma^2(\tau) = \frac{N^2}{\tau} \quad (3.9)$$

In Figure 3.4, a log-log plot of Equation (3.9). The slope of data is  $-1/2$ . Moreover, the numerical value of  $N$  corresponds directly value of the slope line at  $\tau = 1$ .

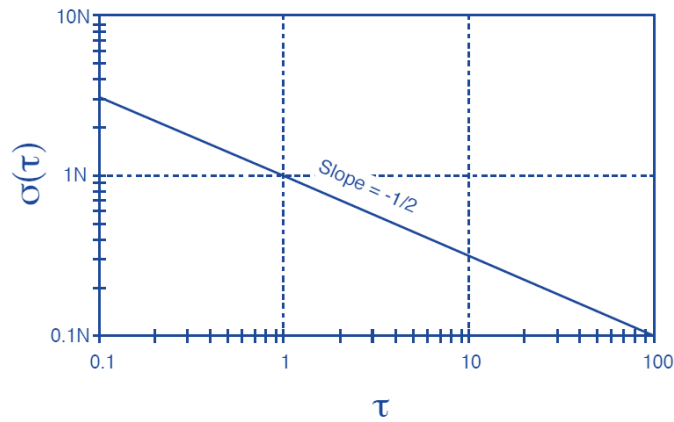


Figure 3.4. Angle random walk parameter variance plot [69]

## 3.2 Noise Analysis

### 3.2.1 Two-level Modulation

Each of the two modulation levels gives a current output at the photodiode as follows [70], [71]:

$$I_1(\Delta\Phi_R, \Phi_m, \sigma_{i,1}) = \frac{I_0}{2} [1 + \cos(\Delta\Phi_R + \pi - \Phi_m)] + \sigma_{i,1} \quad (3.10)$$

$$I_2(\Delta\Phi_R, \Phi_m, \sigma_{i,2}) = \frac{I_0}{2} [1 + \cos(\Delta\Phi_R - \pi + \Phi_m)] + \sigma_{i,2} \quad (3.11)$$

$I_i$  is the current output of the photodiode at each level,  $I_0$  is maximum current output,  $\Delta\Phi_R$  is phase shift due to rotation,  $\Phi_m$  is modulation depth,  $\sigma_{i,j}$  is current noise at  $j^{\text{th}}$  level modulation. In order to calculate the rotation angle, the second current level can be subtracted from the first current level and the difference will be as follows:

$$\Delta I = I_2(\Delta\Phi_R, \Phi_m, \sigma_{i,2}) - I_1(\Delta\Phi_R, \Phi_m, \sigma_{i,1}) \quad (3.12)$$

Put Equations (3.10) and (3.11) into (3.12):

$$\Delta I = \frac{I_0}{2} [1 + \cos(\Delta\Phi_R - \pi + \Phi_m) - 1 - \cos(\Delta\Phi_R + \pi - \Phi_m)] + \sigma_{i,2} - \sigma_{i,1} \quad (3.13)$$

Using the property of cosine function:

$$\cos(\Delta\Phi_R - \pi + \Phi_m) = -\cos(\Delta\Phi_R + \Phi_m) \quad (3.14)$$

The current difference will be:

$$\Delta I = \frac{I_0}{2} [-\cos(\Delta\Phi_R + \Phi_m) + \cos(\Delta\Phi_R - \Phi_m)] + \sigma_{i,2} - \sigma_{i,1} \quad (3.15)$$

Using the property of cosine identity:

$$\Delta I = \frac{I_0}{2} [-\cos(\Delta\Phi_R) \cos(\Phi_m) + \sin \Delta\Phi_R \sin \Phi_m + \cos(\Delta\Phi_R) \cos(\Phi_m) + \sin \Delta\Phi_R \sin \Phi_m] + \sigma_{i,2} - \sigma_{i,1} \quad (3.16)$$

The first and third terms cancel each other.

$$\Delta I = I_0 [\sin \Delta\Phi_R \sin \Phi_m] + \sigma_{i,2} - \sigma_{i,1} \quad (3.17)$$

The addition of uncorrelated noises gives:

$$\sigma^2 = \sigma_1^2 \pm \sigma_2^2 \quad (3.18)$$

Final FOG output is given as:

$$\Delta I = I_0 [\sin \Delta\Phi_R \sin \Phi_m] + \sqrt{2}\sigma_i \quad (3.19)$$

Leave phase difference due to rotation and use small angle approximation:

$$\Delta\Phi_R \approx \frac{\Delta I}{I_0 \sin \Phi_m} - \frac{\sqrt{2}\sigma_i}{I_0 \sin \Phi_m} \quad (3.20)$$

The second term gives the  $i^{\text{th}}$  noise contribution on rotation phase change.

$$\sigma_{R,i} = \frac{\sqrt{2}\sigma_i}{I_0 \sin \Phi_m} \quad (3.21)$$

Sensitivity to noise is related to the sampling of current. Therefore, noise spectral density should be considered as:

$$N_i = \frac{\sigma_i}{\sqrt{\Delta f}} \quad (3.22)$$

Electronic bandwidth is defined as:

$$\Delta f = \frac{1}{2t_s} \quad (3.23)$$

where  $t_s$  is sampling time. The phase noise per unit bandwidth will be:

$$\frac{\sigma_{R,i}}{\sqrt{\Delta f}} = \frac{\sqrt{2}N_i}{I_0 \sin \Phi_m} \quad (3.24)$$

### 3.2.2 Four-level Modulation

Each of the four modulation levels gives a current output at the photodiode as follows:

$$I_1(\Delta\Phi_R, \Phi_m, \sigma_{i,1}) = \frac{I_0}{2} [1 + \cos(\Delta\Phi_R + \pi - \Phi_m)] + \sigma_{i,1} \quad (3.25)$$

$$I_2(\Delta\Phi_R, \Phi_m, \sigma_{i,2}) = \frac{I_0}{2} [1 + \cos(\Delta\Phi_R + \pi + \Phi_m)] + \sigma_{i,2} \quad (3.26)$$

$$I_3(\Delta\Phi_R, \Phi_m, \sigma_{i,3}) = \frac{I_0}{2} [1 + \cos(\Delta\Phi_R - \pi + \Phi_m)] + \sigma_{i,3} \quad (3.27)$$

$$I_4(\Delta\Phi_R, \Phi_m, \sigma_{i,4}) = \frac{I_0}{2} [1 + \cos(\Delta\Phi_R - \pi - \Phi_m)] + \sigma_{i,4} \quad (3.28)$$

Subtract levels one and four from two and three to get the phase of rotation.

$$\begin{aligned} \Delta I = & [I_2(\Delta\Phi_R, \Phi_m, \sigma_{i,2}) + I_3(\Delta\Phi_R, \Phi_m, \sigma_{i,3})] \\ & - [I_1(\Delta\Phi_R, \Phi_m, \sigma_{i,1}) + I_4(\Delta\Phi_R, \Phi_m, \sigma_{i,4})] \end{aligned} \quad (3.29)$$

Using similar steps as section 3.2.1:

$$\Delta I = 2I_0[\sin \Delta\Phi_R \sin \Phi_m] + \sigma_{i,2} + \sigma_{i,3} - \sigma_{i,1} - \sigma_{i,4} \quad (3.30)$$

The addition of uncorrelated noises gives:

$$\sigma^2 = \sigma_1^2 \pm \sigma_2^2 \pm \sigma_3^2 \pm \sigma_4^2 \quad (3.31)$$

The difference will be:

$$\Delta I = 2I_0[\sin \Delta\Phi_R \sin \Phi_m] + 2\sigma_i \quad (3.32)$$

Use small angle approximation and leave phase difference due to rotation:

$$\Delta\Phi_R \approx \frac{\Delta I}{2I_0 \sin \Phi_m} - \frac{\sigma_i}{I_0 \sin \Phi_m} \quad (3.33)$$

The second term gives the noise on phase change due to rotation for four-level modulation.

$$\sigma_{R,i} = \frac{\sigma_i}{I_0 \sin \Phi_m} \quad (3.34)$$

Using the same definitions as before the phase noise per unit bandwidth will be:

$$\frac{\sigma_{R,i}}{\sqrt{\Delta f}} = \frac{N_i}{I_0 \sin \Phi_m} \quad (3.35)$$

The result is dependent on modulation depth. Four-level modulation has a two-fold signal increase and  $\sqrt{2}$  fold noise increases with respect to two-level modulation.

The resultant signal-to-noise is increased by  $\sqrt{2}$  fold.

### 3.3 Sources of ARW

Sources of noise are displayed in Figure 3.5. In the next sections, these noises in the fiber optic gyroscopes are analyzed.

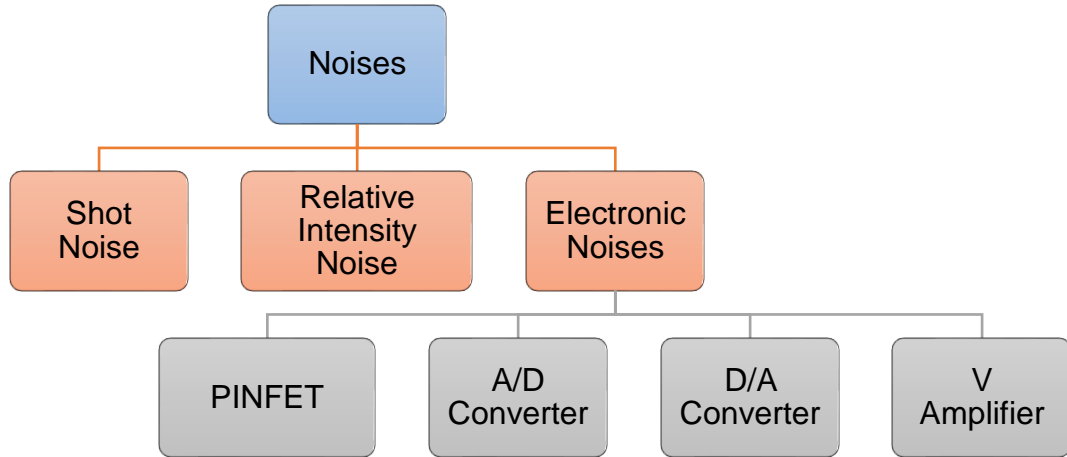


Figure 3.5. Noise sources in FOG

#### 3.3.1 Shot Noise

In theory, FOG measurement is limited by shot noise which is caused by a random distribution of photons on the detection device. Shot noise is also called photon noise. In other words, photons form a statistical distribution of sigma in unit time. In this study, PINFET output fluctuates due to this randomness which can be expressed by Poisson probability distribution [72]. In unit time  $t$ , an average number of photons can be calculated by dividing total average energy by photon energy.

$$\bar{N} = \frac{\bar{E}}{\varepsilon} \quad (3.36)$$

$\bar{E}$  is total average energy given as:

$$\bar{E} = \frac{1}{2} \bar{P}_0 t \quad (3.37)$$

where  $\bar{P}_0$  is average optical power. Photon energy:

$$\varepsilon = h\nu \quad (3.38)$$

$h$  is Plank's constant and  $\nu$  is the optical frequency of the photon. Average photon number is given by:

$$\bar{N} = \frac{1}{2} \frac{\bar{P}_0 t}{h\nu} \quad (3.39)$$

The standard deviation of the photon number is proportional to the square root of the average photon number:

$$\sigma_N = \sqrt{\langle N^2 \rangle - \langle N \rangle^2} = \sqrt{\bar{N}} \quad (3.40)$$

The relation between power and current is given as:

$$\bar{I}_0 = \frac{\bar{P}_0 e}{h\nu} \quad (3.41)$$

Shot noise is given as:

$$\sigma_S = \frac{e}{t} \sqrt{\bar{N}} = \sqrt{2eI\Delta f} \quad (3.42)$$

Here,  $e$  is the charge of an electron.

$$\frac{\sigma_S}{\sqrt{\Delta f}} = N_S = \sqrt{2eI} \quad (3.43)$$

Phase noise due to shot noise can be calculated as:

$$\frac{\sigma_{R,S}}{\sqrt{\Delta f}} = \frac{N_S}{I_0 \sin \Phi_m} = \frac{\sqrt{2eI}}{I_0 \sin \Phi_m} \quad (3.44)$$

Using interference equation:

$$\frac{\sigma_{R,S}}{\sqrt{\Delta f}} = \frac{\sqrt{2e \frac{I_0}{2} (1 + \cos(\Phi_m))}}{I_0 \sin \Phi_m} \quad (3.45)$$

Trigonometric identities and simplification give the final result.

$$\frac{\sigma_{R,S}}{\sqrt{\Delta f}} = \sqrt{\frac{e}{2I_0}} \frac{1}{\sin\left(\frac{\Phi_m}{2}\right)} \quad (3.46)$$

### 3.3.2 Relative Intensity Noise

Low-coherence sources such as Er or Yb-doped ASE sources have a spectrum with broad bandwidth. Many wavelengths in this spectrum beat against other wavelengths. This results in relative intensity noise (RIN) [73].

$$\sigma_{RIN} = I \sqrt{\frac{\Delta f}{\Delta \nu}} \quad (3.47)$$

$\Delta \nu$  is frequency bandwidth and can be calculated by:

$$\Delta \nu = \frac{[\int P(\nu) d\nu]^2}{\int P^2(\nu) d\nu} \quad (3.48)$$

where  $P(\nu)$  is the power spectral density of the optical spectrum of the light source. Equation (3.47) shows that the broader spectrum decreases the RIN.

$$\frac{\sigma_{RIN}}{\sqrt{\Delta f}} = N_{RIN} = I \sqrt{\frac{1}{\Delta \nu}} \quad (3.49)$$

Phase noise due to RIN can be calculated as:

$$\frac{\sigma_{R,RIN}}{\sqrt{\Delta f}} = \frac{N_{RIN}}{I_0 \sin \Phi_m} = \frac{I}{I_0 \sin \Phi_m} \sqrt{\frac{1}{\Delta \nu}} \quad (3.50)$$

$$\frac{\sigma_{R,RIN}}{\sqrt{\Delta f}} = \frac{I_0 (1 + \cos(\Phi_m))}{I_0 \sin \Phi_m} \sqrt{\frac{1}{\Delta v}} \quad (3.51)$$

Using trigonometric identities:

$$\frac{\sigma_{R,RIN}}{\sqrt{\Delta f}} = \frac{1}{2\sqrt{\Delta v} \tan\left(\frac{\Phi_m}{2}\right)} \quad (3.52)$$

### 3.3.3 Electronic Noises

The main electronic noise contributors are PINFET, analog to digital converter ADC, digital to analog converter DAC and voltage amplifier.

#### 3.3.3.1 Photodiode Noises

A photodetector in this case PINFET creates current with incident optical power. The current is converted to voltage and amplified via the amplifier part of PINFET. A basic TIA as an equivalent circuit is modeled in Figure 3.6 [74].

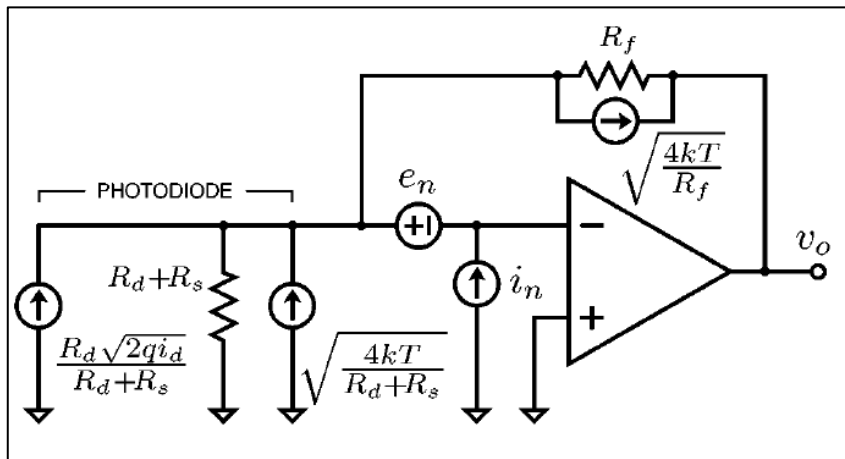


Figure 3.6. Equivalent circuit of a transimpedance amplifier

Each element in this circuit experiences a certain type of noise. The noise voltage spectral density of these noises can be calculated in Equation (3.53):

$$v_0^2 = \left[ \underbrace{\frac{2ei_d R_d^2}{(R_s + R_d)^2}}_{\substack{\text{Dark} \\ \text{Current} \\ \text{Shot} \\ \text{Noise}}} + \underbrace{\frac{4k_b T}{R_s + R_d}}_{\substack{\text{Photod.} \\ \text{Johnson} \\ \text{Noise}}} + \underbrace{i_{n,TIA}^2}_{\substack{\text{Op-Amp} \\ \text{Current} \\ \text{Noise}}} + \underbrace{\frac{4k_b T}{R_f}}_{\substack{\text{Feedb.} \\ \text{Resistor} \\ \text{Johnson} \\ \text{Noise}}} \right] R_f^2 + \underbrace{v_{n,TIA}^2 \left(1 + \frac{R_f}{R_s + R_d}\right)^2}_{\substack{\text{Op-Amp} \\ \text{Voltage Noise}}} \quad (3.53)$$

where  $i_d$  dark current,  $R_d$  photodiode dynamic resistance,  $R_s$  photodiode series resistance,  $k_b$  Boltzmann constant,  $T$  temperature,  $i_{n,TIA}$  op-amp input noise current spectral density,  $R_f$  feedback resistance,  $v_{n,TIA}$  op-amp input noise voltage spectral density. Equation (3.53) consists of dark current Shot noise, photodetector Johnson noise, op-amp input noise current noise, feedback resistance Johnson noise and op-amp voltage noise as the last term.

Using practical assumptions, Equation (3.53) can be simplified. In general,  $R_d$  is much larger than  $R_s$  and  $R_f$  which gives the result:

$$v_0^2 \approx \left[ 2ei_d + i_{n,TIA}^2 + \frac{4k_b T}{R_f} \right] R_f^2 + v_{n,TIA}^2 \quad (3.54)$$

The total noise of current spectral density can be calculated as:

$$N_p = i_0 = \frac{v_0}{R_f} \approx \sqrt{2ei_d + i_{n,TIA}^2 + \frac{4k_b T}{R_f} + \frac{v_{n,TIA}^2}{R_f^2}} \quad (3.55)$$

Phase noise due to PINFET total noise:

$$\frac{\sigma_{R,P}}{\sqrt{\Delta f}} = \frac{N_p}{I_0 \sin \Phi_m} = \frac{\sqrt{2ei_d + i_{n,TIA}^2 + \frac{4k_b T}{R_f} + \frac{v_{n,TIA}^2}{R_f^2}}}{I_0 \sin \Phi_m} \quad (3.56)$$

### 3.3.3.2 A/D Converter Noise

Voltage noise density of A/D converter ( $v_{ADC}$ ) of electronics is given in volts per square root of bandwidth. In order to convert this value to current noise, noise density should be divided by resistance.

$$N_{ADC} = \frac{\sigma_{ADC}}{\sqrt{\Delta f}} = \frac{v_{ADC}}{R_f} \quad (3.57)$$

Phase noise due to ADC:

$$\frac{\sigma_{R,ADC}}{\sqrt{\Delta f}} = \frac{N_{ADC}}{I_0 \sin \Phi_m} = \frac{v_{ADC}}{R_f I_0 \sin \Phi_m} \quad (3.58)$$

### 3.3.3.3 D/A Converter Noise

At this stage, noise in the D/A converter and voltage amplifier of MIOC create phase noise in an interferometer. Therefore, phase noise analysis should be carried out instead of current noise. Starting with four modulation levels with phase noise:

$$I_1(\Delta\Phi_R, \Phi_m, \sigma_{i,1}) = \frac{I_0}{2} [1 + \cos(\Delta\Phi_R + \pi - \Phi_m + \sigma_{i,1})] \quad (3.59)$$

$$I_2(\Delta\Phi_R, \Phi_m, \sigma_{i,2}) = \frac{I_0}{2} [1 + \cos(\Delta\Phi_R + \pi + \Phi_m + \sigma_{i,2})] \quad (3.60)$$

$$I_3(\Delta\Phi_R, \Phi_m, \sigma_{i,3}) = \frac{I_0}{2} [1 + \cos(\Delta\Phi_R - \pi + \Phi_m + \sigma_{i,3})] \quad (3.61)$$

$$I_4(\Delta\Phi_R, \Phi_m, \sigma_{i,4}) = \frac{I_0}{2} [1 + \cos(\Delta\Phi_R - \pi - \Phi_m + \sigma_{i,4})] \quad (3.62)$$

$\sigma_{i,j}$  is directly phase noise instead of current noise at the  $j^{\text{th}}$  modulation level. The current difference will be:

$$\Delta I = [I_2(\Delta\Phi_R, \Phi_m, \sigma_{i,2}) + I_3(\Delta\Phi_R, \Phi_m, \sigma_{i,3})] - [I_1(\Delta\Phi_R, \Phi_m, \sigma_{i,1}) + I_4(\Delta\Phi_R, \Phi_m, \sigma_{i,4})] \quad (3.63)$$

$$\Delta I = \frac{I_0}{2} [\cos(\Delta\Phi_R + \pi + \Phi_m + \sigma_{i,2}) + \cos(\Delta\Phi_R - \pi + \Phi_m + \sigma_{i,3}) - \cos(\Delta\Phi_R + \pi - \Phi_m + \sigma_{i,1}) - \cos(\Delta\Phi_R - \pi - \Phi_m + \sigma_{i,4})] \quad (3.64)$$

Using the property of cosine function:

$$\cos(\Delta\Phi_R - \pi + \Phi_m) = -\cos(\Delta\Phi_R + \Phi_m) \quad (3.65)$$

The current difference will be:

$$\Delta I = \frac{I_0}{2} [-\cos(\Delta\Phi_R + \Phi_m + \sigma_{i,2}) - \cos(\Delta\Phi_R + \Phi_m + \sigma_{i,3}) + \cos(\Delta\Phi_R - \Phi_m + \sigma_{i,1}) + \cos(\Delta\Phi_R - \Phi_m + \sigma_{i,4})] \quad (3.66)$$

Using the property of cosine identity:

$$\Delta I = 2I_0 \left[ \sin\left(\Delta\Phi_R + \frac{\sigma_{i,1} + \sigma_{i,2} + \sigma_{i,3} + \sigma_{i,4}}{4}\right) \sin\left(\Phi_m + \frac{\sigma_{i,1} + \sigma_{i,4} - \sigma_{i,2} - \sigma_{i,3}}{4}\right) \right] \quad (3.67)$$

The addition of uncorrelated noises gives:

$$\sigma^2 = \sigma_1^2 \pm \sigma_2^2 \pm \sigma_3^2 \pm \sigma_4^2 \quad (3.68)$$

$$\Delta I = 2I_0 \sin\left(\Delta\Phi_R + \frac{2\sigma_i}{4}\right) \sin\left(\Phi_m + \frac{2\sigma_i}{4}\right) \quad (3.69)$$

and use small angle approximation:

$$\Delta I = 2I_0 \left( \Delta\Phi_R + \frac{2\sigma_i}{4} \right) \sin(\Phi_m) \quad (3.70)$$

Leave phase difference due to rotation

$$\Delta\Phi_R \approx \frac{\Delta I}{2I_0 \sin \Phi_m} - \frac{\sigma_i}{2} \quad (3.71)$$

The second term gives the noise on phase change due to rotation for four-level modulation.

$$\sigma_{R,i} = \frac{\sigma_i}{2} \quad (3.72)$$

Using the same definitions as before the phase noise per unit bandwidth will be:

$$\frac{\sigma_{R,i}}{\sqrt{\Delta f}} = \frac{N_i}{2} \quad (3.73)$$

If  $N_i$  is power spectral density of D/A converter voltage, corresponding phase noise can be calculated by considering  $V_\pi$  which is the voltage applied to create  $\pi$  phase difference:

$$\frac{\sigma_{R,DAC}}{\sqrt{\Delta f}} = \frac{v_{DAC}\pi}{2V_\pi} \quad (3.74)$$

Here,  $v_{ADC}$  is the voltage noise density of the D/A converter.

### 3.3.3.4 Voltage Amplifier Noise

Similar to D/A voltage, voltage amplifier noise should be converted to phase noise using  $V_\pi$ :

$$\frac{\sigma_{R,VA}}{\sqrt{\Delta f}} = \frac{v_{VA}\pi}{2V_\pi} \quad (3.75)$$

Here,  $v_{VA}$  is the voltage noise density of the voltage amplifier.

### 3.3.4 Total ARW of FOG

The total rotation rate noise per bandwidth due to electronics is the sum of PINFET, A/D converter, D/A converter and voltage amplifier noises.

$$\frac{\sigma_{R,E}}{\sqrt{\Delta f}} = \sqrt{\left(\frac{\sigma_{R,P}}{\sqrt{\Delta f}}\right)^2 + \left(\frac{\sigma_{R,ADC}}{\sqrt{\Delta f}}\right)^2 + \left(\frac{\sigma_{R,DAC}}{\sqrt{\Delta f}}\right)^2 + \left(\frac{\sigma_{R,VA}}{\sqrt{\Delta f}}\right)^2} \quad (3.76)$$

Total rotation rate noise is the sum of shot noise, relative intensity noise and electronic noise.

$$\frac{\sigma_R}{\sqrt{\Delta f}} = \sqrt{\left(\frac{\sigma_{R,S}}{\sqrt{\Delta f}}\right)^2 + \left(\frac{\sigma_{R,RIN}}{\sqrt{\Delta f}}\right)^2 + \left(\frac{\sigma_{R,E}}{\sqrt{\Delta f}}\right)^2} \quad \left[rad/s\sqrt{Hz}\right] \quad (3.77)$$

In order to calculate the ARW scale factor of FOG should be considered. Instead of expressing per square root of Hz, per square root of the hour is used commonly.

$$ARW = \frac{\sigma_R}{\sqrt{\Delta f}} \cdot \frac{1}{SF} \cdot \sqrt{\frac{3600s}{1hr}} \quad \left[rad/s\sqrt{Hz}\right] \quad (3.78)$$

Phase noise can be converted to angular quantity in terms of degrees by:

$$ARW = \frac{\sigma_R}{\sqrt{\Delta f}} \cdot \frac{1}{SF} \cdot \sqrt{\frac{t_s}{t_{int}}} \cdot \frac{180}{\pi} \cdot 60 \quad \left[^\circ/\sqrt{h}\right] \quad (3.79)$$

Sampling ( $t_s$ ) and integration time ( $t_{int}$ ) of data are also included.

Equation (3.79) can be used to identify the dominant noise type of a FOG. Additionally, wavelength-dependent RIN can be reduced by decreasing the mean wavelength of IFOG while SF is also improved. Consequently, the Yb-doped ASE source which has a shorter central wavelength compared to the Er-doped ASE source results from better ARW performance. This theoretical improvement in ARW performance is shown in Figure 3.7. The effect of optical power at the photodiode on ARW is displayed for each wavelength.

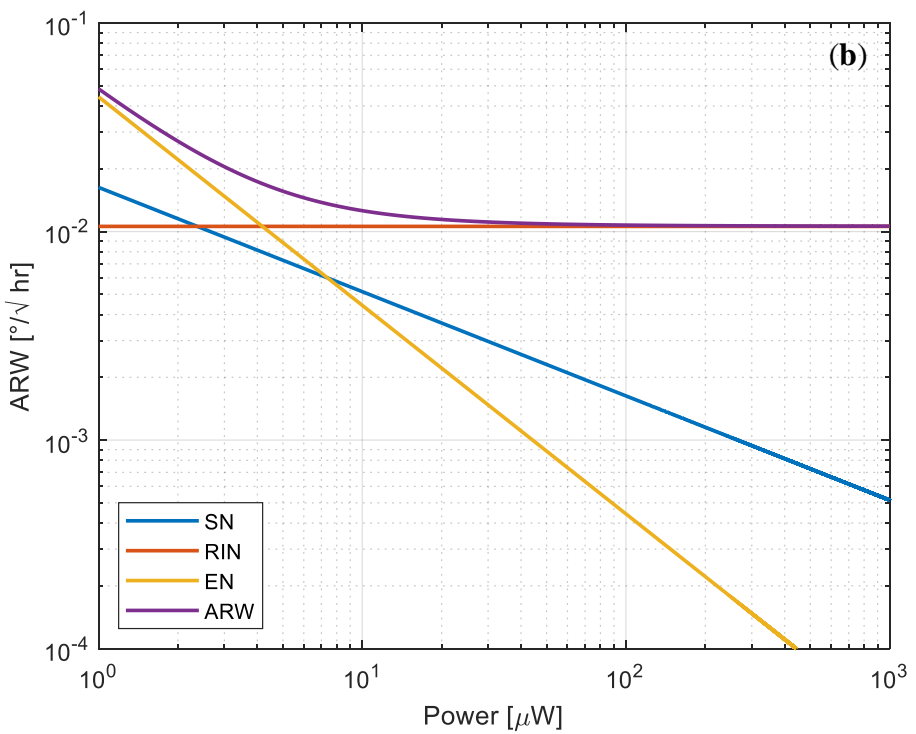
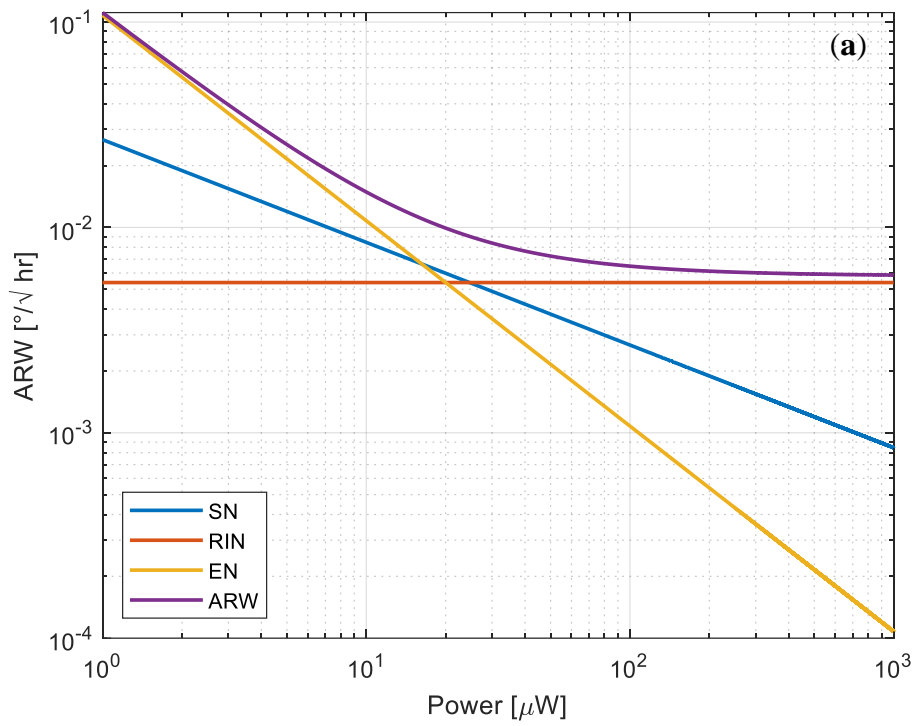


Figure 3.7. ARW analysis of (a) 1030nm; (b) 1550nm FOG

The low optical power at the photodetector exhibits EN as the dominant noise source type. If the optical power is above 10 $\mu$ W, ARW is limited by RIN. Using a 1030nm ASE source improves ARW about 2-fold theoretically assuming the same optical power at PINFET for each wavelength of about 100 $\mu$ W. Er-doped ASE source is limited to about 100 $\mu$ W optical power in this case. However, the Yb-doped ASE source is limited to about 200 $\mu$ W optical power which results in better ARW values for IFOG.

### 3.4 Phase Noise and SNR Optimization

In Equation (3.33), the first term is the phase change due to rotation for four-level modulation and the second term gives the noise on phase change due to rotation. The ratio of the first and the second term gives a signal-to-noise ratio (SNR) value as [75]:

$$SNR = \frac{\frac{\Delta I}{2I_0 \sin \Phi_m}}{\frac{\sigma_i}{I_0 \sin \Phi_m}} \quad (3.80)$$

After simplifying SNR can be calculated using:

$$SNR = \frac{\Delta I}{2\sigma_i} \quad (3.81)$$

The noise ( $\sigma_i$ ) at the photodetector that matches a specific noise level of phase change in the interferometer. The minimum detectable rotation rate is limited by this noise level. The optical power of the light source is very critical for the noise component at a detector. Consequently, optical power has to be optimized and controlled in order to optimize the ratio between phase difference due to rotation and phase noise level. Phase signal which is optimal at  $\Phi_m = \pi/2$  is shown in Figure 3.8. The noise and SNR values are analyzed for 1030nm at 100 $\mu$ W and 105 $\mu$ W optical. Earth rotation rate at a latitude of 39.93 $^\circ$  is used as input rotation that results from phase change.

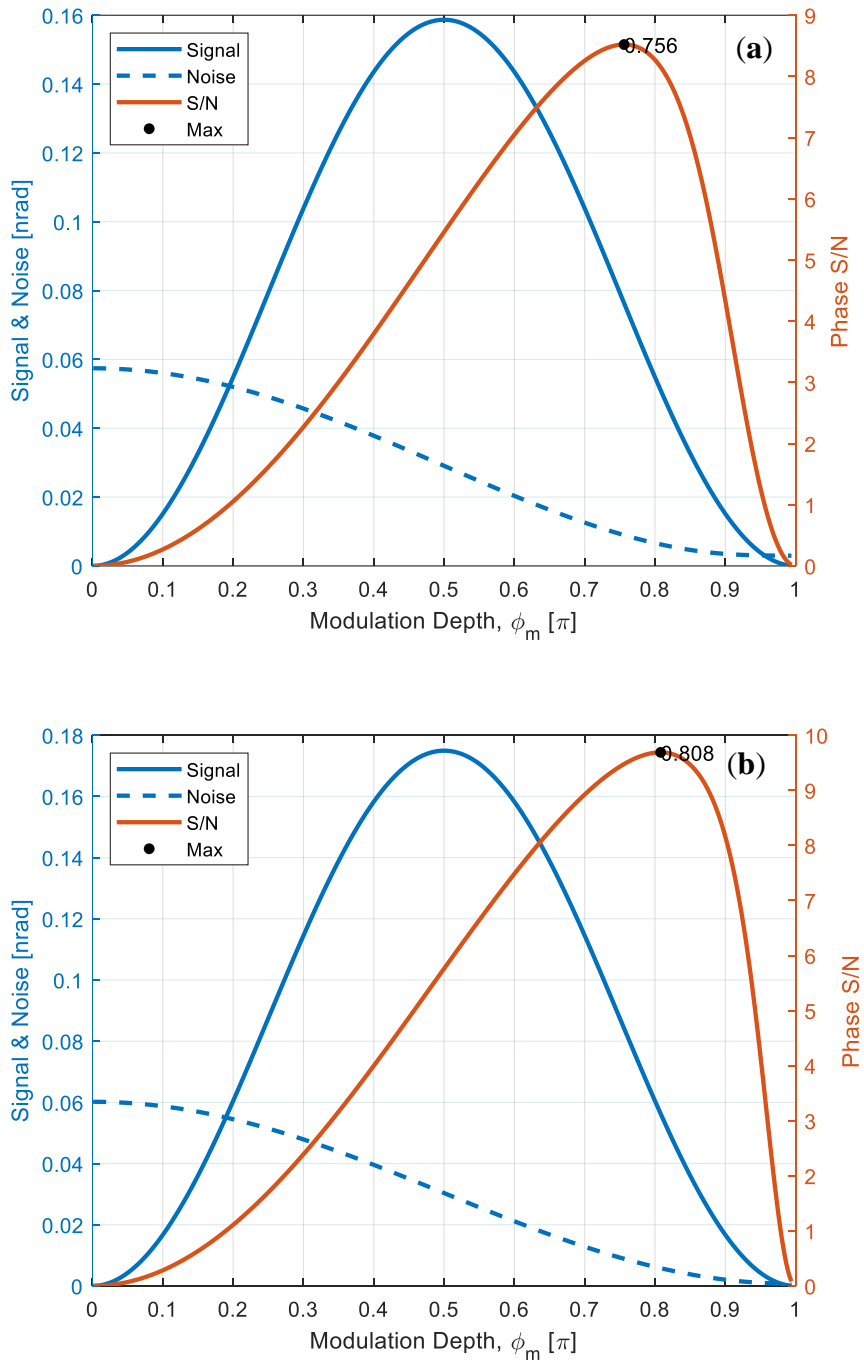


Figure 3.8. SNR analysis of 1030nm FOG (a) 100 $\mu$ W (b) 105 $\mu$ W optical power

The optimal SNR and modulation value shift with the %5 change in optical power. Correspondingly, the phase SNR value alters from 8.3 to 9.8 for a constant

modulation depth of  $0.8\pi$ . Therefore, optical power must be measured and optimized in order to improve the SNR value for a constant value of modulation depth.

In Section 2.7.1, ASE source configurations are studied in detail. Each design configuration has advantages and disadvantages regarding optical power, central wavelength stability and optical bandwidth. SPB configuration which results in the broadest bandwidth is realized to reduce ARW as the main purpose of this study. ASE configuration includes a pump LD operating at 976nm, a WDM that combines pump and emission wavelength, Yb-doped fiber with high concentration and an in-line fiber isolator to block back reflections resulting from fiber outputs. The system is shown in Figure 3.9.

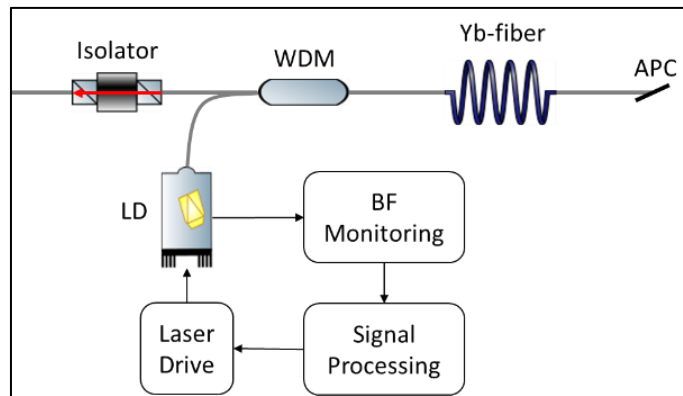


Figure 3.9. Single pass backward configuration

A control mechanism of optical power is needed to improve phase SNR as in Figure 3.8. The proposed methodology in this study contains a closed-loop control system that optimizes phase SNR with respect to output optical power at the ideal value as displayed in Figure 3.9. Back faced (BF) output of LD is used to monitor the power output of the system. The resulting value is controlled using a digital signal processing unit. Processing of signal decides consequent laser current. This closed-loop methodology enhances phase SNR by over 10% for a 5% variation of optical power.



## CHAPTER 4

### EXPERIMENTAL RESULTS

In this chapter, experimental results are presented including optical fiber, fiber coil, ASE components and ASE output. Finally, gyroscope output is characterized in terms of ARW performance.

#### 4.1 Fiber Coil Assembly Tests

In order to have a low-volume test setup and device, a compact fiber coil assembly is produced. Fiber optic coil assembly consists of fiber optic coil, MIOC and mechanical support.

A special polarization-maintaining fiber is selected which is optimized for a 1 $\mu$ m operating wavelength. Additionally, this fiber has a reduced coating of 165 $\mu$ m diameter compared to the standard 250 $\mu$ m diameter. A smaller form factor enables reduced component size. The fiber is Nufern/PM980-XP-80 panda-type fiber. Specifications of panda fiber are listed in Table 4.1.

Table 4.1. Nufern/PM980-XP-80 specifications

| Optical Specifications          | Specifications  | Actual |
|---------------------------------|-----------------|--------|
| Operating Wavelength [nm]       | 960 –1550       | -      |
| Core NA                         | 0.130           | -      |
| Mode Field Diameter [ $\mu$ m]  | 6.0 $\pm$ 0.5   | 6      |
| Cutoff [nm]                     | 910 $\pm$ 40 nm | 894    |
| Core Attenuation [dB/km@1060nm] | $\leq$ 2.0      | 1      |
| Beat Length [mm @ 980 nm]       | $\leq$ 2.6      | 1.9    |
| Clad Diameter [ $\mu$ m]        | 79-81           | 80     |
| Coating Diameter [ $\mu$ m]     | 155-175         | 163    |

PM panda fiber is wound using the quadrupole winding technique. The total length of the fiber is 150m. Final fiber coil parameters are listed in Table 4.2.

Table 4.2. Fiber coil specifications

| Length (m) | Mean Diameter (mm) | Height (mm) | # of Layers | # of Loop |
|------------|--------------------|-------------|-------------|-----------|
| 150        | 45                 | 12.0        | 14          | 73        |

Maintaining polarization in fiber is a crucial parameter. A polarization extinction ratio meter (PER) test setup as shown in Figure 4.1 is used to evaluate this parameter.

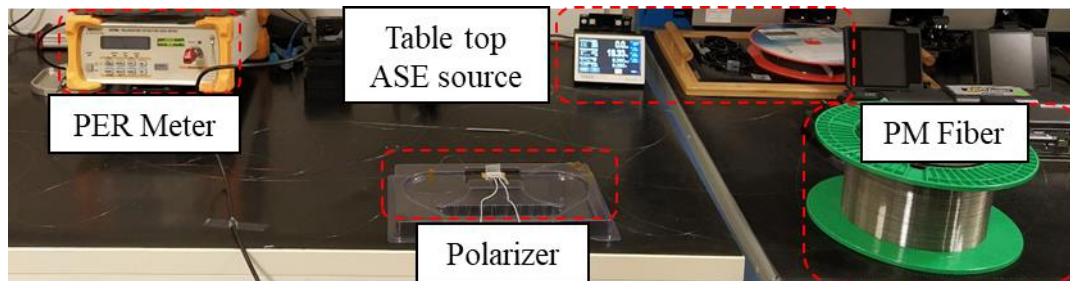


Figure 4.1. PER meter test setup

The output of the polarizer is used as a reference and the result is compared with PM fiber output as given in Table 4.3.

Table 4.3. PER meter results

| Polarizer Output [dB] | Fiber Coil Output [dB] |
|-----------------------|------------------------|
| 26.0                  | 24.5                   |

The fiber coil is wound using the quadrupole winding technique. The final fiber coil is displayed in Figure 4.2.



Figure 4.2. Fiber optic coil

MIOC is used for multiple purposes such as polarizing, coupling and modulating the phase of the input light. Characteristics of MIOC are given in Table 4.4.

Table 4.4. MIOC characteristics

|            | <b>Parameter</b>                   | <b>Unit</b> | <b>Test Data</b>        |
|------------|------------------------------------|-------------|-------------------------|
| Optical    | Operating Wavelength               | nm          | $1550 \pm 25$           |
|            | Insertion Loss                     | dB          | $\leq 3.5$              |
|            | Input Optical Power – max          | mW          | $\leq 200$              |
|            | Split Beam Ratio                   | -           | 47/53 ~ 53/47           |
|            | Pigtail Polarization Crosstalk     | dB          | $\leq -30$              |
|            | Polarization Extinction-chip       | dB          | $\geq 60$               |
|            | Additional Intensity<br>Modulating | %           | 0.2                     |
|            | Optical Return Loss                | dB          | $\geq 50$               |
| Electrical | Half Wave Voltage                  | V           | $\leq 4.5$              |
|            | Applied DC Voltage – max           | V           | $\leq 15$               |
|            | Electrode Type                     | -           | Push-pull<br>modulating |
|            | Bandwidth                          | MHz         | $\geq 300$              |

Table 4.4 (Continued)

|               |                       |    |            |
|---------------|-----------------------|----|------------|
| Mechanical    | Electrical Connector  | -  | 3 PIN      |
|               | Pigtail Type          | -  | PM         |
| Environmental | Operating Temperature | °C | -55 to +85 |

PERs of first and second output MIOC are 27.4dB and 26dB respectively. The coupling power of MIOC is given in Table 4.5.

Table 4.5. MIOC power coupling

| MIOC Input [mW] | 1 <sup>st</sup> Output [mW] | 2 <sup>nd</sup> Output [mW] |
|-----------------|-----------------------------|-----------------------------|
| 22.8            | 1.83                        | 1.47                        |
| 20.0            | 1.61                        | 1.30                        |
| 17.2            | 1.39                        | 1.13                        |
| 14.3            | 1.15                        | 0.95                        |
| 11.4            | 0.93                        | 0.76                        |
| 8.6             | 0.70                        | 0.58                        |
| 5.9             | 0.49                        | 0.40                        |
| 3.6             | 0.29                        | 0.24                        |
| 1.7             | 0.14                        | 0.11                        |
| 0.5             | 0.04                        | 0.03                        |
| 0.08            | 0.006                       | 0.006                       |

First, the fiber optic coil is fixed from the bottom side using special glue. MIOC is placed in the center of the assembly.

The picture of the fiber optic coil assembly is shown in Figure 4.3.

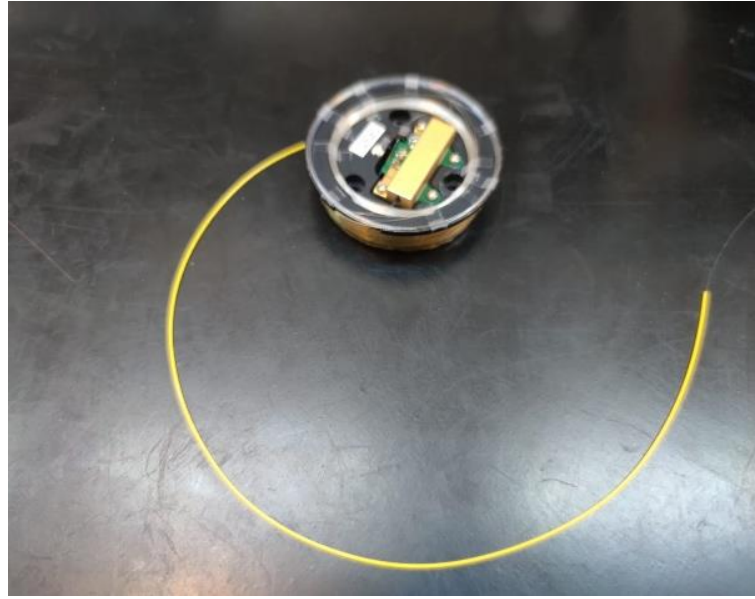


Figure 4.3. Fiber optic coil assembly

## 4.2 ASE Assembly Tests

The first step for ASE source manufacturing is characterizing the laser diode. Electro-optical characteristics of the laser diode are given in Table 4.6.

Table 4.6. Laser diode specifications

| Parameter  | Symbol            | Value | Unit               |
|--|-------------------|-------|--------------------|
| Case Temperature                                       | $T_c$             | 25    | $^{\circ}\text{C}$ |
| Operating Power  | $P_{op}$          | 450   | mW                 |
| Threshold Current                                      | $I_{th}$          | 65.40 | mA                 |
| Operating Current at $P_{op}$                          | $I_f P_{op}$      | 720   | mA                 |
| Operating Current at $P_{op} + 10\%$                   | $I_f \text{ ref}$ | 792   | mA                 |
| Forward Voltage at $P_{op} + 10\%$                     | $V_f$             | 1.62  | V                  |
| Monitor Photo Current at $P_{op}$                      | $I_{pd}$          | 657   | $\mu\text{A}$      |
| TEC Current at $P_{op} + 10\%$ at $75^{\circ}\text{C}$ | $\text{TEC}_i$    | 1.55  | A                  |
| TEC Voltage at $P_{op} + 10\%$ at $75^{\circ}\text{C}$ | $\text{TEC}_v$    | 1.80  | V                  |
| Peak Wavelength at $P_{op}$                            | $\lambda_p$       | 974.0 | nm                 |

The power and voltage versus current characteristics of the laser diode are given in Figure 4.4.

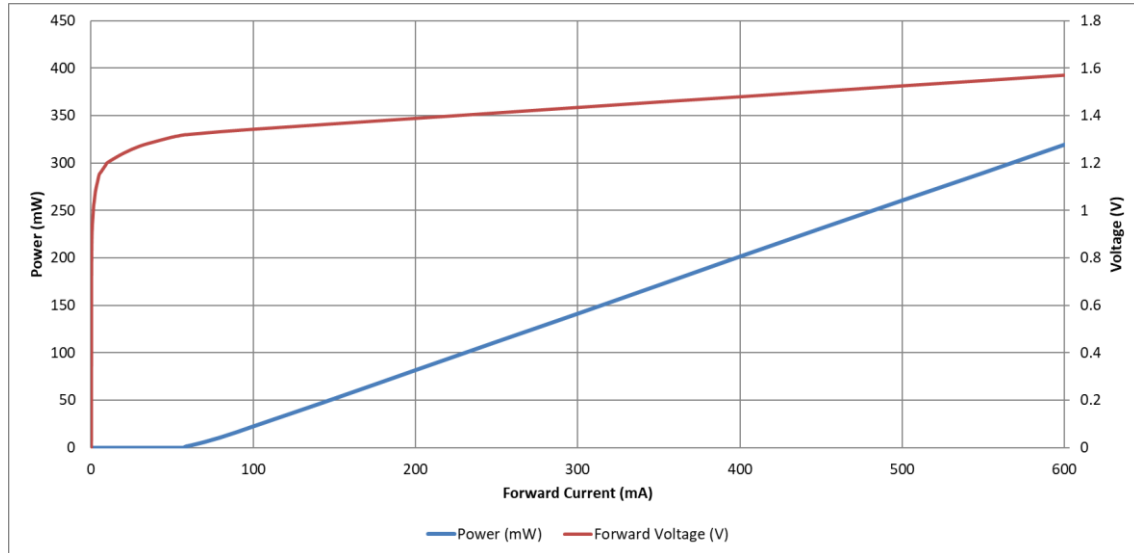


Figure 4.4. Laser diode characteristics

A pump protection filter (PPF) is used to protect the laser diode from back reflections due to fiber splices and other component connections. PPF characteristics are given in Table 4.7.

Table 4.7. PPF specifications

| Parameter                                     | Unit  | Value     |
|---|-------|-----------|
| Transmission Wavelength Range                 | nm    | 900 - 995 |
| Max. Insertion Loss                           | dB    | 0.7       |
| Min. Isolation @ Wavelength<br>1020 - 1120 nm | dB    | 30        |
| Max. Polarization Dependent Loss              | dB    | 0.1       |
| Min. Return Loss                              | dB    | 50        |
| Thermal Sensitivity                           | dB/°C | ≤ 0.005   |
| Thermal Wavelength Drift                      | nm/°C | ≤ 0.003   |
| Fiber Type                                    | -     | HI 1060   |
| Max. Optical Power (CW)                       | W     | 1         |

Table 4.7 (Continued)

|                             |    |            |
|-----------------------------|----|------------|
| Operating Temperature Range | °C | -5 to +70  |
| Storage Temperature Range   | °C | -40 to +85 |

WDM is used to collect backward emissions from Yb-doped fiber. WDM characteristics are given in Table 4.8.

Table 4.8. WDM specifications

| Parameter                    | Unit | Test Data         |
|------------------------------|------|-------------------|
| Fiber Type                   | -    | OFS980 Bare Fiber |
| Operating Wavelength         | nm   | 980/1030±5nm      |
| Insertion Loss @980/1030±5nm | dB   | 0.41/0.36         |
| Isolation @980/1030±5nm      | dB   | 14.95/13.49       |
| PDL @980                     | dB   | 0.05              |
| Directivity                  | dB   | 66                |
| Operating Temperature Range  | °C   | -40 to +85        |
| Storage Temperature Range    | °C   | -40 to +85        |

Yb-doped fiber is used as a gain medium. Fiber characteristics are given in Table 4.9.

Table 4.9. Yb-doped fiber specifications

| Optical                                     | Unit | Value     |
|---|------|-----------|
| Mode Field Diameter at 1060 nm              | µm   | 4.4 ± 0.8 |
| Peak Core Absorption at 976 nm<br>(nominal) | dB/m | (1200)    |
| Peak Core absorption at 920 nm              | dB/m | 280 ± 50  |
| Core Numerical Aperture<br>(nominal)        | -    | 0.2       |
| Cut-off Wavelength                          | nm   | 1010 ± 70 |

Table 4.9 (Continued)

| <b>Geometrical and Mechanical</b> |               |                                 |
|-----------------------------------|---------------|---------------------------------|
| Core Concentricity Error, $\leq$  | $\mu\text{m}$ | 0.7                             |
| Cladding Diameter (flat-to-flat)  | $\mu\text{m}$ | $125 \pm 2$                     |
| Cladding Geometry                 | -             | Round                           |
| Coating Diameter                  | $\mu\text{m}$ | $245 \pm 15$                    |
| Coating Material                  | -             | Dual coated high index acrylate |
| Proof Test, $\geq$                | kpsi          | 100                             |

A polarization-insensitive isolator is used to protect the ASE source from back reflections due to splice and component connection. Isolation is critical for obtaining stable power, central wavelength and output polarization state. Characteristics are given in Table 4.10.

Table 4.10. Isolator data

| <b>Parameter</b>                  | <b>Unit</b> | <b>Test Data</b>             |
|-----------------------------------|-------------|------------------------------|
| Center Wavelength ( $\lambda_c$ ) | nm          | 1030                         |
| Insertion Loss (0~50°C)           | dB          | 2.78                         |
| Isolation (23°C)                  | dB          | 27                           |
| PDL (23°C)                        | dB          | 0.02                         |
| Return Loss (Input)               | dB          | 52                           |
| Return Loss (Output)              | dB          | 56                           |
| Connector Type                    | -           | None                         |
| Fiber Type                        | -           | HI 1060                      |
| Fiber Jacket                      | -           | 250 $\mu\text{m}$ Bare Fiber |
| Max. Optical Power (CW)           | mW          | 80                           |
| Operating Temperature Range       | °C          | -40 to +85                   |

The tabletop ASE source is shown in Figure 4.5.

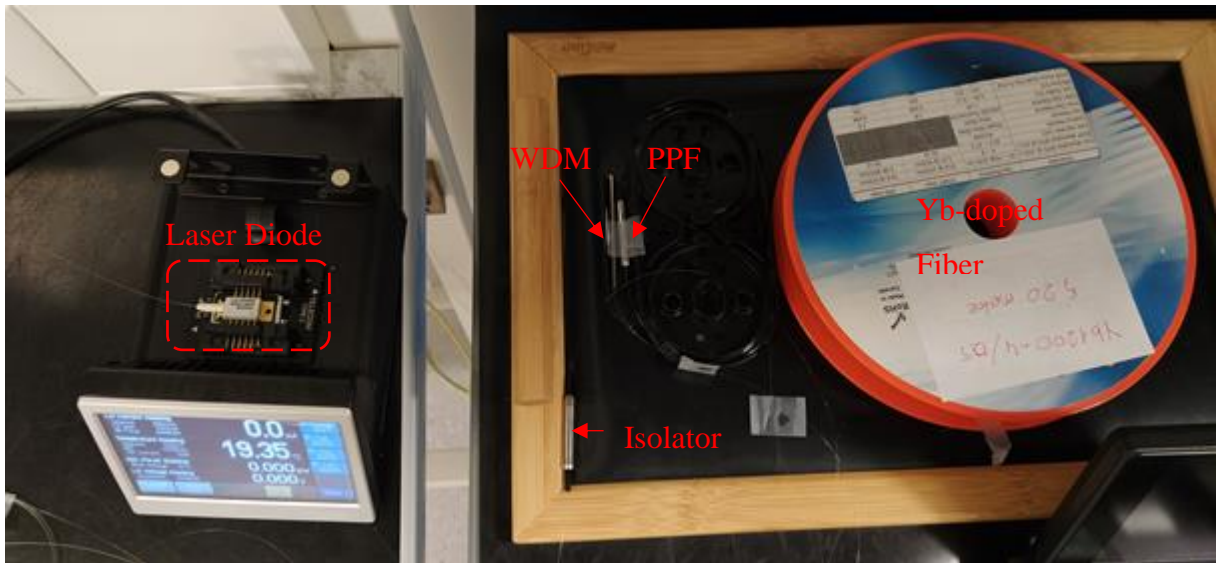


Figure 4.5. ASE source

Detailed ASE source test results are given in Section 2.7.2. After optimizing the ASE source, a compact, low-volume ASE source assembly is produced.

A mechanical tray is used to organize optical and optoelectronic components such as laser diode, PPF, WDM, Yb-doped fiber, optical isolator, and an optical coupler. A laser diode is driven by a laser diode driver while optical power and spectrum tests. ASE assembly is shown in Figure 4.6 and Figure 4.7.



Figure 4.6. ASE source assembly

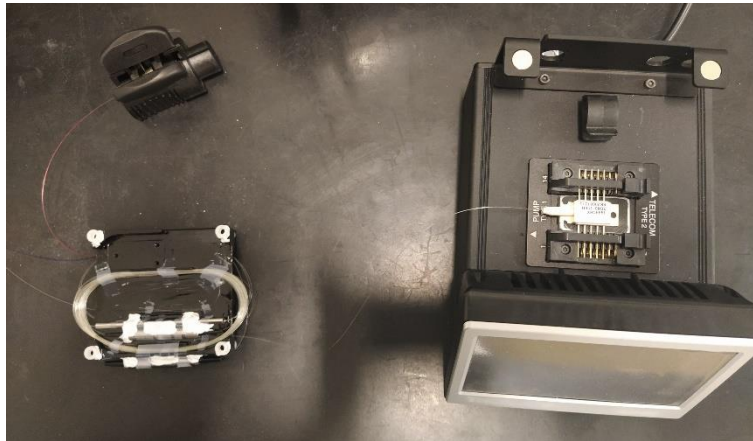


Figure 4.7. ASE source assembly and laser diode driver

Lastly, the output power and optical spectrum of the Yb-doped ASE source assembly are characterized. ASE source has a central wavelength of 1030.0nm with an optical bandwidth of 15nm. Spectrum is measured using an optical spectrum analyzer. The spectral output of ASE emission is displayed in Figure 4.8.

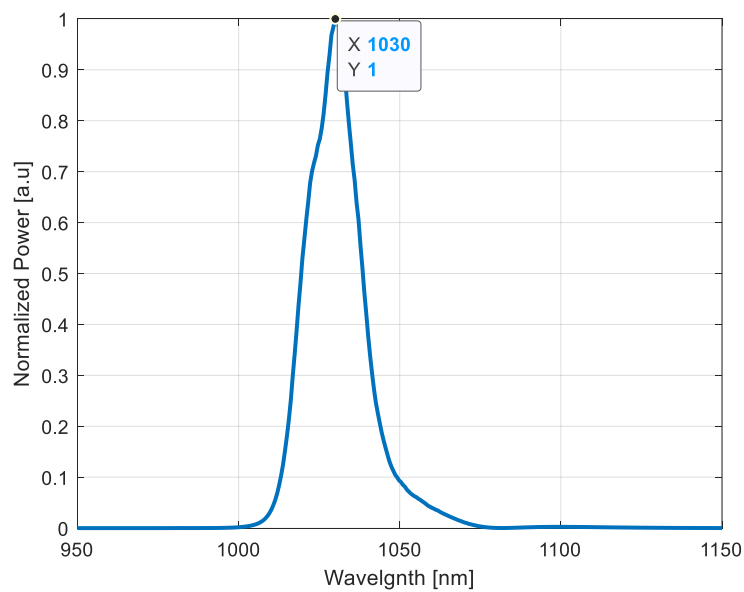


Figure 4.8. Yb-doped ASE source spectrum output

The output optical power of the Yb-doped ASE source was measured using a thermal power meter. The test results are shown in Figure 4.9.

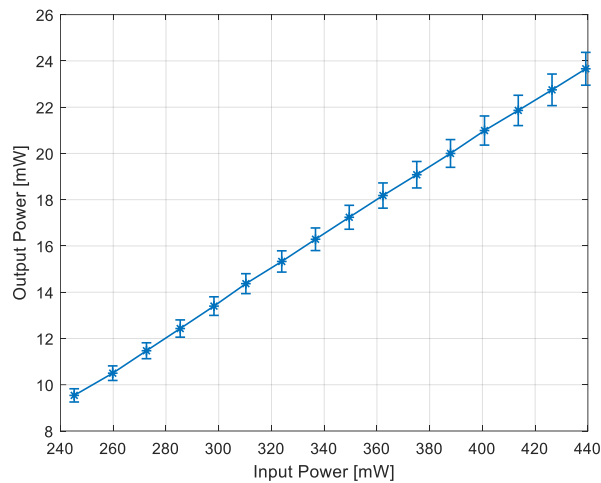


Figure 4.9. Optical power output of Yb-doped ASE source

A double laser diode current is needed in order to achieve comparable power levels with an Er-doped ASE source. 2.5W power is gained for around 0.5A laser diode current and 5V voltage.

### 4.3 IFOG Prototype and Tests

1030nm IFOG contains a light source as Yb-doped ASE, fiber coil as gyroscope sensor, detection and reading electronics. The output of the ASE source is coupled to MIOC and coil with PM fiber. Here, the sensing element is the PM fiber coil and MIOC is used to couple, polarize and modulate the light. Furthermore, a closed-loop feedback signal is directed to MIOC. PINFET converts the optical interference output of the sensing element of FOG into voltage. The voltage output of PINFET is converted to a digital signal via an ADC. Sensor control, data acquisition, signal processing, and input/output communication management are implemented in a main electronic card that consists of a processing unit (CPU). The digital signal processing (DSP) module calculates the mathematical operations of the closed-loop FOG. FOG is modulated in order to increase sensitivity and achieve a closed-loop operation. Biasing modulation shifts the interferometer to an operating point with higher sensitivity. Rate control loop feedback modulation is applied to null the phase

shift due to the Sagnac Effect at the interferometer. A diagram of IFOG is displayed in Figure 4.10.

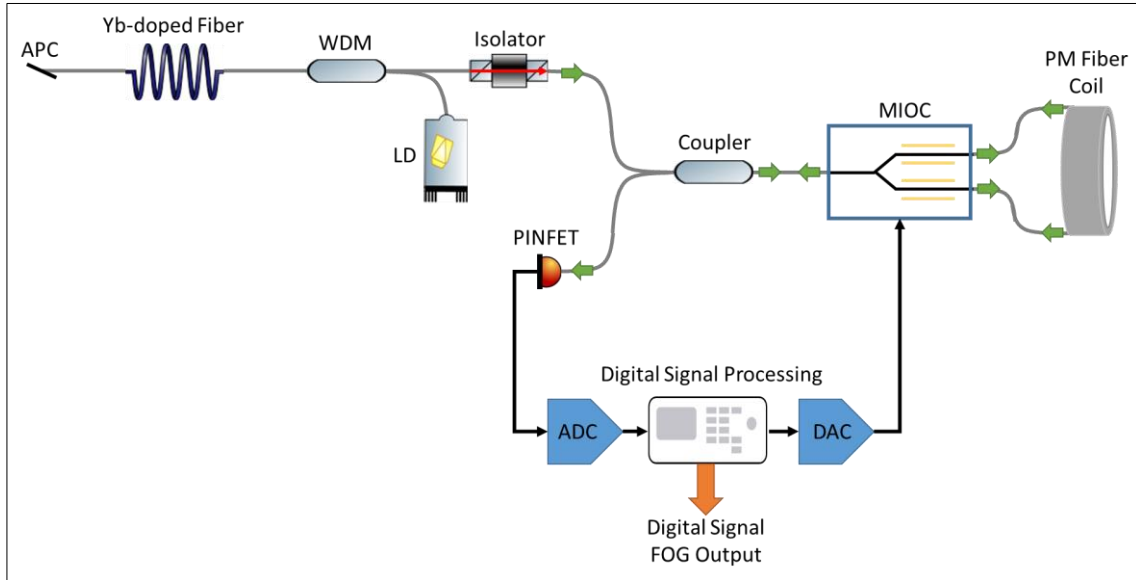


Figure 4.10. Functional scheme of Yb ASE IFOG

Characteristics of a 50/50 coupler are given in Table 4.11.

Table 4.11. 50/50 coupler specifications

| Parameter             | Unit | Test Data  |
|-----------------------|------|------------|
| Operating Wavelength  | nm   | 1030±10    |
| EL                    | dB   | 0.43       |
| TDL                   | dB   | 0.15       |
| RL/Dir                | dB   | 16         |
| Operating Temperature | °C   | 0 to +70   |
| Storage Temperature   | °C   | -40 to +85 |
| Proof test Level      | kpsi | 200        |

Characteristics of PINFET fiber are given in Table 4.12.

Table 4.12. PINFET specifications

| Parameter                                   | Unit  | Test Data      |
|---|-------|----------------|
| Minimum Bandwidth                           | MHz   | 250            |
| Suggested Data Rate                         | Mb/s  | 350            |
| Sensitivity                                 | dBm   | -32/34         |
| Dynamic Range                               | dB    | 25             |
| Transimpedance                              | kohms | 10             |
| Dark Current                                | nA    | 0.5            |
| Detector Responsivity<br>At 850/1300/1550nm | A/W   | 0.50/0.90/.095 |
| Max Output                                  | Vpp   | 2.5            |

An electronic board drives the laser diode and PINFET. Additionally, the PINFET output signal is collected via the same board. An electrical board is shown in Figure 4.11.

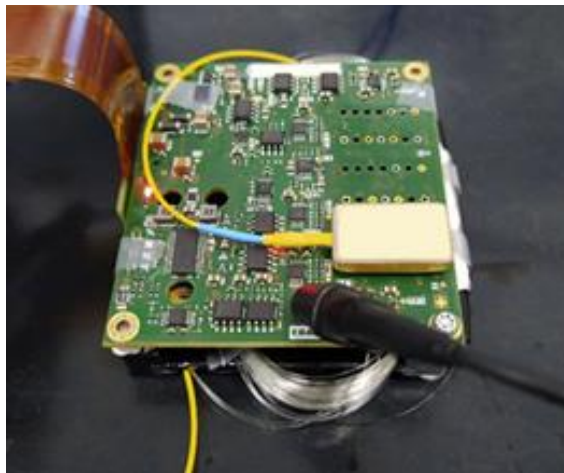


Figure 4.11. Driver electrical board

ASE source, fiber optic coil, MIOC and electronic cards; such as the main board, ASE board and power board were assembled using and mechanical frame. Electrical signals and currents are delivered using and internal cabling. The picture of the IFOG prototype is shown in Figure 4.12.

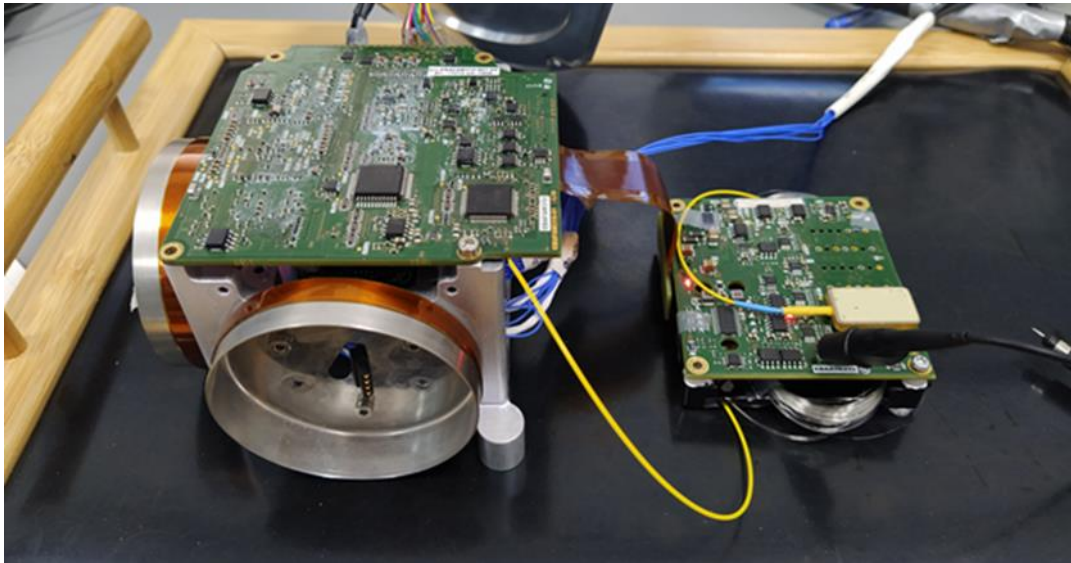


Figure 4.12. IFOG prototype

In order to prove proof of concept, an open-loop operation is demonstrated. Square wave voltage is applied to MIOC for phase modulation. PINFET signals are displayed in Figure 4.13 and Figure 4.14. The fiber coil is stable and rotated while a signal is recorded, respectively.

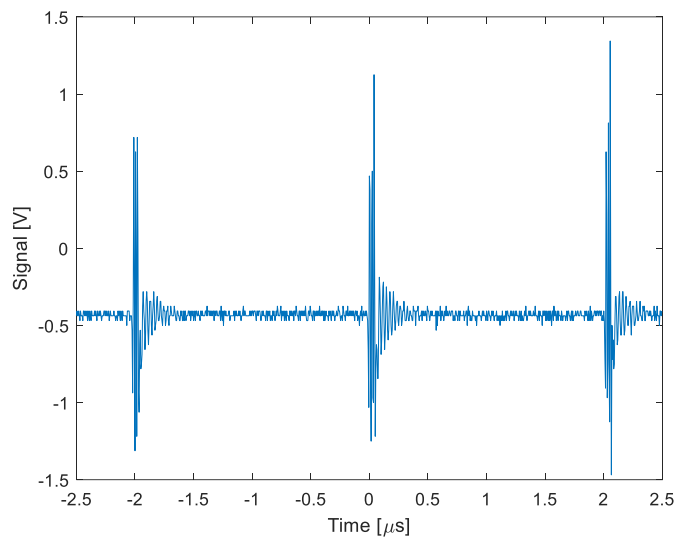


Figure 4.13. Signal output with no rotation

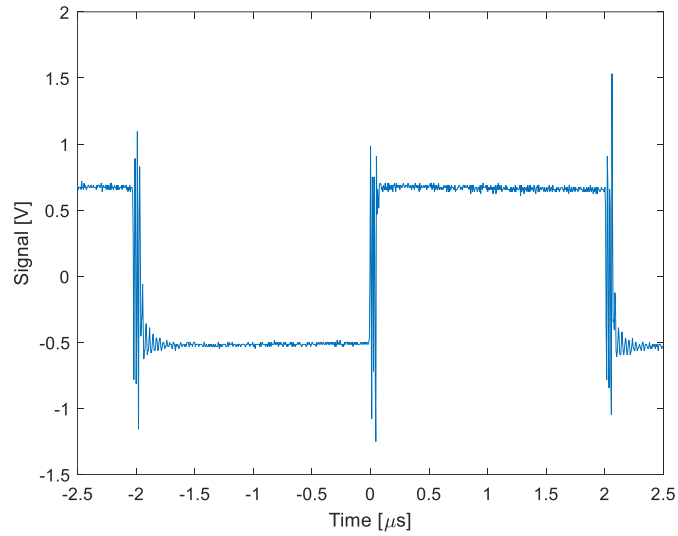


Figure 4.14. Signal output while rotating

ARW performance is analyzed using Allan Variance analysis for three optical power levels at PINFET. The ARW results are shown in Figure 4.15. Allan deviation curves for 10, 110 and 120  $\mu\text{W}$  (blue, red and green, respectively) are shown as straight lines which are the tangential lines with a slope of -0.5. The ARW parameter is determined by analyzing the intersection of  $\tau = 1\text{hr}$  value and extrapolated line in the Allan variance graphic.

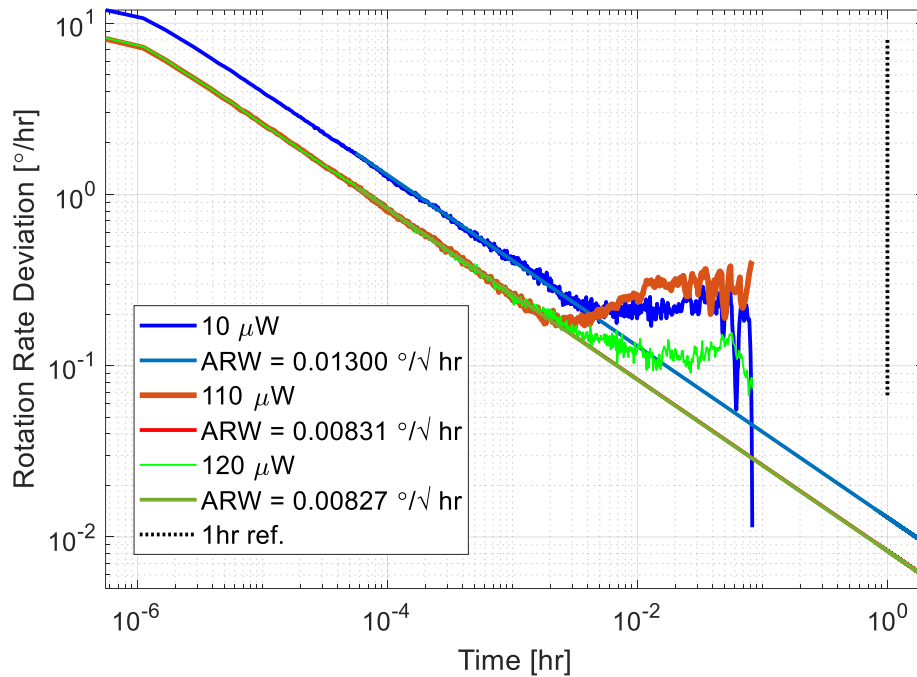


Figure 4.15. Allan variance analysis for 10, 110 and 120 $\mu$ W optical power

A good agreement was observed between the ARW performance results and the theoretical analysis of 1030nm IFOG. ARW values are  $0.0130^{\circ}/\sqrt{hr}$ ,  $0.00831^{\circ}/\sqrt{hr}$  and  $0.00827^{\circ}/\sqrt{hr}$  for 10  $\mu$ W, 110 $\mu$ W and 120 $\mu$ W respectively. Performance change indicates that the optical dependency of ARW is still observable. This dependency is more noticeable at 10 $\mu$ W optical power measurement. The IFOG system is optimized in order to achieve improved ARW performance. On the other hand, bias stability performance is not considered. The drift at the output signal in long term is due to the heat dissipation of electronics and mechanics. Bias stability performance can be enhanced by improving the mechanical design and having temperature calibration.

## CHAPTER 5

### CONCLUSION

In this study, various types of Yb-doped fiber ASE sources were examined and demonstrated. Particularly, four main configurations were studied by simulating their spectral outputs and comparing them with experimental results. Each configuration contains a WDM to isolate the pump laser diode from backward reflections, especially for forward configurations. Each configuration was tested for three different fiber lengths in order to determine the optimal fiber length.

ASE configurations were tested for various laser diode currents. In the meantime, the output spectrum and power were measured. Additionally, mean wavelength stability was characterized in the range of  $-40^{\circ}\text{C}$  to  $+60^{\circ}\text{C}$ . Central wavelength stability is one of the most critical parameters for fiber optic gyroscope applications. It determines the scale factor accuracy of the sensor.

The Central wavelength stability of the source depends on especially temperature characteristic of Yb-doped fiber. Additionally, pump laser characteristics such as pump wavelength, power and polarization have a crucial effect on emission wavelength. Fiber joints and fiber ends create back reflections that result in perturbation in Yb-fiber gain. Using an in-line isolator suppressed this effect.

Yb-doped fiber ASE sources have spectral bandwidth comparable to Er-doped fiber ASE. Higher efficiency levels of Yb-doped fiber enable higher output power levels with lower input pump laser currents. Moreover, the high radiation tolerance of Yb-doped fiber makes it more suitable for applications that involve low power consumption and radiation tolerance such as space applications.

Spectral simulations and spectrum measurements have a good agreement for SPF, SPB and DPF configuration regarding central wavelength. DPB configuration has a difference in mean wavelength between the simulation and test result. The spectral

response of the in-line reflector used in the DPB ASE source may cause this difference. Temperature dependency of both mean wavelength and optical power output simulations may be studied for a better understanding of the rewards of Yb-doped ASE sources.

Novel closed-loop control of the laser diode inside the ASE source was realized in the IFOG structure. This original method enhanced SNR by regulating the power output of the light source at optimum power. Phase SNR can be improved by more than %10 for a change of %5 optical power.

For the first time, an all-fiber closed-loop 1030nm fiber optic gyroscope was studied. Yb-doped ASE source having a broad bandwidth was implemented to reduce the main source of ARW. ARW was limited by the relative intensity noise of the ASE source. The central wavelength of the light source increased the scale factor of the gyroscope which results in higher sensitivity. All fiber assembly enables a compact and robust system. Yb-doped fiber has higher efficiency in the gain medium compared to Er-doped fiber. Lower operating currents are available which results from low power consumption. This is very critical, particularly for space applications. The rotation rate sensitivity of the sensor was increased by around 2-fold with the increase in scale factor compared to a common ASE source using 1550nm. Additional to the increase in sensitivity, ARW performance was similarly enhanced. Better gyroscope performance compared to a similar gyroscope operating at 1550nm was achieved.

In order to enhance ARW performance, different techniques such as laser broadening by phase modulation were developed in the literature. A 2-fold increase in ARW performance was confirmed. Combining the phase broadening method and Yb-doped ASE source would yield a 4-fold ARW performance enhancement. Additionally, the device volume can be decreased by designing a smaller gyroscope coil using a shorter fiber length for a target ARW performance. Radiation resistant characteristic of the Yb-doped ASE source makes the design suitable for space-grade missions in addition to low power requirement and low volume design.

## REFERENCES

- [1] M. N. Armenise, C. Ciminelli, F. Dell’Olio, and V. M. N. Passaro, *Advances in Gyroscope Technologies*, vol. 9783642154935. Springer-Verlag Berlin Heidelberg, 2010. doi: 10.1007/978-3-642-15494-2/COVER.
- [2] W. M. MacEk and D. T. M. Davis, “Rotation rate sensing with traveling-wave ring lasers,” *Appl Phys Lett*, vol. 2, no. 3, p. 68, Nov. 1963, doi: 10.1063/1.1753778.
- [3] E. A. Izmailov, M. M. Koleśnik, A. M. Osipov, and A. Akimov, “Hemispherical resonator gyro technology. Problems and possible ways of their solutions,” *undefined*, 1999.
- [4] A. Lawrence, *Modern Inertial Technology*. New York, NY: Springer New York, 1998. doi: 10.1007/978-1-4612-1734-3.
- [5] H. C. Lefèvre, *The Fiber-Optic Gyroscope, Second Edition*. 2014.
- [6] J. D. Jackson, *Classical Electrodynamics, 3rd edition*. John Wiley & Sons, New York, 1998.
- [7] B. E. A. Saleh and M. C. Teich, *Fundamentals of Photonics, Third edition*. John Wiley & Sons, 2019.
- [8] F. Aronowitz, “Fundamentals of the ring laser gyro,” *Optical gyros and their application*, vol. 339, 1999.
- [9] J. Noda, T. Hosaka, Y. Sasaki, and R. Ulrich, “Dispersion of Verdet constant in stress-birefringent silica fibre,” *Electron Lett*, vol. 20, no. 22, pp. 906–908, Oct. 1984, doi: 10.1049/EL:19840616.
- [10] E. Benser, G. Sanders, M. Smickilas, J. Wu, and L. Strandjord, “Development and evaluation of a navigation grade resonator fiber optic gyroscope,” *2015 DGON Inertial Sensors and Systems, ISS 2015 - Proceedings*, Oct. 2015, doi: 10.1109/INERTIALSENSORS.2015.7314259.

- [11] H. Ma, X. Yu, and Z. Jin, "Closed-loop resonant fiber optic gyro with an improved digital serrodyne modulation," *Opt Express*, vol. 21, no. 22, pp. 26578–26588, Nov. 2013, doi: 10.1364/OE.21.026578.
- [12] D. R. Ponikvar and S. Ezekiel, "Stabilized single-frequency stimulated Brillouin fiber ring laser," *Opt Lett*, vol. 6, no. 8, pp. 398–400, Aug. 1981, doi: 10.1364/OL.6.000398.
- [13] F. Zarinetchi, S. Ezekiel, and S. P. Smith, "Stimulated Brillouin fiber-optic laser gyroscope," *Opt Lett*, vol. 16, no. 4, pp. 229–231, Feb. 1991, doi: 10.1364/OL.16.000229.
- [14] S. Ezekiel, "Optical gyroscope options: Principles and challenges," *Optical Fiber Sensors (2006)*, paper MC1, p. MC1, Oct. 2006, doi: 10.1364/OFS.2006.MC1.
- [15] S. Merlo, M. Norgia, and S. Donati, *Fiber Gyroscope Principles*. Handbook of Fibre Optic Sensing Technology, John Wiley & Sons, Ltd., Hoboken, 2000.
- [16] H. J. Shaw, C. C. Cutler, and S. A. Newton, "Limitation of rotation sensing by scattering," *Optics Letters*, Vol. 5, Issue 11, pp. 488-490, vol. 5, no. 11, pp. 488–490, Nov. 1980, doi: 10.1364/OL.5.000488.
- [17] W. K. Burns and R. P. Moeller, "Polarizer requirements for fiber gyroscopes with high-birefringent fiber and broadband sources," *Optical Fiber Communication (1984)*, paper TuD5, p. TuD5, Jan. 1984, doi: 10.1364/OFC.1984.TUD5.
- [18] B. Culshaw, H. J. Shaw, C. C. Cutler, H. C. Lefevre, and R. A. Bergh, "Source statistics and the Kerr effect in fiber-optic gyroscopes," *Optics Letters*, Vol. 7, Issue 11, pp. 563-565, vol. 7, no. 11, pp. 563–565, Nov. 1982, doi: 10.1364/OL.7.000563.
- [19] P. F. Wysocki, M. J. F. Digonnet, B. Y. Kim, and H. J. Shaw, "Characteristics of Erbium-doped superfluorescent fiber sources for interferometric sensor

- applications,” *Journal of Lightwave Technology*, vol. 12, no. 3, pp. 550–567, 1994, doi: 10.1109/50.285318.
- [20] R. F. Schuma and K. M. Killian, “Superluminescent diode (SLD) wavelength control in high performance fiber optic gyroscopes,” *Proceedings Volume 0719, Fiber Optic Gyros: 10th Anniversary Conf.*, vol. 0719, pp. 192–196, Mar. 1987, doi: 10.1117/12.937557.
- [21] N. S. K. Kwong, K. Y. Lau, N. Bar-Chaim, I. Ury, and K. Lee, “High power GaAlAs superluminescent diode for fiber sensor applications,” *Optical Fiber Sensors (1988), paper FDD2*, p. FDD2, Jan. 1988, doi: 10.1364/OFS.1988.FDD2.
- [22] C. S. Wang, W. H. Cheng, C. J. Hwang, W. K. Burns, and R. P. Moeller, “High-power low-divergence superradiance diode,” *Appl Phys Lett*, vol. 41, no. 7, p. 587, Jun. 1998, doi: 10.1063/1.93618.
- [23] M. J. F. Digonnet, *Rare-Earth-Doped Fiber Lasers and Amplifiers, Revised and Expanded*. CRC Press, 2001. doi: 10.1201/9780203904657.
- [24] M. K. Jazi *et al.*, “The evaluation of various designs for a C and L band superfluorescent source based erbium doped fiber,” *Laser Phys*, vol. 23, no. 6, Jun. 2013, doi: 10.1088/1054-660X/23/6/065104.
- [25] H. Keskin, H. A. Vural, E. Alaçakir, and H. Altan, “The evaluation of various designs for ytterbium-doped fiber-based superfluorescent source at 1 $\mu$ m wavelength,” *Proc. SPIE 11772, Optical Sensors 2021*, vol. 11772, pp. 295–301, Apr. 2021, doi: 10.1117/12.2590737.
- [26] Y. Chen *et al.*, “A temperature-insensitive amplified spontaneous emission broadband source based on Er-doped fiber,” *Chinese Physics Letters*, vol. 35, no. 4, p. 044206, Apr. 2018, doi: 10.1088/0256-307X/35/4/044206.
- [27] F. Guattari, S. Chouvin, C. Molucon, and H. Lefevre, “A simple optical technique to compensate for excess RIN in a fiber-optic gyroscope,” *2014*

- DGON Inertial Sensors and Systems, ISS 2014 - Proceedings*, Feb. 2014, doi: 10.1109/INERTIALSENSORS.2014.7049411.
- [28] P. Ou, B. Cao, C. X. Zhang, Y. Li, and Y. H. Yang, “Er-doped superfluorescent fibre source with enhanced mean-wavelength stability using chirped fibre grating,” *Electron Lett*, vol. 44, no. 3, pp. 187–189, 2008, doi: 10.1049/EL:20082948.
- [29] S. Girard *et al.*, “Radiation effects on ytterbium- and ytterbium/erbium-doped double-clad optical fibers,” *IEEE Trans Nucl Sci*, vol. 56, no. 6, pp. 3293–3299, Dec. 2009, doi: 10.1109/TNS.2009.2033999.
- [30] S. Girard *et al.*, “Radiation effects on rare-earth doped optical fibers,” <https://doi.org/10.1117/12.862706>, vol. 7817, pp. 137–146, Sep. 2010, doi: 10.1117/12.862706.
- [31] A. Ladaci *et al.*, “X-rays,  $\gamma$ -rays, electrons and protons radiation-induced changes on the lifetimes of Er<sup>3+</sup> and Yb<sup>3+</sup> ions in silica-based optical fibers,” *J Lumin*, vol. 195, pp. 402–407, Mar. 2018, doi: 10.1016/J.JLUMIN.2017.11.061.
- [32] S. Girard *et al.*, “Recent advances in radiation-hardened fiber-based technologies for space applications,” *Journal of Optics (United Kingdom)*, vol. 20, no. 9, Aug. 2018, doi: 10.1088/2040-8986/AAD271.
- [33] R. P. Moeller and W. K. Burns, “1.06-um all-fiber gyroscope with noise subtraction,” 1902.
- [34] Z. Fang, K. Chin, R. Qu, and H. Cai, *Fundamentals of Optical Fiber Sensors*. Wiley, 2012.
- [35] E. Desurvire, *Erbium-doped Fiber Amplifiers: Principles and Applications*. Wiley-Interscience, 2002.

- [36] H. M. Pask *et al.*, “Ytterbium-doped silica fiber lasers: versatile sources for the 1–1.2  $\mu\text{m}$  region,” *IEEE Journal of Selected Topics in Quantum Electronics*, vol. 1, no. 1, pp. 2–13, 1995, doi: 10.1109/2944.468377.
- [37] A. Sharon and S. Lin, “Development of an automated fiber optic winding machine for gyroscope production,” *Robot Comput Integr Manuf*, vol. 17, no. 3, pp. 223–231, Jun. 2001, doi: 10.1016/S0736-5845(00)00030-2.
- [38] Coherent, “<https://www.coherent.com/resources/brochures/components-and-accessories/cohr-precision-wound-gyro-coils-brochure.pdf>,” May 19, 2022.
- [39] S. Du, Y. Guan, J. Jin, and C. Zhang, “Finite element model of thermal transient effect for crossover-free fiber optic gyros,” *Optik (Stuttg)*, vol. 123, no. 8, pp. 748–751, Apr. 2012, doi: 10.1016/J.IJLEO.2011.06.036.
- [40] W. Ling, X. Li, H. Yang, P. Liu, Z. Xu, and Y. Wei, “Reduction of the Shupe effect in interferometric fiber optic gyroscopes: The double cylinder-wound coil,” *Opt Commun*, vol. 370, pp. 62–67, Jul. 2016, doi: 10.1016/J.OPTCOM.2016.02.064.
- [41] E. M. Torney, “US5351900A - Method of manufacture of quadrupole-wound fiber optic sensing coil - Google Patents,” 1992 Accessed: May 24, 2022. [Online]. Available: <https://patents.google.com/patent/US5351900A/en>
- [42] M. Sardinha, J. Rivera, A. Kaliszek, and S. Kopacz, “EP2075535A2 - Octupole winding pattern for a fiber optic coil - Google Patents,” 2007 Accessed: May 24, 2022. [Online]. Available: <https://patents.google.com/patent/EP2075535A2/en>
- [43] “Fiber-optic Sensing: Transforming FOG coil manufacture from an art to a science | Laser Focus World.” <https://www.laserfocusworld.com/fiber-optics/article/16548093/fiberoptic-sensing-transforming-fog-coil-manufacture-from-an-art-to-a-science> (accessed May 19, 2022).

- [44] L. Jeunhomme, “Single-Mode Fiber Design for Long Haul Transmission,” *IEEE J Quantum Electron*, vol. 18, no. 4, pp. 727–732, 1982, doi: 10.1109/JQE.1982.1071563.
- [45] “Optical Fiber Couplers – Fosco Connect.” <https://www.fiberoptics4sale.com/blogs/archive-posts/95047750-optical-fiber-couplers> (accessed May 19, 2022).
- [46] “Optical Splitter 1 to 3 Steel Tube Single Mode Fused Type Fiber Splitter.” <https://fibrefibre.com/optical-splitter-3-in-1/> (accessed May 19, 2022).
- [47] “Economical 980 nm Filter WDM,980 nm Filter WDM Manufacturer.” [https://www.fiber-resources.com/980-nm-filter-wdm\\_p362.html](https://www.fiber-resources.com/980-nm-filter-wdm_p362.html) (accessed May 19, 2022).
- [48] C. Wang *et al.*, “Fiber Bragg gratings for microwave photonics subsystems,” *Opt Express*, vol. 21, no. 19, pp. 22868–22884, Sep. 2013, doi: 10.1364/OE.21.022868.
- [49] Raman. Kashyap, *Fiber Bragg gratings*. Academic Press, 2010.
- [50] “FBG Sensors & Systems AOS GmbH.” <https://www.aos-fiber.com/eng/Sensors/Sensoren.html> (accessed May 19, 2022).
- [51] F. Mitschke, *Fiber Optics: Physics and Technology: Second Edition*. Springer Berlin Heidelberg, 2016. doi: 10.1007/978-3-662-52764-1.
- [52] “The evolution of diodes - Diverse Electronics.” <https://www.diverseelectronics.com/blog/The-evolution-of-diodes-a20/> (accessed May 19, 2022).
- [53] “IR Laser Diode.” <https://www.rpmclasers.com/product/ldx-xxxx-960/> (accessed May 19, 2022).

- [54] “Types of LED, Application, Working, Symbol, Diagram & Construction.” <https://engineeringlearn.com/what-is-led-types-of-led-application-working-symbol-diagram-construction-complete-details/> (accessed May 19, 2022).
- [55] “SLD (Super-Luminescent Diode) Light Sources SLD series.” <https://www.anritsu.com/en-us/sensing-devices/products/sld> (accessed May 19, 2022).
- [56] “Pigtail LASER.” <https://onlinesale.cheaps2022.ru/category?name=pigtail%20laser> (accessed May 19, 2022).
- [57] A. Zhou *et al.*, “Simultaneous evaluation of two branches of a multifunctional integrated optic chip with an ultra-simple dual-channel configuration,” *Photonics Research*, Vol. 3, Issue 4, pp. 115-118, vol. 3, no. 4, pp. 115–118, Aug. 2015, doi: 10.1364/PRJ.3.000115.
- [58] B. G. Streetman and S. K. Banerjee, *Solid State Electronic Devices, Global edition*. Pearson Education, 2016.
- [59] S. B. Alexander, “Optical communication receiver design,” p. 314, 1997.
- [60] “PINFET Optical Receiver Modules.” [https://www.laserdiode.com/standard\\_products/products/pinfet-optical-receiver-modules](https://www.laserdiode.com/standard_products/products/pinfet-optical-receiver-modules) (accessed May 29, 2022).
- [61] R. Paschotta, J. Nilsson, A. C. Tropper, and D. C. Hanna, “Ytterbium-doped fiber amplifiers,” *IEEE J Quantum Electron*, vol. 33, no. 7, pp. 1049–1056, Jul. 1997, doi: 10.1109/3.594865.
- [62] D. C. Hanna *et al.*, “Continuous-wave oscillation of a monomode Ytterbium-doped fibre laser,” *Electron Lett*, vol. 24, no. 17, pp. 1111–1113, 1988, doi: 10.1049/EL:19880755.

- [63] R. Paschotta, J. Nilsson, P. R. Barber, J. E. Caplen, A. C. Tropper, and D. C. Hanna, "Lifetime quenching in Yb-doped fibres," *Opt Commun*, vol. 136, no. 5–6, pp. 375–378, Apr. 1997, doi: 10.1016/S0030-4018(96)00720-1.
- [64] L. D. DeLoach, S. A. Payne, L. L. Chase, L. K. Smith, W. L. Kway, and W. F. Krupke, "Evaluation of absorption and emission properties of Yb<sup>3+</sup> doped crystals for laser applications," *IEEE J Quantum Electron*, vol. 29, no. 4, pp. 1179–1191, 1993, doi: 10.1109/3.214504.
- [65] G. Barnard, P. Myslinski, J. Chrostowski, and M. Kavehrad, "Analytical Model for Rare-Earth-Doped Fiber Amplifiers and Lasers," *IEEE J Quantum Electron*, vol. 30, no. 8, pp. 1817–1830, 1994, doi: 10.1109/3.301646.
- [66] C. H. Henry, "Theory of Spontaneous Emission Noise in Open Resonators and its Application to Lasers and Optical Amplifiers," *Journal of Lightwave Technology*, vol. 4, no. 3, pp. 288–297, 1986, doi: 10.1109/JLT.1986.1074715.
- [67] D. C. Hall, D. C. Hall, W. K. Burns, and R. P. Moeller, "High-stability Er<sup>3+</sup>-doped superfluorescent fiber sources," *Journal of Lightwave Technology*, vol. 13, no. 7, pp. 1452–1460, 1995, doi: 10.1109/50.400711.
- [68] D. W. Allan, "Statistics of atomic frequency standards," *Proceedings of the IEEE*, vol. 54, no. 2, pp. 221–230, 1966, doi: 10.1109/PROC.1966.4634.
- [69] Institute of Electrical and Electronics Engineers, *IEEE Standard Specification Format Guide and Test Procedure for Single-Axis Interferometric Fiber Optic Gyros*, vol. 1997. 2008.
- [70] NATO-RTO, "Optical gyros and their application," *Rto-Ag-339 Ac/323(Sci)Tp/9*, vol. 323, no. May, p. 336, 1999.
- [71] S. Ögüt, "Implementation of digital detection scheme for fiber optic gyroscope," M.Sc. thesis, Bilkent University, Ankara, 2013.

- [72] R. A. Bergh, H. C. Lefevre, and H. J. Shaw, "An overview of fiber-optic gyroscopes," *Journal of Lightwave Technology*, vol. 2, no. 2, pp. 91–107, 1984, doi: 10.1109/JLT.1984.1073580.
- [73] K. Iwatsuki, "Excess noise reduction in fiber gyroscope using broader spectrum linewidth Er-doped superfluorescent fiber laser," *IEEE Photonics Technology Letters*, vol. 3, no. 3, pp. 281–283, 1991, doi: 10.1109/68.79781.
- [74] R. P. Scott, C. Langrock, and B. H. Kolner, "High-dynamic-range laser amplitude and phase noise measurement techniques," *IEEE Journal on Selected Topics in Quantum Electronics*, vol. 7, no. 4, pp. 641–655, Jul. 2001, doi: 10.1109/2944.974236.
- [75] H. Keskin, H. A. Vural, B. Altınöz, Ü. Bektik, and H. Altan, "1030 nm all-fiber closed-loop fiber optic gyroscope with high sensitivity," *J Sens*, vol. 2022, pp. 1–8, Oct. 2022, doi: 10.1155/2022/8967827.



## CURRICULUM VITAE

Surname, Name: Keskin, Hakan

### EDUCATION

| Degree      | Institution  | Year of Graduation |
|-------------|--|--------------------|
| MS          | METU Physics Dept.                                 | 2013               |
| BS          | METU Physics Dept.                                 | 2011               |
| High School | Türk Eğitim Vakfı İnanç Türkeş Özel Lisesi, Ankara | 2006               |

### FOREIGN LANGUAGES

Advanced English, Beginner German

### PUBLICATIONS

1. Keskin, H., Vural, H. A., Altınöz., B., Bektik, Ü., Altan., H. 1030nm All Fiber Closed-Loop Fiber Optic Gyroscope with High Sensitivity. *J Sensors* 2022, 8967827, 8 (2022)
2. Gaafar, M., Richter, P., Keskin, H., Möller, C., Wichmann, M., Stolz, W., Rahimi-Iman, A., Koch, M. Self-mode-locking semiconductor disk laser. *Opt. Express* 22, 28390-28399 (2014)
3. Takan, T., Keskin, H. and Altan, H. Low-cost bandpass filter for terahertz applications. *Opt Quant Electron* 47, 953–960 (2015)
4. Keskin, H., Altan, H., Yavas, S., Ilday, F.O., Eken, K., Sahin, A.B. Development of a rapid-scan fiber-integrated terahertz spectrometer. *Opt. Quantum Electron.* 46(4), 495-503 (2014)

Piano, Baglama, Anime, Computer Games, Learning, Improvement, Efficiency and Problem Solving